Low-Linewidth Optical Comb Sources based on Gain-Switched Lasers

Justin K. Alexander
BSc

Thesis submitted for the degree of Doctor of Philosophy

NATIONAL UNIVERSITY OF IRELAND, CORK

SCHOOL OF SCIENCE
DEPARTMENT OF PHYSICS

September 2017

Head of Department: Prof John McInerny

Supervisors: Prof Frank H. Peters
Mr. Brian Corbett

Research supported by Science Foundation Ireland

Contents

List of Figures

List of Tables

List of Acronyms

AO-OFDM: All-Optical Orthogonal Frequency Division Multiplexing
DFB: Distributed Feedback Laser
DP-QPSK: Dual Polarization Quadrature Phase Shift Keying
DUT: Device Under Test
DWDM: Dense-Wavelength Division Multiplexing
EAM: Electro-absorption Modulator
EDFA: Erbium-Doped Fibre Amplifier
EF: Etched Facet
ESA: Electrical Spectrum Analyser
FP: Fabry-Pérot
FSR: Free Spectral Range
IPG: Integrated Photonics Group
ITU: International Telecommunication Union
MEF: Metal Etched Facet MMI: Multimode Interference Coupler
MZM: Mach-Zehnder Modulator
OOK: On-Off Keying
OSA: Optical Spectrum Analyser
PIC: Photonic Integrated Circuit
QAM: Quadrature Amplitude Modulation
QPSK: Quadrature Phase-Shift Keying
QW: Quantum Well
SFP: Slotted Fabry-Pérot
SMSR: Side-Mode Suppression Ratio
SOA: Semiconductor Optical Amplifier
TEC: Thermoelectric Cooler
TLS: Tunable Laser Source
WDM: Wavelength Division Multiplexing

I, Justin K. Alexander, certify that this thesis is my own work and has not been submitted for another degree at University College Cork or elsewhere.

Justin K. Alexander

"A man does not fly like a bird, but one foot moves and then another and one day a man is there" - No one

Acknowledgements

Firstly, I would like to thank my supervisor Prof. Frank Peters for welcoming me to the Integrated Photonics Group (IPG) at Tyndall, and for his constant guidance over the long years of this PhD. I would like to show my gratitude to his wife Jo Peters for hosting the group on numerous occasions for delicious lunches and entertaining afternoons of boardgames.

A big thank you to Padraic Morrissey for his support throughout my PhD, whether it be on experimentation, writing, or videogame recommendations. With his help, I hit the ground running with the main body of this work. I thank the senior past and present members of IPG for helping me find my feet in the early days of my PhD, Eddie Cotter, Rob Sheehan, Hua Yang, Mark Crowley, and thanks to Philip Marraccini for saving the last dance. Thank you to my co-supervisor, Brian Corbett, and to James O'Callaghan, Brendan Roycroft, and the other members of the Photonics Devices group, for their helpful discussions throughout the years. Thank you to my PhD monitor, Peter O'Brien, for taking the time to give feedback during my annual reviews.

Cheers to Fabien Dubois and Joe Cashell for making the Kane building less grim back when we started our post-grads. Big shout-out to Shane Duggan, Alison "Bloodhound" Perrott, Niamh Kavanagh, and Brian Murray for the lunchtime bants, to Moises Jezzini and Prasanna Ramaswamy for the post PIC meeting teas and good humour, and to Mohamad Dernaika and Ludovic Caro for being fab friends. Thank you to Maryam Shayesteh for her superb SEMs, and to all the other members of IPG, Kevin Shortiss, Masoud Seifikar, Niall Kelly, Francesco Azzerallo, and Mingqi Yang.

To my good pals, Feargus, Áine, Ben, Neeve, Mike, and John, I say thank you. To my girlfriend Emily, thank you for your love and support over the past few years.

I am grateful for the unfailing support provided from my family, my parents Maria and Ken, my brothers Melvin and Stephen, and a special thanks to my sister Donna for her help with the make writing good.

Abstract

As the number of internet users continues to grow, along with the increase in bandwidth demanding services, the optical communications network struggles to keep up. Upgrading the optical fibre network is a costly endeavour, therefore research into spectrally efficient communication methods must be performed to combat the year-on-year increase in bandwidth demand. Long-haul communications has typically relied on wavelength division multiplexing (WDM) to transmit multiple optical carriers through a single fibre. Each wavelength carrier must be separated by a guard band to reduce interference between channels. By moving to a coherent set of carriers, these guard bands can be reclaimed as usable bandwidth.

Optical superchannels, which consist of several sub-carriers, can be used to increase the information spectral density (Gbps/Hz). An even greater increase in the information spectral density can be achieved by implementing all-optical orthogonal frequency division multiplexing (AO-OFDM). Coherent communications systems, such as AO-OFDM, require a coherent optical comb source as a fundamental component.

The work presented in this thesis investigates several device designs for the generation of optical combs based on gain-switched slotted Fabry-Pérot lasers. The semiconductor rate equations were used to analyse the phase noise properties of a gain-switched single mode laser both with and without optical injection-locking. Phase noise was shown to increase with gain-switching, and decrease when the gain-switched laser was injection-locked to a low linewidth master laser. Photonic integration was used to integrate two lasers on a single chip for the purpose of generating a low linewidth optical comb. Optical combs with linewidths in the region of $300\,\mathrm{kHz}$ were generated, with a comb line spacing of up to $10\,\mathrm{GHz}$ demonstrated.

The versatile design of these comb sources show promise for further integration with splitters and modulators to facilitate the development of an AO-OFDM transmitter photonic integrated circuit (PIC). Such a PIC is essential in meeting the future bandwidth demands of the optical communications network.

List of Publications

[1] J. K. Alexander, W. Cotter, J. Cashell, P.E. Morrissey, B. Corbett and F.H. Peters, "Current controller development for testing next generation photonic integrated circuits," Institute of Physics (IOP) Spring Meeting, Cork, Ireland, March 2015.

[2] J. K. Alexander, P.E. Morrissey, M. Yang, H. Yang, B. Corbett, and F.H. Peters, "Resonance Enhancement of Monolithically Integrated Common Cavity Device," Photonics Ireland, Cork, Sept. 2015.

[3] F. M. Dubois, E. Sooudi, R. N. Sheehan, E. Clerkin, M. Yang, J. K. Alexander, H. Yang, and F. H. Peters, "Mutually Coupled Semiconductor Lasers in Photonic Integrated Circuits", Photonics Ireland, Cork, Sept. 2015.

[4] J. K. Alexander, P. E. Morrissey, H. Yang, M. Yang, P. J. Marraccini, B. Corbett, and F. H. Peters, "Monolithically integrated low linewidth comb source using gain switched slotted Fabry-Perot lasers," Opt. Express, vol. 24, no. 8, p. 7960, 2016.

[5] J. K. Alexander, P.E. Morrissey, H. Yang, M. Yang, and F.H. Peters, "Monolithically Integrated Optical Comb Generation Device," Institute of Physics (IOP) Spring Meeting, Belfast, Northern Ireland, Feb. 2016.

[6] J. K. Alexander, P. E. Morrissey, H. Yang, M. Yang, and F. H. Peters, "Resonance Enhancement of a Monolithically Integrated Common Cavity Device," in European Conference on Integrated Optics (ECIO), 2016.

[7] F. Dubois, E. Sooudi, P. E. Morrissey, J. Alexander, H. Yang, and F. H. Peters, "Mutually Coupled Semiconductor Lasers in Photonic Integrated Circuits," in European Conference on Integrated Optics (ECIO), 2016, pp. 18–19.

[8] N. P. Kelly, M. Dernaika, L. Caro, P. E. Morrissey, A. H. Perrott, J. K. Alexander, and F. H. Peters, "Regrowth-Free Single Mode Laser Based on Dual Port Multimode Interference Reflector," IEEE Photonics Technol. Lett., vol. 29, no. 3, pp. 279–282, Feb. 2017.

[9] J. K. Alexander, P.E. Morrissey, H. Yang, M. Yang, and F.H. Peters, "A Photonic Device for Superchannel Communication Systems," Institute of Physics (IOP) Spring Meeting, Dublin, Ireland, March 2017.

[10] M. Dernaika, L. Caro, N. P. Kelly, J. K. Alexander, F. Dubois, P. E. Morrissey, and F. H. Peters, "Deeply Etched Inner-Cavity Pit Reflector," IEEE Photonics J., vol. 9, no. 1, pp. 1–8, 2017.

[11] L. Caro, N. P. Kelly, M. Dernaika, M. Shayesteh, P. E. Morrissey, J. K. Alexander, and F. H. Peters, "A facetless regrowth-free single mode laser based on MMI couplers," Opt. Laser Technol., vol. 94, pp. 159–164, 2017.

[12] J. Alexander, P. Morrissey, L. Caro, M. Dernaika, N. Kelly, and F. Peters, "On-chip investigation of phase noise in monolithically integrated gain-switched lasers," IEEE Photonics Technol. Lett., vol. 29, no. 9, pp. 1–1, 2017.

[13] J. K. Alexander, P. E. Morrissey, H. Yang, M. Yang, Y. Zhao, M. Rensing, P. O'Brien, and F. H. Peters, "Butterfly packaged low-linewidth optical comb source," Electron. Lett., vol. 53, no. 9, pp. 615–616, 2017.

[14] S. P. Duggan, N. P. Kelly, L. Caro, M. Dernaika, M. Shayesteh, J. K. Alexander, H. Yang, P. E. Morrissey, A. Gocalinska, K. K. Thomas, E. Pelucchi, and F. H. Peters, "Development of inverted p-substrate InP/AlGaInAs lasers for vertical integration with multiple passive or active intrinsic regions," in European Conference on Integrated Optics (ECIO), 2017.

[15] J. K. Alexander, P. E. Morrissey, L. Caro, M. Dernaika, N. P. Kelly, and F. H. Peters, "Integratable Optical Comb Source for Coherent Communications Systems," in Conference on Lasers and Electro-Optics (CLEO) USA, May 2017.

[16] H. Yang, M. Yang, Y. Zhao, L. Zhang, Z. Jia, J. Alexander, L. Zhao, D. C. Hall, F. H. Peters, "Butterfly Packaged Ultra-narrow Linewidth Single Frequency Teardrop Laser Diode," IEEE Photonics Technol. Lett., no.99, 2017.

[17] J. K. Alexander, P.E. Morrissey, M. Dernaika, L. Caro, N. P. Kelly, and F. H. Peters, "A Facetless Gain-Switched Laser for Optical Comb Generation," Photonics Ireland, Galway, Sept. 2017.

Chapter 1

Introduction

1.1 Fibre Optic Communications

From the demonstration of the first solid state ruby laser in 1960 [1], to the first optical fibre field experiments performed in Italy in the 1970's [2], the growth of fibre optic communications has been a major driving force for research and development of communication technologies. Today, over 300 million kilometers of optical fibre have been deployed worldwide [3]. Fibre optic networks have enabled the rapid growth of communication systems and has revolutionised media distribution. The number of Internet users surpassed 3 billion in 2015, with over 40% of the world's population using the Internet as of 2016, a dramatic increase from just 1% of the population in 1993 [4]. Figure 1.1 shows the growth of Internet users from 2001 to 2015 per region.

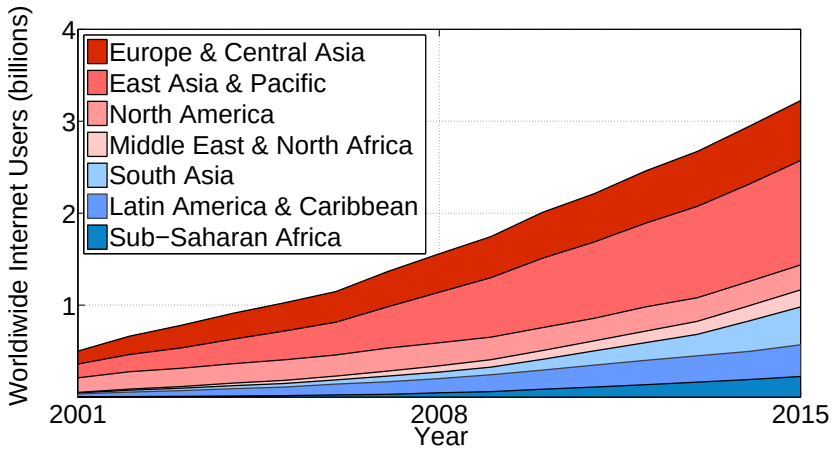

Figure 1.1: Total worldwide Internet user growth from 2001 to 2015. User growth by region is shown within each color [5].

Among this user base there is a growing demand for bandwidth intensive services such as high-definition video streaming (Netflix, YouTube), video chat (Skype, Facetime), cloud storage (Dropbox, Google Drive), as well as the all pervasive social media applications (Facebook, Snapchat). Figure 1.2 shows the average worldwide bandwidth use per month each year, with forecast figures for 2017 - 2019 [6].

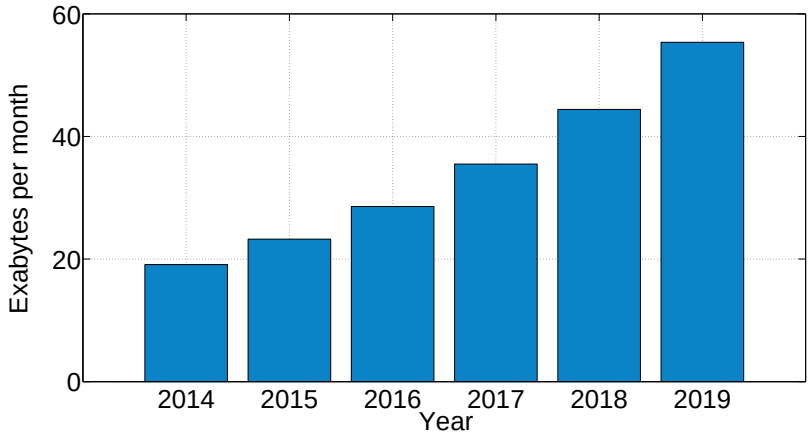

Figure 1.2: Average worldwide bandwidth use per month each year from 2014 - 2016, with estimates for years 2017 - 2019 [6].

With no end in sight to the rising demand for bandwidth, and the growing number of users, there is a strong drive for the research and development of optical transmitters capable of sending data at higher and higher rates. Developing methods which take advantage of the existing infrastructure is key to meeting demand, since the economic effort required to lay new fibre cables is excessive [7].

10 Gbit/s transmitters, demonstrated in research labs as early as 1994 [8], and standardised in 2002, typically use on-off keying (OOK) to transmit data. The OOK modulation format uses direct modulation of a laser, and is simple to implement, capable of sending 1 bit of data per optical symbol, where the laser signal on is a 1 and the laser signal off is a 0. The number of bits per optical symbol can be increased with the use of advanced modulation formats [9]. Quadrature phase shift keying (QPSK), also known as 4-QAM (quadrature amplitude modulation) is one such modulation format, capable of encoding 2 bits per optical symbol. QPSK achieves this by using four different phases. Constellation diagrams can be seen in Figure 1.3 illustrating the operation of OOK and QPSK.

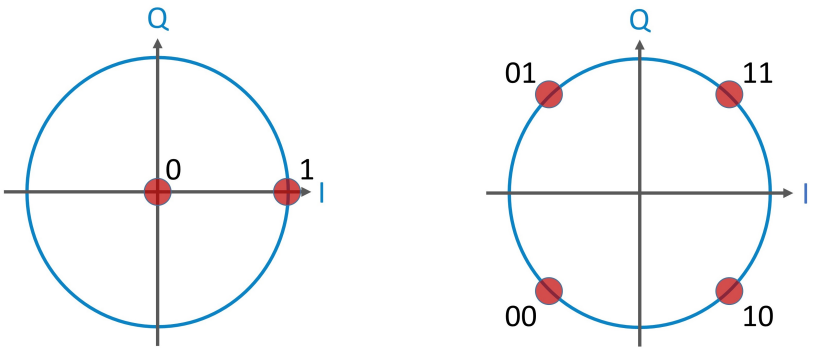

(a) (b)

Figure 1.3: (a) Constellation diagram illustrating on-off keying (OOK). (b) Quadrature phase shift keying (QPSK).

A more sophisticated variation of QPSK called polarization maintained QPSK, or PM-QPSK (also known as dual polarization QPSK), can be used to double the spectral efficiency by allowing two optical signals with orthogonal polarisations to coexist in the same fibre and frequency space, with the orthogonality maintained over transmission. DP-QPSK was standardised in 2010 [9] for 40 Gbit/s and 100 Gbit/s transmitters, having first been demonstrated in 2005 [10, 11]. The decrease in time between lab demonstration and industry standardization when compared to 10 Gbit/s transmission is notably in keeping with the rising demand.

The use of advanced modulation formats places stringent requirements on the phase noise properties of the transmitting laser. Assuming a symbol rate of $10\,\mathrm{GBaud}$, a laser linewidth of $4.1\,\mathrm{MHz}$ is required for 4-QAM to maintain a manageable bit error rate (BER) [12]. To move to higher order modulation formats such as 16-QAM and 64-QAM, laser linewidths as low as $1.4\,\mathrm{MHz}$ and $400\,\mathrm{kHz}$ are required respectively.

From reference [13], PM-QPSK has a reach of $3000\,\mathrm{km}$, while PM-64-QAM has a reach of $175\,\mathrm{km}$. This reduction in reach presents another disadvantage in the use of advanced modulation formats.

1.2 All-Optical Orthogonal Frequency Division Multiplexing

The rapid increase in communications bandwidth consumption outlined above has motivated research into spectrally efficient communications which make optimal use of the existing infrastructure. The spectral bandwidth of optical fibre can be subdivided amongst several wavelength channels using a technique known as wavelength division multiplexing (WDM) [14, 15]. Each channel is generated by a single mode laser emitting at the required wavelength and transmitted simultaneously through a single fibre. A minimum spacing is required to reduce interference between channels. The current standardised channel spacing can support spacings between $12.5\,\mathrm{GHz}$ and $100\,\mathrm{GHz}$, and was standardised by the International Telecommunication Union (ITU) in 2012 [16]. The implementation of WDM was aided by the invention of the Erbium-doped fibre amplifier (EDFA) [17], which allowed the simultaneous optical amplification of WDM channels, allowing WDM deployment for long-haul communications.

WDM requires spectrally inefficient guard bands between each communication channel [18]. These guard bands are unused bands of the spectrum which separate channels so as to prevent interference. The guard bands can be removed by creating a "superchannel" [13]. With a superchannel, several optical carriers are combined to create a composite channel of desired capacity.

A superchannel can lead to a significant increase in information spectral density (Gbps/Hz) so that Tbps superchannels can then be created using less total fibre bandwidth [19]. From [13, 19], it is possible to reclaim 25% to 40% of the spectral bandwidth by using optical superchannels. Figure 1.4 illustrates the potential spectral bandwidth that can be reclaimed with the use of an optical superchannel. Optical superchannels can be built using Coherent-WDM (CoWDM) [20]. Alternatively, if each carrier within the superchannel is encoded with data at a modulation frequency equal and phase locked to the carrier separation frequency, interference between carriers is minimised and even greater information spectral density can be achieved. This method is known as all-optical orthogonal frequency division multiplexing (AO-OFDM) [21, 22]. OFDM has already been used to great effect in the radio communications domain in the implementation of 4G cellular networks [23].

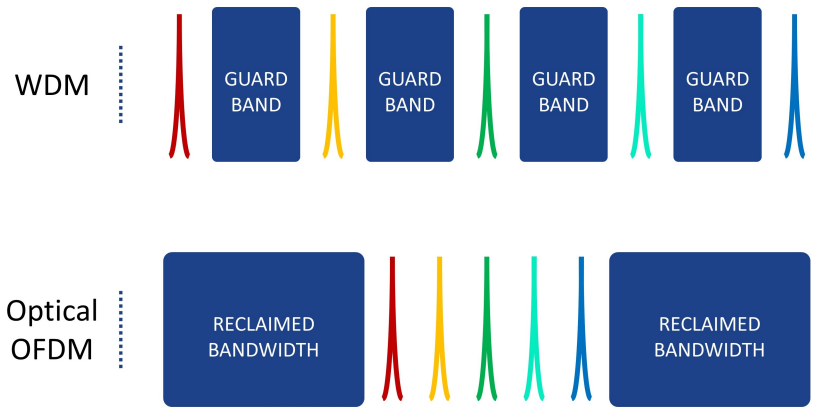

Figure 1.4: Illustration of spectrally inefficient WDM with $50\,\mathrm{GHz}$ channel spacing vs. AO-OFDM with $12.5\,\mathrm{GHz}$ channel spacing.

1.3 Optical Frequency Combs

To consider AO-OFDM for next generation fibre communications, a method of generating evenly spaced, coherent optical wavelengths is required. In the optical domain, this is known as an optical frequency comb [24, 25]. An optical frequency comb is an optical spectrum which consists of equally spaced lines/wavelengths. Such a spectrum is generated from from a regular time domain pulse train with a fixed repetition rate. An example of a typical optical comb spectrum is shown in Figure 1.5.

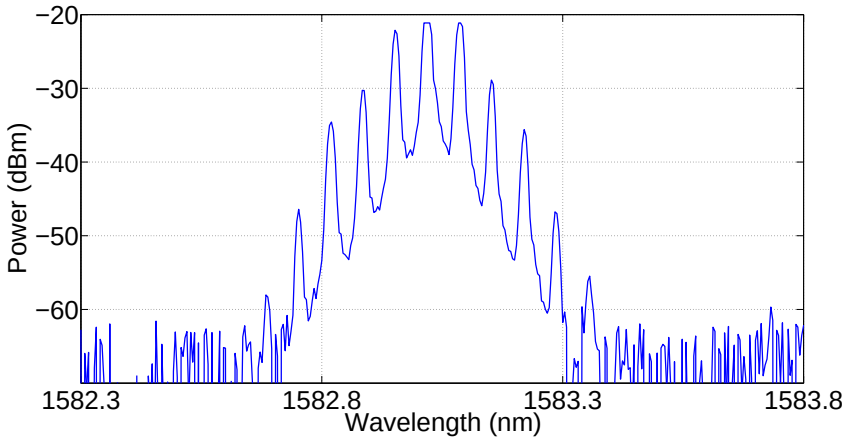

Figure 1.5: Typical optical comb spectrum with $8\,\mathrm{GHz}/{\sim}0.066\,\mathrm{nm}$ line spacing.

Optical comb sources have applications in spectroscopy [26], space-based instruments [27], as well as high speed telecommunications [20, 28]. An

optical comb featuring a narrow linewidth is necessary for advanced modulation formats in Tbit/s coherent superchannel communications systems [29, 30], as outlined in Section 1.1. A schematic of what an AO-OFDM transmitter might look like is shown in Figure 1.6.

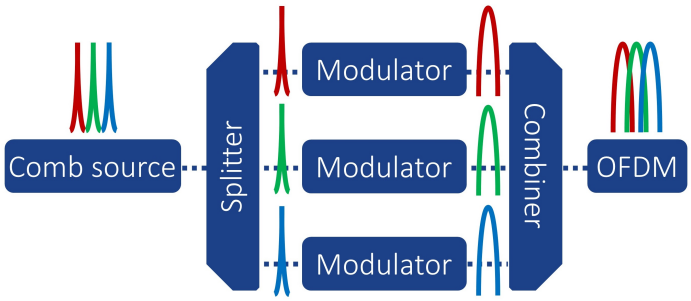

Figure 1.6: AO-OFDM schematic. The lines of the comb are split for data modulation, before recombining for simultaneous transmission.

A monolithically integrated phase and modulation section using quantum well intermixing has been previously demonstrated which showed a linewidth for each comb line of $25\,\mathrm{MHz}$ limited by the laser itself [31], although this linewidth is much too wide to be used to generate coherent superchannels. In comparison, directly modulated (gain-switched) lasers are of interest for generating narrow linewidth combs due to their tunable wavelength, free spectral range (FSR), and ease of integration [32–34]. In contrast to this, comb generation based on mode-locked lasers have a fixed FSR [35], while comb generation based on electro-optic modulators are difficult to integrate with lasers [36]. For these reasons, the subject of this thesis was chosen to be optical comb generation based on gain-switched lasers.

1.4 Gain-Switched Lasers

Gain-switching as a method of generating optical pulses has been a topic of research since the late 70's and early 80's [37, 38]. The premise is simple: directly modulate a semiconductor laser with a high power R.F. signal capable of switching the laser on/off. As the device is pumped and depleted of carriers, the gain parameter of the material switches from positive to negative, hence the

name gain-switching. The comb line spacing can be easily adjusted by changing the R.F. modulation frequency. The operation of gain-switched lasers as comb generators will be examined in more detail in Chapter 2 alongside mode-locked lasers and electro-optic modulators, with a theoretical simulation following in Chapter 3.

When data transmission rates in excess of 10 Gbit/s were required, simple intensity modulation techniques such as OOK were all but abandoned in favor of the advanced modulation formats made available by electro-optic modulators, due to the high fibre penalties induced [39, 40]. These penalties include sensitivity to chromatic dispersion and fibre nonlinearity, which can increase by up to 4 and 16 times respectively when intensity modulation is increased from 10 Gbit/s to 40 Gbit/s [9]. Gain-switching has since seen a resurgence in interest as the many uses for optical combs have come to light [41–44].

An inherent drawback of gain-switching for optical comb generation in semiconductor lasers is the accompanying phase modulation. As the carriers of the laser are modulated, so too is the refractive index of the device. This unwanted phase modulation is known as chirp. There also exists large temporal jitter between pulses produced via gain-switching as each pulse begins with spontaneous emission with a random phase. Also, the noise due to amplified spontaneous emission (ASE) is quadratically dependent on the carrier density, and as the optical power is distributed among the comb lines, the influence of ASE on each comb line is increased [45]. These effects can be measured as an increase in the laser linewidth. Mitigating the additional noise is essential if gain-switched lasers are to be used in the field for AO-OFDM. One method of reducing the noise of a directly modulated laser is injection-locking [46].

1.5 Injection-Locking

Injection-locking was first observed by Christiaan Huygens in the 17^{th} century, who noticed that two pendulum clocks mounted on a common beam would eventually lock frequency with each other. Huygens believed that vibrations carried through the beam were the mechanism behind this phenomenon, and was proven correct not long after [47]. Optical injection-locking is the process whereby one laser, typically called the master laser, injects light into a second laser, typically called the slave laser, and locks the emission frequency of the

slave laser to that of the master. Injection-locking in lasers was first reported theoretically in 1965 [48], with the first experimental demonstration following in 1966 using He-Ne gas lasers [49].

In recent years the field of optical injection-locking has benefited from numerous studies [50–53]. Keen research on the topic has been fueled by the many favourable effects optical injection-locking can have on directly modulated lasers. These effects include;

1. Noise suppression and linewidth reduction [54]
2. Enhanced modulation bandwidth [50]
3. Reduced chirp in directly modulated lasers [55]

A schematic for a typical setup for performing optical injection is shown in Figure 1.7. The master laser injection-locks the slave laser through an isolator, which reduces feedback to the master laser.

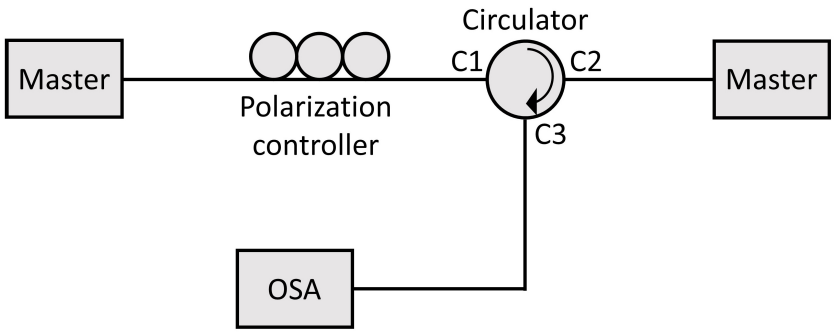

Figure 1.7: Typical injection-locking setup. The master laser injects into the slave through a polarisation controller, and a circulator protecting the master laser from feedback. The output of the slave laser is then analysed using an optical spectrum analyser (OSA).

An example of an injection-locked laser spectrum is shown in Figure 1.8. In this example, one of the low power side modes of the slave laser is injection-locked by a master laser. Suppression of the main lasing mode is observed.

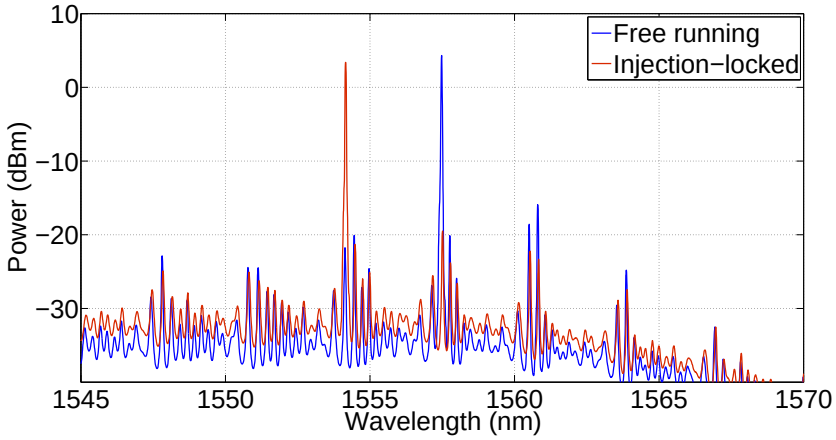

Figure 1.8: Spectra for injection-locked single mode laser. Free running spectrum in blue, with post-injection spectrum in red showing suppression of the main lasing mode.

While injection-locking is typically performed with an isolator between the master and the slave laser using discrete components, optical isolators are not readily available for the case of integrated lasers. Nevertheless, research has been performed for the case of isolator-free optical injection using on-chip integrated lasers with many of the previously stated benefits demonstrated [56–59].

For the purpose of optical comb generation based on gain-switched lasers, injection-locking can aid with the issues of limited laser bandwidth, and phase noise. For this purpose, the photonic integration of two lasers on a single chip was investigated.

1.6 Photonic Integration

Photonic integration is the integration of discrete optical components, such as lasers, splitters, and modulators, on to a single chip. Photonic integration was first proposed in 1969 [60], and was expected to mirror the explosive growth the electronics industry experienced with the advent of integrated circuits [61]. Unfortunately photonic integration has lagged behind its electronic counterpart, largely due to a lack of standardization in the field [62]. Material systems vary depending on the applications, with devices such as lasers and amplifiers requiring active materials, while devices such as modulators and waveguides requiring passive materials, making it difficult to arrive at a "one size fits all" solution to photonic integration. Efforts have been made to address this issue, such as the generic foundry model introduced by

TU Eindhoven, which seeks to standardise a few processes for multi-project development [63].

Progress in the field over the last 20 years include; the integration of a laser with an electroabsortpion modulator [64], the integration of a laser with an optical amplifier [65], a 12 channel optical controller [66], an 8 channel wavelength demultiplexor [67], a 10 channel laser array [68]. The first commercial PICs appeared in 2005 from Infinera with their dense wavelength division multiplexed (DWDM) transmitter and receiver PICs [69]. An example of a PIC designed for coherent optical comb line filtering is shown under test in Figure 1.9 [70, 71].

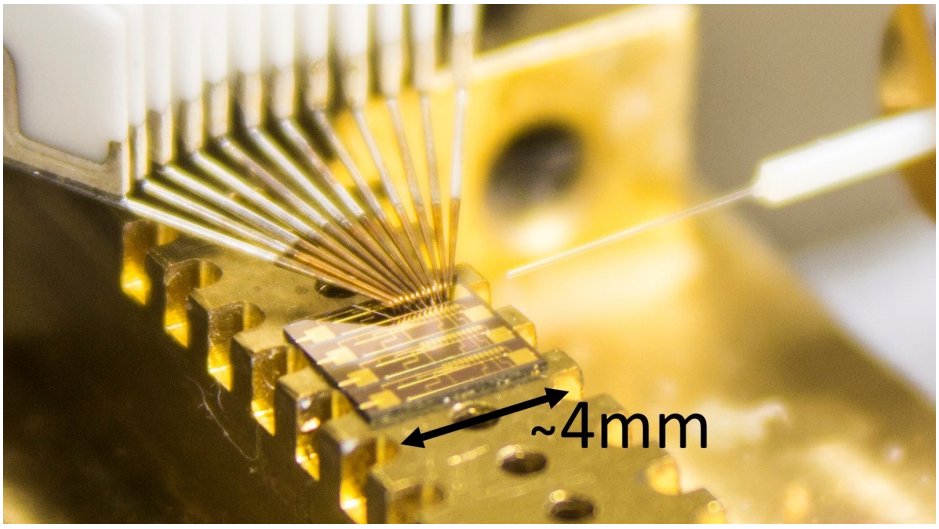

Figure 1.9: Photonic integrated circuit under test. This particular circuit integrates several lasers, splitters, and combiners, measuring approximately $4\,\mathrm{mm}$ in length. A multi-contact probe and lensed optical fibre for testing purposes are shown [70, 71].

The allure of photonic integration is simple; by integrating optical components onto a single chip, savings can be made on overall size, power consumption, fabrication cost, and packaging cost. As optical transmitter and receiver demands and complexity continue to rise, photonic integration could be a key technology in the future of fibre communications [13].

There are several disciplines for integrating photonic devices onto a single chip. Silicon photonics is one such field, seeking to integrate photonic devices on silicon substrates [72]. Silicon is transparent at optical communications wavelengths ($1.3\,\mu\mathrm{m}$, $1.55\,\mu\mathrm{m}$) making it ideal for waveguide interconnects. As silicon is an indirect band gap material, a silicon laser is not yet an option. Silicon photonics benefits from existing CMOS foundries and would allow for the integration of photonic devices with electronics. Photonic devices could be

developed on silicon substrates using wafer bonding to bond photonic device material to silicon substrates [73], or by transfer printing devices [74]. The integration of devices on a single common substrate is known as monolithic integration.

Indium-phosphide (InP) substrates are used for the development of devices which lase at $1.55\,\mu\mathrm{m}$. This is the wavelength of choice for long-reach communications as $1.55\,\mu\mathrm{m}$ corresponds to the region of lowest loss in an optical fibre. Suitable direct band gaps can be engineered using InGaAsP or AlInGaAs compounds lattice matched to InP. Several techniques are employed to integrate passive structures on InP based on material regrowth; butt-joint regrowth, selective area regrowth, offset quantum wells, dual quantum wells, and quantum well intermixing. These techniques are summarised in [75]. The devices designed for this thesis employ regrowth-free monolithic integration [76].

1.7 Thesis Motivation

In this chapter, an overview of fibre optic communications has been given. As both the number of users and the bandwidth required per user continues to grow, so too must the technology underpinning the worldwide web. Advanced modulation formats can only drive the increase in bit rate so far, before serious fibre penalties are incurred for long-reach transmission. Therefore it is imperative to explore alternative solutions.

AO-OFDM could address the current need for Tbit/s optical transmitters by significantly increasing the spectral efficiency of the communications spectrum. In order for AO-OFDM to become a contender for the next generation of optical transmitters, coherent low-linewidth optical comb sources are required. A brief summary of the gain-switching technique was given, as well as advantages/disadvantages of other methods. A more rigorous discussion will follow in Chapter 2. An overview of optical injection-locking as a method for reducing phase noise in directly modulated lasers was given.

The purpose of this work was the development of an integrated low-linewidth optical comb source. The three main objectives were: to use gain-switching to generate an optical comb, to use injection-locking to reduce the laser linewidth of the comb, and to use photonic integration to reduce size, cost, and power consumption. Gain-switching was selected as the comb generation method due to gain-switched lasers tunable FSR, and ease of integration. Injection-locking was used to stabilise the gain-switched laser, as gain-switching is known to generate broad linewidth combs. Photonic integration was used to integrate the gain-switched laser with the injection-locking laser on to a single chip, reducing the need for optical interconnects between lasers. Regrowth-free monolithic integration was used to minimize fabrication costs.

The work presented in this thesis describes novel designs for low-linewidth optical comb sources based on injection-locked gain-switched lasers. Each design was extensively characterised using a purpose built test setup. Several device geometries were explored, with low-linewidth combs generated from each. Simulations were also carried out to theoretically investigate the phase noise of gain-switched lasers vs. injection-locked gain-switched lasers.

1.8 Thesis Outline

This thesis is outlined as follows;

In Chapter 2, gain-switching, and two additional methods of comb generation are described in more detail; mode-locking and electro-optic modulation. Advantages and disadvantages of each are outlined, with reasons given for selecting gain-switched lasers for this work.

In Chapter 3, a theoretical model of injection-locked gain-switched lasers is presented using the single mode semiconductor rate equations. The model was used to simulate the linewidth of a single mode gain-switched laser, both with and without optical injection-locking. From this model, the benefits of injection-locking a gain-switched laser are demonstrated.

Chapter 4 contains the basic characterization of the ridge waveguide lasers used for this work. Features such as etched facets are characterised for the purpose of integration. The main fabrication steps involved in the processing of these devices are illustrated.

Optical comb generation experimental results can be found in Chapter 5. The structure of each device is given, along with descriptions of the experimental procedures performed. This chapter contains the main experimental findings of this thesis.

In Chapter 6, it is suggested how this work can be expanded and improved on in the future.

Chapter 2

Comb Generation Methods

With an overview of the fibre optic communications network given in the previous chapter, the following chapter gives details on comb generation methods. An optical comb is a requirement for AO-OFDM. Several methods can be used for the generation of optical combs from semiconductor devices, each with advantages and disadvantages. The three main methods shall be outlined in this chapter: mode-locking, electro-optic modulation, and gain-switching. For AO-OFDM, a tunable comb line spacing would be desirable as to allow customization of the data transmission bit rate depending on network requirements. Following the details given in this chapter, the reasons for pursuing gain-switched optical comb sources shall be clear. Details on mode-locked lasers are presented first, followed by electro-optic modulation, and finally, gain-switching.

2.1 Mode-Locked Lasers

Mode-locking is a technique where the modes of a multimode laser lock phase with each other, resulting in a pulsed optical output [77]. A multimode Fabry-Pérot laser has a longitudinal mode spacing given by the equation,

$$\Delta\nu = \frac{c}{2nL} \tag{2.1}$$

where c is the speed of light, n is the refractive index, and L is the length of the cavity. This can be expressed in angular frequency as,

$$\Delta\omega = \frac{2\pi c}{2nL} = \frac{\pi c}{nL} \tag{2.2}$$

The total electric field is given by,

$$E_T(t) = \sum_{m=-(N-1)/2}^{(N-1)/2} a_m(t) e^{j(\omega_0 t + m\Delta\omega t + \phi_m(t))} \tag{2.3}$$

where $E_T(t)$ is the total electric field, N is the total number of modes in the cavity, $a_m(t)$ is the amplitude, $\omega_0 + m\Delta\omega$ is the angular frequency, and $\phi_m(t)$ is the phase.

Under mode-locking conditions, $\phi_m(t)$ is equal to some constant. Taking $a_m(t) = 1$, and $\phi_m(t) = 0$ we get,

$$E_T(t) = e^{j\omega_0 t} \sum_{m=-(N-1)/2}^{(N-1)/2} e^{jm\Delta\omega t} \tag{2.4}$$

Using,

$$\sum_{m=-(N-1)/2}^{(N-1)/2} e^{jmx} = \frac{1 - exp(\frac{jNx}{2})}{1 - exp(\frac{jx}{2})} \tag{2.5}$$

and simplifying, the total electric field is given by,

$$E_T(t) = e^{j\omega_0 t} \frac{exp(\frac{jN\Delta\omega t}{2}) sin(\frac{N\Delta\omega t}{2})}{e(\frac{j\Delta\omega t}{2}) sin(\frac{\Delta\omega t}{2})} \tag{2.6}$$

The total power is given by,

$$P_T(t) =< E_T^*(t) E_T(t) > \tag{2.7}$$

$$P_T(t) = \frac{sin^2(\frac{N\Delta\omega t}{2})}{sin^2(\frac{\Delta\omega t}{2})} \tag{2.8}$$

Thus when the modes in a multimode laser are phase locked, the total power is a periodic function. The total power can easily be plotted in Matlab. A plot of the output power vs. time for 5 locked modes is shown in Figure 2.1, and for 20 modes as seen in Figure 2.2.

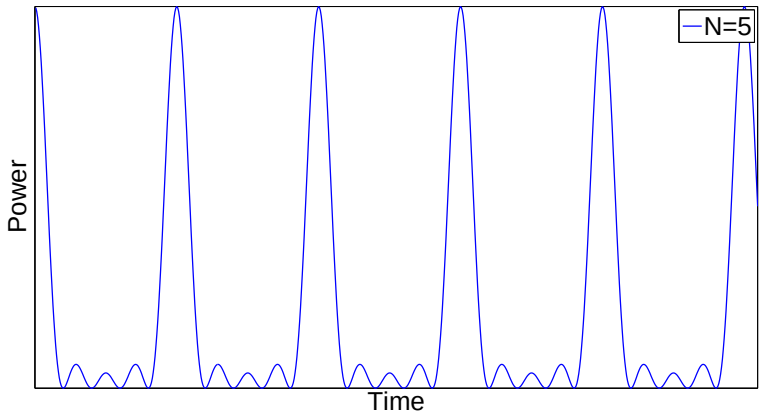

Figure 2.1: Optical pulse train resulting from 5 locked modes.

The pulse repetition rate T is given by,

$$T = \frac{2\pi}{\Delta\omega} \tag{2.9}$$

with the duration of a single pulse given by,

$$t_p = \frac{2\pi}{N\Delta\omega} \tag{2.10}$$

The pulse width is shown to decrease with increasing number of phase locked modes. A comparison between Figure 2.1 and Figure 2.2 confirms this. Thus mode-locked lasers can be used to obtain very short optical pulses, on the order of $1\,\mathrm{ps}$ [35].

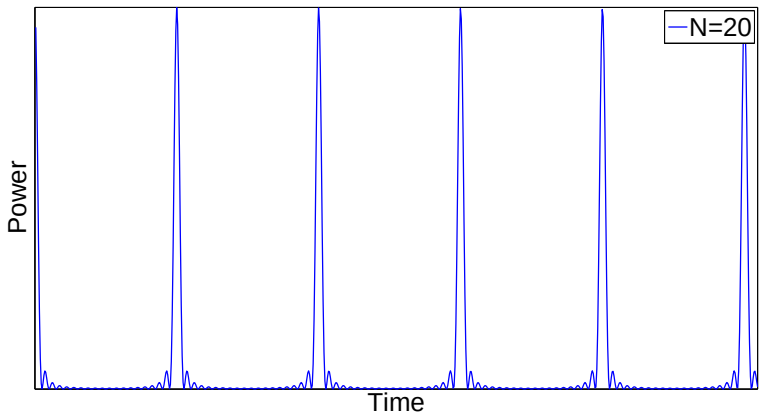

Figure 2.2: Optical pulse train resulting from 20 locked modes.

The pulse separation is seen to be a function of $\Delta\omega$, which is itself a function of L. By doubling the length of the cavity, the pulse separation is doubled also.

This is shown in Figure 2.3.

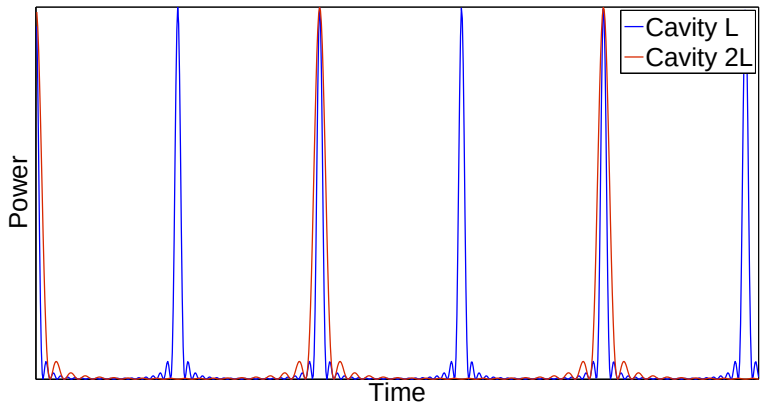

Figure 2.3: Pulse train for different length cavities. Repetition rate can be increased by decreasing the length of the cavity.

A drawback of mode-locked lasers is highlighted by this analysis: the repetition rate, and thus the comb line spacing, is set by the cavity length. Precise cavity design is required for the desired line spacing.

Phase-locking between the modes of a multimode semiconductor laser can be achieved either actively or passively [77, 78]. Active methods involve either amplitude (AM) or phase modulation (PM). Passive mode-locking involves the use of a saturable absorber (SA) to generate pulses [35, 79], although passive mode-locked lasers experience reduced phase correlation between modes on opposite edges of the spectrum. Passively mode-locked quantum dot/dash lasers rectify this issue, demonstrating excellent phase correlation between all modes, and a broad comb spectrum. [80]. Mode-locking has demonstrated the generation of broad optical combs with a large possible comb line spacing in excess of $92\,\mathrm{GHz}$ [81]. While mode-locking remains an essential field for the generation of ultra short pulses [82], the lack of tunability of the repetition rate / comb line spacing make mode-locking a less than ideal approach for AO-OFDM. Mode-locked lasers can also suffer from mode partition noise amongst individual modes, leading to an increase in linewidth (typically in the MHz range).

2.2 Electro-Optic Modulation

Electro-optic modulation has been the de facto method for modulation speeds in excess of $10\,\mathrm{GHz}$ [83–85]. Electro-optic modulators typically utilise the

Pockels effect, which states that an applied electric field will cause a change in the refractive index of a material [86]. Electro-optic modulators are therefore phase modulators. By far the most popular use is in the design of Mach-Zehnder amplitude modulators (MZMs). By splitting the input optical signal between two arms, the relative phase can be adjusted to create constructive/destructive interference upon recombination of the signals. MZMs can also utilise the quantum-confined Stark effect (QCSE) [87]. Thus MZMs can be used to generate optical combs by modulating an optical signal on/off. An MZM as an optical comb generator was demonstrated experimentally, the setup for which is shown in Figure 2.4.

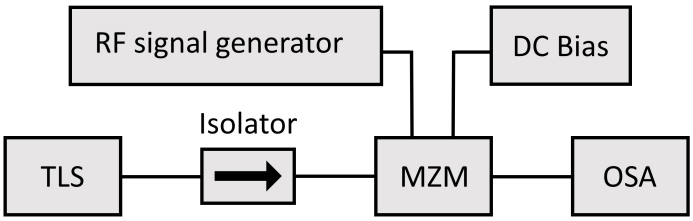

Figure 2.4: Experimental setup for modulating a tunable laser source (TLS) with a Mach-Zehnder modulator (MZM).

A tunable laser source (TLS) input a single wavelength at $1563.05\,\mathrm{nm}$ to the MZM, an Oclaro PowerBit SD40 with a bandwidth of $33\,\mathrm{GHz}$. The MZM was driven by a an RF signal generator and a DC bias. The modulating frequency was set to $25\,\mathrm{GHz}$ at $25\,\mathrm{dBm}$, with the DC bias set to $2.6\,\mathrm{V}$ to bias the MZM at the null point. The optical comb generated is shown in Figure 2.5.

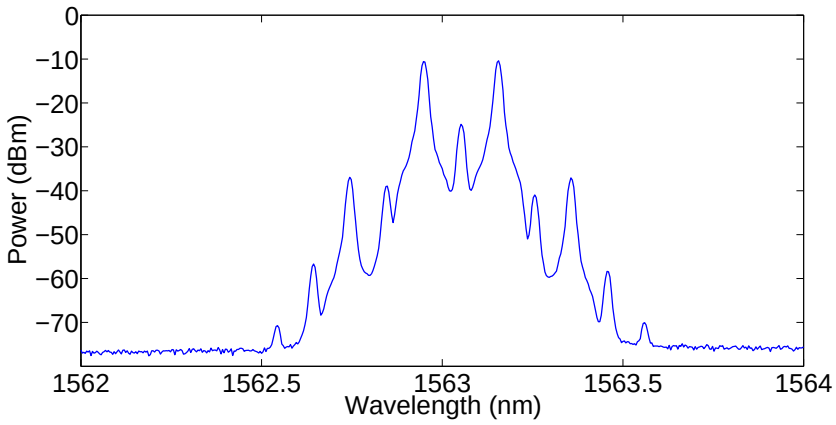

Figure 2.5: Optical comb generated from MZM with $25\,\mathrm{GHz}$ line spacing. The carrier is suppressed as the MZM is biased at the null point.

MZMs can be used to generate broad, tunable optical combs, with as many as 11 lines [28]. There has been a great deal of interesting work done on this topic in recent years, see references [88, 89]. While MZMs show strong potential as comb generators for AO-OFDM, there are some drawbacks. MZMs can be difficult to integrate with lasers, and typically have a high insertion loss. The design of MZMs is also more complex, and also occupies a large area on a PIC when compared to a gain-switched laser. MZMz also suffer from bias drift, leading the transfer function to drift as a function of time. As a result, MZMs require some form of feedback in order to maintain the correct bias for a specific point on the transfer function.

2.3 Gain-Switching

Gain-switching is the direct modulation of a laser with a high power RF signal. To understand how this can be used for comb generation, we need to look at the relaxation oscillations for a semiconductor laser. Relaxations oscillations occur when a semiconductor laser is switched on, or perturbed during steady state operation. Due to the interplay between carriers and photons, the laser does not immediately return to steady state operation. Relaxation oscillations are most obvious when the laser is abruptly switched on. The onset of stimulated emission generates an optical pulse that rapidly depletes carriers, faster than they can be added to the system. The relaxation oscillation frequency, also known as the resonance frequency, can be determined by a small signal analysis of the carrier and photon rate equations for a single mode laser. These equations are given by [45];

$$\frac{dN}{dt} = \frac{I}{eV} - R(N) - a(N - N_{tr})S \tag{2.11}$$

$$\frac{dS}{dt} = \left(a\Gamma(N - N_{tr}) - \frac{1}{\tau_p}\right)S + \beta BN^2 \tag{2.12}$$

where N is carrier density, S is photon density, I is the current applied, e is the electron charge, V is the volume of the active region, R is the rate of carrier recombination, a is the differential gain (the rate at which gain increases with more carriers), N_{tr} is the carrier density at transparency, Γ is the confinement factor, τ_p is the photon lifetime, β is the fraction of spontaneous emission coupling into the lasing mode, and B is the bimolecular recombination coefficient. A small signal analysis of these equations gives the resonance

frequency. Several equivalent expressions for the resonance frequency can be seen below [86];

$$\omega_\tau^2 = \frac{1}{\tau_s \tau_p} = \frac{\nu_g a S_0}{\tau_p} = \frac{\nu_g a \Gamma \eta_i (I - I_{th})}{eV} \tag{2.13}$$

where ω_τ is the angular relaxation oscillation frequency, τ_s is the stimulated carrier lifetime, ν_g is the group velocity, S_0 is the steady state photon density, η_i is the internal quantum efficiency, and $(I - I_{th})$ is the bias current above threshold. A typical plot of the relaxation oscillations of carrier and photon density experienced by a laser as it is switched on is shown in Figure 2.6.

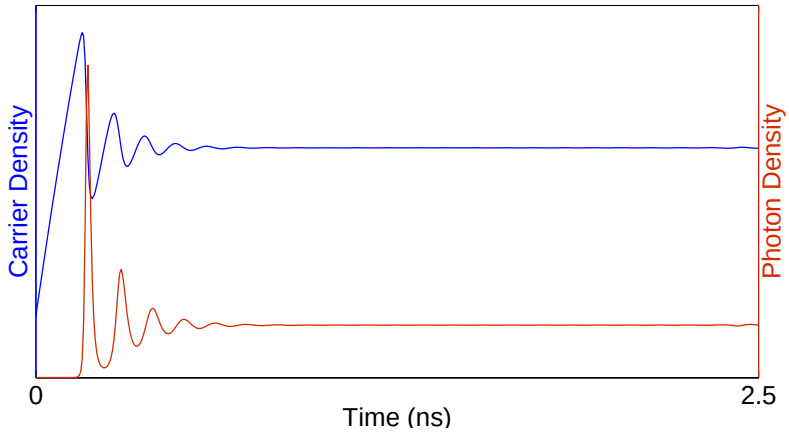

Figure 2.6: Typical carrier and photon density turn-on plots for a semiconductor laser showing relaxation oscillations on the order of a few hundred picoseconds.

The carrier density is shown to steadily increase before rapidly dropping as stimulated emission generates an optical pulse. These oscillations continue before settling after a few nanoseconds. The idea behind gain-switching is to excite the first pulse of the relaxation oscillations, cutting the power before the second pulse can be generated. An example of the pulse train resulting from this method is shown in Figure 2.7.

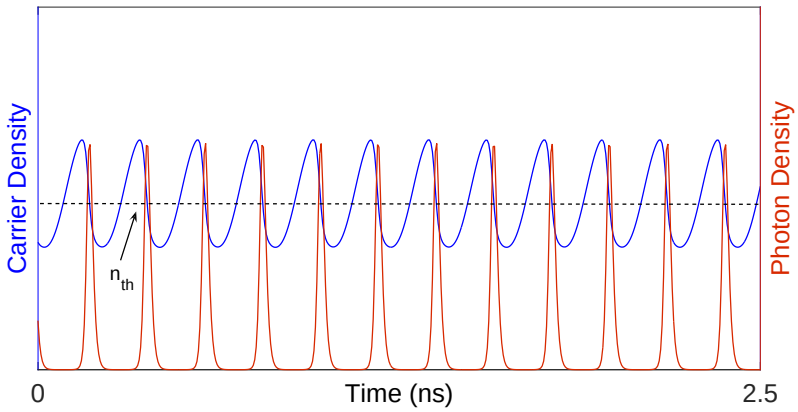

Figure 2.7: Gain-switched carrier and photon density pulse train.

The regular time domain pulse train produced by gain-switching appears as an optical comb in the frequency domain. The pulse spacing, and therefore the comb line spacing of a gain-switched laser can be changed by adjusting the frequency of the high power RF signal. The evolution of the sinusoidal current bias, the carrier density, and the photon density is shown in Figure 2.8 for the generation of one pulse. From this illustration, it is shown how the the carrier density builds above threshold before being rapidly depleted by stimulated emission and the cycle begins again.

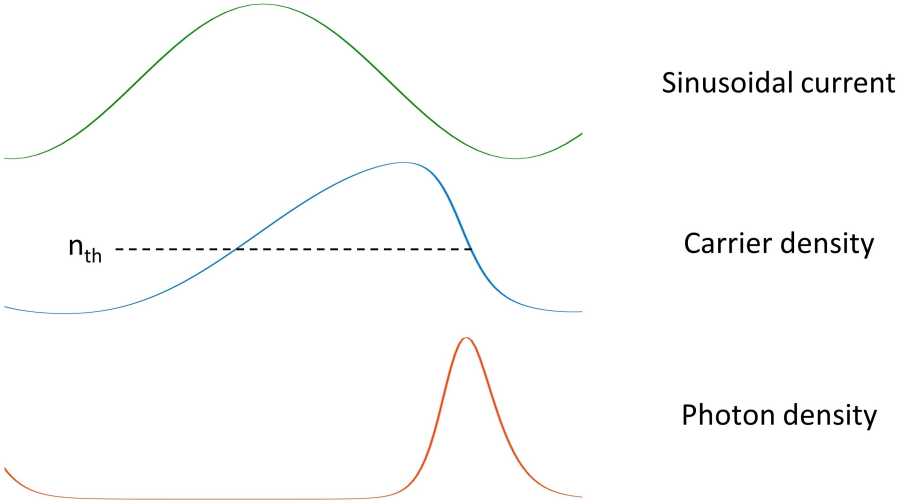

Figure 2.8: The evolution of the sinusoidal current bias, the carrier density, and the photon density throughout the generation of one pulse.

Coupled with the simplistic design, gain-switched lasers show strong potential to act as comb generators for AO-OFDM. The major drawbacks being the increase in linewidth during gain-switching, and the limited modulation bandwidth of lasers [90]. In Chapter 3, the linewidth is shown to decrease

under injection-locking from a low linewidth master laser. In Chapter 5, the modulation bandwidth is shown to improve somewhat under optical injection-locking. This effect is discussed further in Chapter 6.

2.4 Conclusion

In this chapter the 3 main techniques were outlined for the generation of optical combs; Mode-locking, electro-optic modulation, and gain-switching. Mode-locked lasers were shown to be excellent devices for the generation of short optical pulses, but the fixed repetition rate limit their use in flexible AO-OFDM networks. Electro-optic modulators such as MZMs allow for the tuning of the comb line spacing, though the design of such devices is complex, and not readily integrable with a laser. Gain-switched lasers can generate flexible optical combs, while also having a relatively straightforward design. The issue of limited bandwidth can be improved through the use of optical injection-locking, provided the device is not RC limited.

A theoretical model of a gain-switched laser, both with and without injection-locking, is discussed in the following chapter, Chapter 3. The noise properties of gain-switched lasers are analysed to verify optical injection from a low-noise master laser can mitigate the inherent noise issues in gain-switched lasers.

Chapter 3

Theoretical Analysis of Phase Noise

Three methods of comb generation were outlined in Chapter 2. Gain-switching was selected as the method of choice for this thesis due to the method's device design simplicity, and tunable comb line spacing. One of the issues with gain-switching is the inherent noise increase as a result of direct modulation. In this chapter, a theoretical analysis of the phase noise in gain-switched lasers is performed using the single mode semiconductor laser rate equations [91] [92], both with and without injection-locking. The rate equations are a set of ordinary differential equations (ODEs) which can be used to theoretically study the dynamics of a semiconductor laser, and are solved numerically. They provide a mathematical insight into the operation of a semiconductor laser, which can be used to inform experiment.

The rate equations model the carrier density, photon density, and the phase of a semiconductor laser. Carrier density is increased with the injection of electric current through the laser. Carrier and photon density are coupled via stimulated emission, which acts to deplete carriers and increase photon density once the device is biased above threshold. Phase noise is coupled with the carrier density as the refractive index of semiconducting material is tied to carrier density. Thus, when directly modulating a laser, as is the case with gain-switching, an increase in phase noise is to be expected. Low phase noise is a desirable property for telecommunications as it is required for higher order data modulation formats [12]. The equations do not account for the heating effects that occur in real devices.

The equations were solved in Matlab using the built-in ordinary differential equation solver ODE45. The solver uses the 4^{th} order Runga-Kutta method to solve the equations for a given set of initial conditions $y(0)$, over time span $tspan$.

3.1 Without Injection-Locking

3.1.1 The Rate Equations

The rate equations for a single mode laser consists of 3 equations which describe the dynamic flow of carriers, photons, and phase in the laser. The rate equations are given by [45],

$$\frac{dN}{dt} = \frac{I(t)}{eV} - R(N) - a(N - N_{tr})S + F_N(t) \tag{3.1}$$

$$\frac{dS}{dt} = \left(\Gamma a(N - N_{tr}) - \frac{1}{\tau_p}\right) S + \beta BN^2 + F_S(t) \tag{3.2}$$

$$\frac{d\phi}{dt} = \frac{1}{2}\Gamma\alpha_H a(N - N_{tr}) + F_\theta(t) \tag{3.3}$$

where N is carrier density, S is photon density, and ϕ is phase. All other parameters are defined and quantified in Table 3.1.

$R(N)$ is the rate of carrier recombination including the non-radiative, bimolecular, and Auger recombination and is given by Equation (3.4).

$$R(N) = AN + BN^2 + CN^3 \tag{3.4}$$

τ_p is the photon lifetime, a measure of the average time a photon exists in the laser cavity, and can be expressed as [93],

$$\tau_p = \frac{L}{\nu_g \log\sqrt{\frac{1}{R_1 R_2}}} \tag{3.5}$$

where L is the length of the cavity, ν_g is the group velocity in the material, and R_1 and R_2 are the cavity mirror reflectivities. Intrinsic losses in the cavity have been excluded for simplicity. The photon lifetime is the product of the round trip delay and the photon loss during the round trip for a cold cavity (gain $= 0$). The photon lifetime is an important parameter in determining the resonance frequency of the simulated laser.

The β parameter represents the fraction of the spontaneous emission coupled into the lasing mode, and has been used in this work to artificially adjust the linewidth of the simulated lasers in the model.

$F_N(t)$, $F_S(t)$, and $F_\theta(t)$ are Langevin noise sources [91] based on Gaussian

random variables and are defined below,

$$F_N(t) = \sqrt{2RB_{sim}}\, x_N(t) \tag{3.6}$$

$$F_S(t) = \sqrt{\beta 2SBN^2B_{sim}}\, x_S(t) \tag{3.7}$$

$$F_\theta(t) = \sqrt{\frac{\beta SBN^2B_{sim}}{2}}\, x_\theta(t) \tag{3.8}$$

B_{sim} is the simulation bandwidth, given by the inverse of the sampling period. $x_N(t)$, $x_S(t)$, $x_\theta(t)$, are Gaussian random variables with zero-mean unity-variance. These white noise sources simulate the random generation of spontaneously emitted photons in the cavity which are distributed uniformly across all frequencies.

Table 3.1: Parameter definitions and values

Parameter	Definition	Value
V	Volume of active region	$3.75 \times 10^{-17}\ m^3$
A_{eff}	Effective modal area	$2.25 \times 10^{-14}\ m^2$
L	Length of device	$500 \times 10^{-6}\ m$
Γ	Confinement factor	0.3
R_1, R_2	Mirror reflectivity	0.3
a	Differential gain	$5 \times 10^{-13}\ m^3 s^{-1}$
N_{tr}	Carrier density at transparency	$1 \times 10^{-24}\ m^{-3}$
τ_p	Photon lifetime	$4.8858 \times 10^{-12}\ s$
β	Fraction of spontaneous emission coupled into lasing mode:	
	slave	1×10^{-4}
	master	1×10^{-6}
a_H	Linewidth enhancement factor	4
A	Non-radiative recombination rate	$1 \times 10^{9}\ s^{-1}$
B	Bimolecular recombination coefficient	$1 \times 10^{-16}\ m^3 s^{-1}$
C	Auger recombination coefficient	$1 \times 10^{-41}\ m^6 s^{-1}$
ν_g	Group velocity	$8.5 \times 10^{7}\ m\ s^{-1}$
v	Emission frequency	$2\ THz$
h	Planck's constant	$6.62 \times 10^{-34}\ m^2 kg/s$
e	Electron charge	$1.602 \times 10^{-19}\ C$
t_1	Start time	$100 \times 10^{-9}\ s$
t_2	End time	$150 \times 10^{-9}\ s$
dt	Simulation time step	$5 \times 10^{-12}\ s$
$tspan$	Simulation time span	$50 \times 10^{-9}\ s^{-1}$
B_{sim}	Simulation bandwidth	$1/(5 \times 10^{-12})\ s^{-1}$

Equation (3.1) represents the change in carrier density in the cavity over time, which is caused by: the inward flow of carriers due to pumping current, the carriers lost to non-radiative, bimolecular, and Auger recombination, and carrier loss due to stimulated emission. A plot of carrier density vs. time is shown in Figure 3.1a for a step input current of $50\,\mathrm{mA}$. $50\,\mathrm{mA}$ was chosen as this is a typical laser bias, and is well above threshold, as shown in Figure 3.2b. Characteristic oscillations of the carrier density is shown as the laser is switched on before settling to a steady value. These are the relaxation oscillations of the system.

Equation (3.2) represents the change in photon density over time. Photons are generated through stimulated and spontaneous emission, and lost through scattering in the waveguide, and emission from the cavity. Photon density vs. time at $50\,\mathrm{mA}$ is shown in Figure 3.1b. The corresponding relaxation oscillations in the carrier density is shown in the photon density as the device turns on.

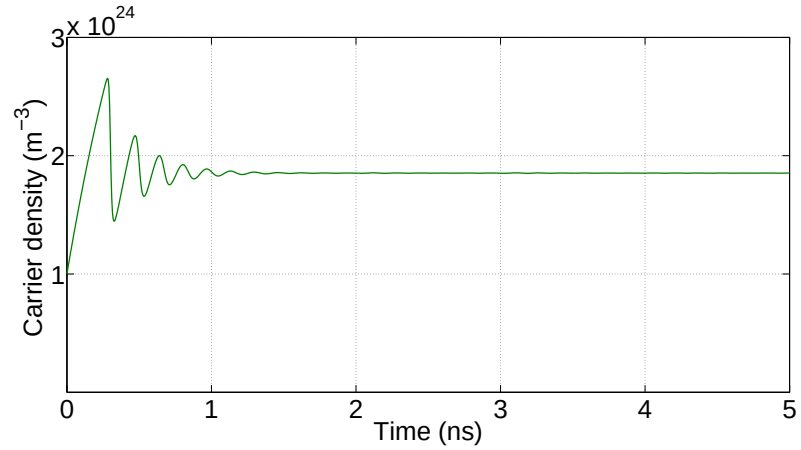

(a)

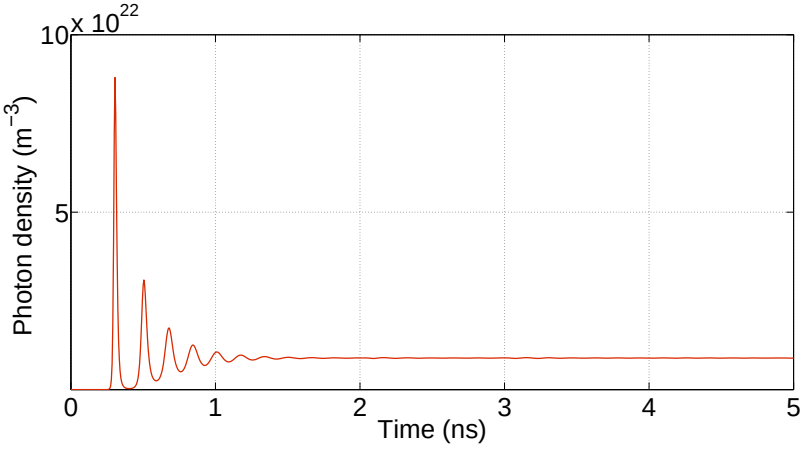

(b)

Figure 3.1: (a) Carrier density vs. time (b) Photon density vs. time, calculated from the rate equations. Relaxation oscillations is shown in both plots as the laser is switched on.

A plot of the carrier density vs. input current for a linearly increasing current is shown in Figure 3.2a. The carrier density clamps to a fixed value once the gains equal the losses, with all further injected carriers contributing to stimulated emission, as is shown in Figure 3.2b. Figure 3.2b shows how optical power varies with increasing current.

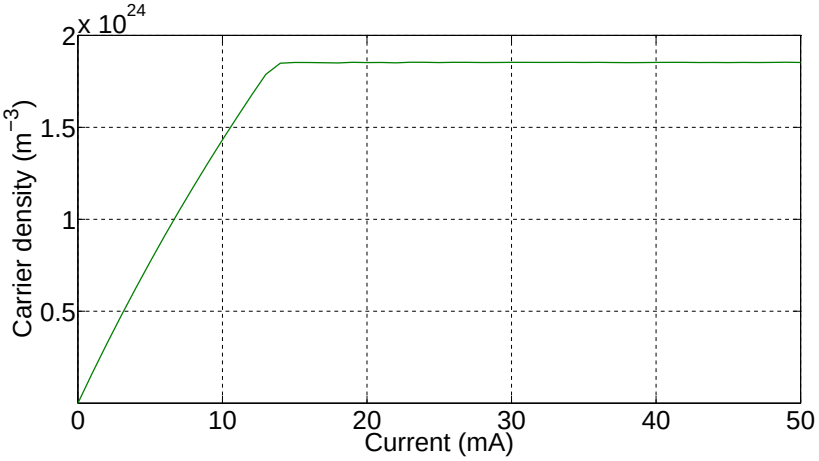

(a)

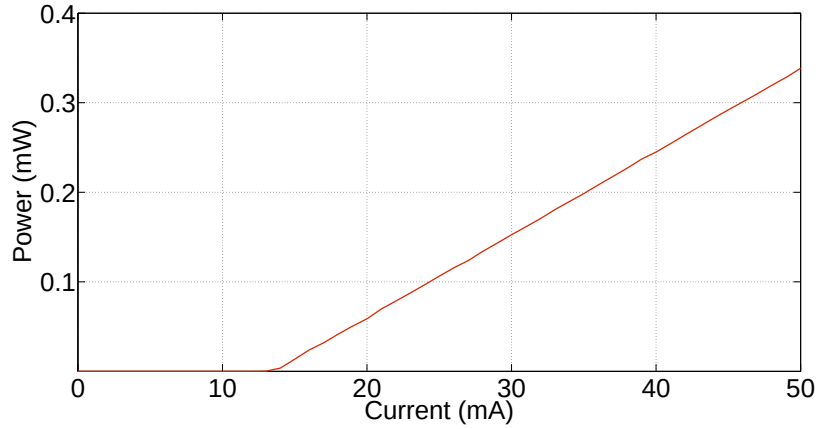

(b)

Figure 3.2: (a) Carrier density vs. input current. Carrier clamping is shown at the threshold current. (b) Optical power vs. input current.

The optical power in Watts can be calculated from the photon density using Equation (3.9).

$$P = \frac{1}{2} K \nu_g A_{eff} h v S(t) \tag{3.9}$$

$K = 0.3$ is the fraction of photons emitted from the cavity. The factor of a half is included as the laser emits from both sides, with only one side observed in this case. The average value of the steady state carrier and photon densities at each value of current was used to generate each plot. From Figures 3.2a and 3.2b, the threshold current for the simulated laser can be estimated as $14\,\mathrm{mA}$.

3.1.2 Phase Noise

The phase noise of a laser is directly related to the power spectral density of the frequency noise. A general waveform $S(t)$, with amplitude A, angular frequency ω, time t, and phase $\phi(t)$ can be expressed as,

$$S(t) = Acos(\omega t + \phi(t)) \tag{3.10}$$

The instantaneous angular frequency is given by

$$\omega_i = \frac{d}{dt}(\omega t + \phi(t)) \tag{3.11}$$

$$\omega_i = \omega_0 + \frac{d\phi}{dt} \tag{3.12}$$

$$\Delta\omega = \frac{d\phi}{dt} \tag{3.13}$$

Thus, the instantaneous frequency relative to the central frequency is,

$$\Delta v = \frac{1}{2\pi}\frac{d\phi}{dt} \tag{3.14}$$

Equation 3.14 can be used to obtain a frequency noise (FN) spectrum for the laser. The FN spectrum can then be calculated from the Fourier transform of Equation (3.14), and is a measure of how noise is distributed across frequencies.

$$FN = \frac{1}{T}|\int_0^T \Delta v(\tau)e^{-j\omega\tau}d\tau|^2 \tag{3.15}$$

At low frequencies carrier/index fluctuations contribute to a higher white noise level [94], thus the average value of the low frequency ($< 1\,\mathrm{GHz}$) of the FN spectrum times π is equivalent to the linewidth of the laser [95].

The phase derivative, as calculated from Equation 3.3, for two lasers of length $500\,\mu\mathrm{m}$ with β parameters of 10^{-4} and 10^{-6} was plotted in Figure 3.3. The current was set to $50\,\mathrm{mA}$ and the simulation was run for $50\,\mathrm{ns}$. The initial $10\,\mathrm{ns}$ were truncated to remove the relaxation oscillations. The instantaneous variations in phase is shown due to noise in the system, with notably lower phase variations for a lower value of β.

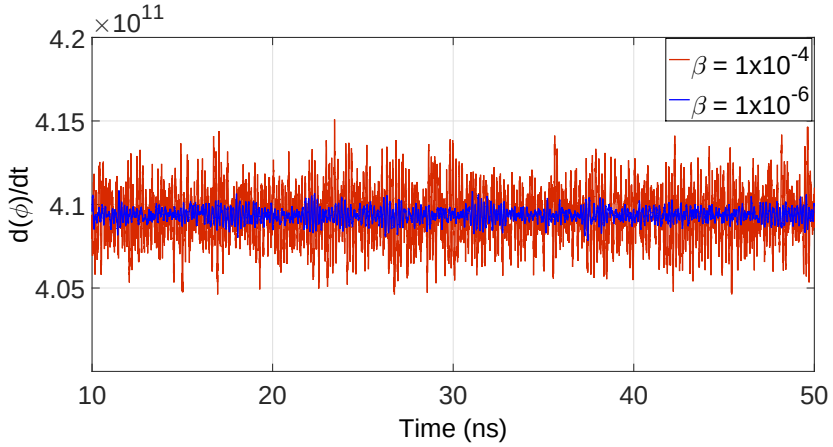

Figure 3.3: Phase derivative for two $500\,\mu\mathrm{m}$ lasers with β parameters of 10^{-4} and 10^{-8}.

An FN spectrum was then calculated from Equation 3.3, using Equation 3.15, for the same conditions used for Figure 3.3. 10 averages were taken to smooth the trace, and a 2.5% smoothing function was also applied. The FN spectrum was plotted in Figure 3.4. The increase in FN is clearly seen as the value of β is increased.

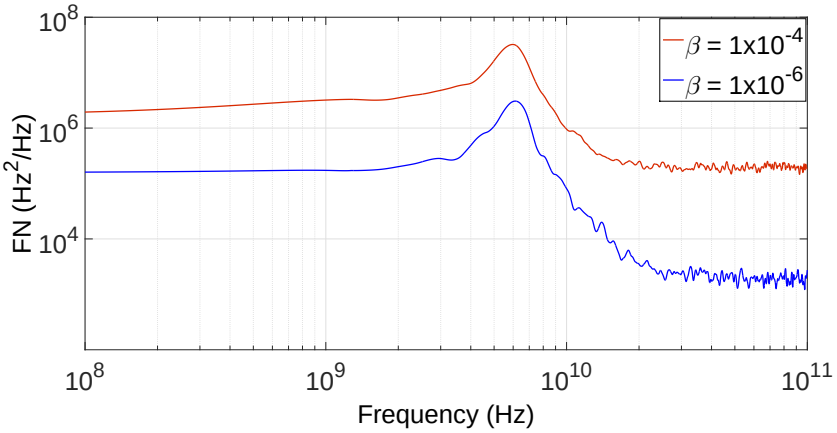

Figure 3.4: FN spectrum for two $500\,\mu\mathrm{m}$ lasers with β parameters of 10^{-4} and 10^{-6}. The peak at $6\,\mathrm{GHz}$ corresponds to the resonance frequency of the device.

Two distinct noise levels can be seen either side of a peak in the spectrum. The peak corresponds to the resonance frequency of the device. The resonance frequency is a measure of how fast a laser can respond optically to a carrier fluctuation, and sets a limit to the modulation speed of directly modulated lasers [96, 97]. Fluctuations in the carrier density which occur below and around the resonance frequency contribute to a higher noise level due to amplitude-phase coupling. At frequencies above the resonance frequency only the spontaneous emission contribution to the frequency noise is present.

3.1.3 Including Gain-Switching with the Rate Equations

Gain-switching was included in the simulated laser by adding a cosine term to the current, $I = I + I_m cos(2\pi f)$, where $I = I_m = 50\,\mathrm{mA}$ and $f = 5\,\mathrm{GHz}$ or $4\,\mathrm{GHz}$. While gain-switched, the laser is fundamentally a single mode laser, therefore the rate equations are still applicable. The FN spectrum for this configuration is plotted in Figure 3.5 along with the free running FN spectrum, with $\beta = 10^{-4}$.

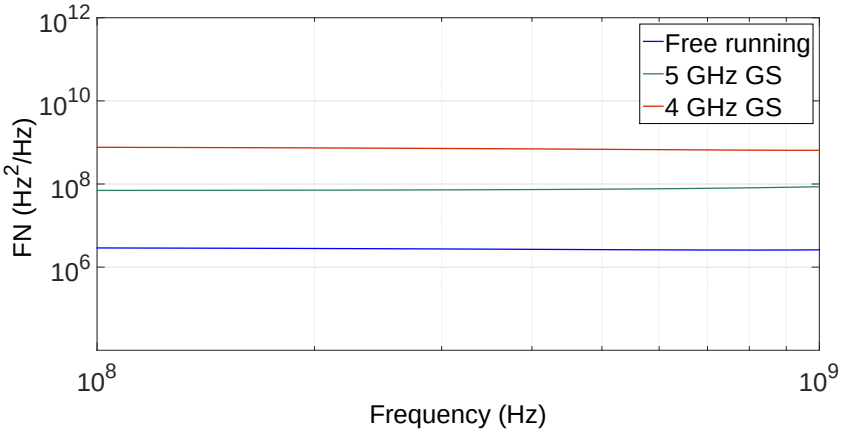

Figure 3.5: FN spectrum for a $500\,\mu\mathrm{m}$ laser with β parameters of 10^{-4}. Free running case is compared to gain-switched case for RF frequencies of $5\,\mathrm{GHz}$ and $4\,\mathrm{GHz}$. An increase in frequency noise is seen for the gain-switched case.

An increase in frequency noise is shown when the laser is gain-switched compared to its free running state. When the laser is gain-switched at frequencies above the resonance frequency, the increase in phase correlation between pulses (as the laser is not switching off fully between cycles) leads to a decrease in the frequency noise [45]. The average value of the low frequency FN spectrum was plotted for increasing values of the gain-switching modulation frequency in Figure 3.6.

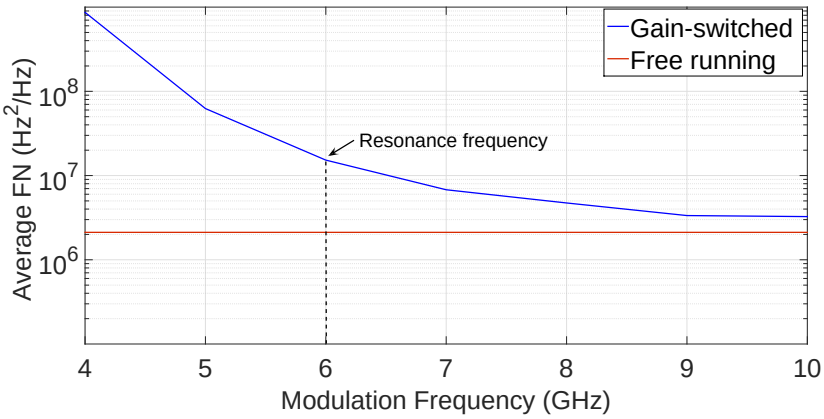

Figure 3.6: Average value of the low frequency (0.1–1 GHz) FN spectrum for increasing values of the gain-switching modulation frequency with $\beta = 10^{-4}$. The average noise decreases as the modulation frequency increases.

As shown in Figure 3.6, the average frequency noise of a gain-switched laser decreases as the modulation frequency increases. As both laser linewidth and resonance frequency increase and decrease with length respectively [94, 96], designing a laser with a high resonance frequency and a low linewidth remains a problem.

3.2 With Injection-Locking

Injection-locking is a technique whereby the optical output of a master laser is injected into a slave laser cavity, typically through an isolator. The optical output of the slave laser is then phase-locked to the master laser, with a number of favourable benefits [50, 52, 56, 58], provided that the master laser has sufficient power and the master laser frequency matches a mode in the slave cavity.

3.2.1 The Injection-Locked Rate Equations

The rate equations for an injection-locked single mode laser are similar to the standard case, but with additional terms in the photon and phase equations to account for the injected optical signal. The equations are as follows,

$$\frac{dN}{dt} = \frac{I(t)}{eV} - R(N) - a(N - N_{tr})S + F_N(t) \tag{3.16}$$

$$\frac{dS}{dt} = \left(\Gamma a(N - N_{tr})S - \frac{1}{\tau_p}\right) S + \beta BN^2 + k_C\sqrt{S(t)S_{ml}(t)cos(\phi_{ml} - \phi)} + F_S(t) \tag{3.17}$$

$$\frac{d\phi}{dt} = \frac{1}{2}\Gamma\alpha_H a(N - N_{tr}) + k_C\sqrt{\frac{S_{ml}(t)}{S(t)}sin(\phi_{ml} - \phi)} - 2\pi\Delta f + F_\theta(t) \tag{3.18}$$

$k_C = \nu_g/2L$ is the coupling rate, which has an inverse relation to the slave laser length. A shorter slave laser will have a higher coupling rate as the injected photons can better distribute along the cavity, i.e. it is easier to injection-lock a shorter slave laser. $S_{ml}(t)$ is the master laser photon density, and ϕ_{ml} is the master laser phase. These can be generated from equations 3.1, 3.2, 3.3, and passed into the injection-locked equations. Δf is the frequency detuning between the master and the slave lasers (set to 0 in this case). All other terms are as before (Table 3.1).

The simulated master and slave lasers both used the parameters from Table 3.1. A lower β parameter was used by the master laser to simulate a lower linewidth, see Table 3.1. A scaling factor of 10 was used to amplify the photon density of the master laser to ensure stable locking was achieved [98]. Thus, the model simulates the case of strong optical injection [53, 99].

The variation in carrier and photon density with time was plotted for the injection-locked slave laser, and is shown in Figure 3.7a. The free running slave laser carrier and photon densities are plotted for comparison.

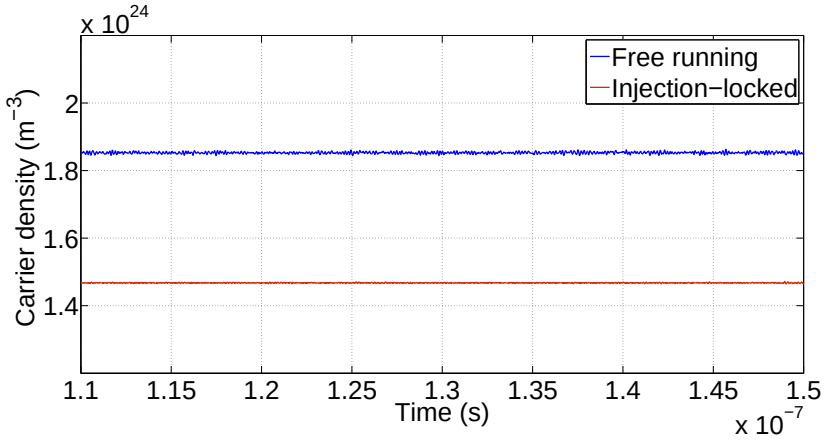

(a)

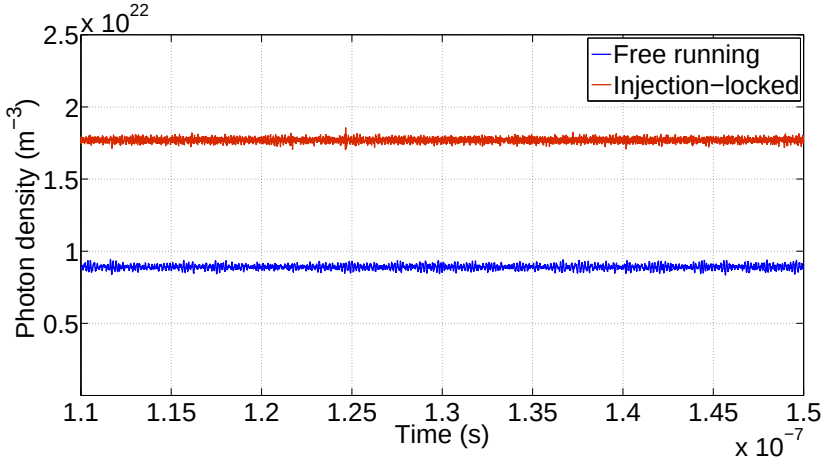

(b)

Figure 3.7: (a) Carrier density vs. time for free running and injection-locked slave laser. Carrier density is shown to decrease when locked. (b) Photon density vs. time. Photon density in the slave laser cavity increases due to the injected optical signal.

The carrier density decreases under injection-locking when compared to the free running case. This makes physical sense as the carrier density clamps when the losses are compensated by the gain, therefore when additional light is injected, less gain is required to reach transparency, and thus the carriers clamp at lower levels under injection. The photon density increases under injection-locking due to the extra contribution of the injected optical signal, provided the pumping remains constant. While the carrier density drops below the threshold density to achieve sustained lasing (see Figure 3.2a), the input of photons from the master laser compensate to maintain the gain equal to the loss threshold condition.

3.2.2 Phase Noise

The impact of injection-locking on phase noise was examined by applying Equations (3.14) and (3.15) to the injection-locked rate equations to obtain the FN spectrum. The FN spectrum of the free running master and slave lasers is compared to the injection-locked slave FN spectrum in Figure 3.8. A smoothing function of 1% was applied to FN spectra.

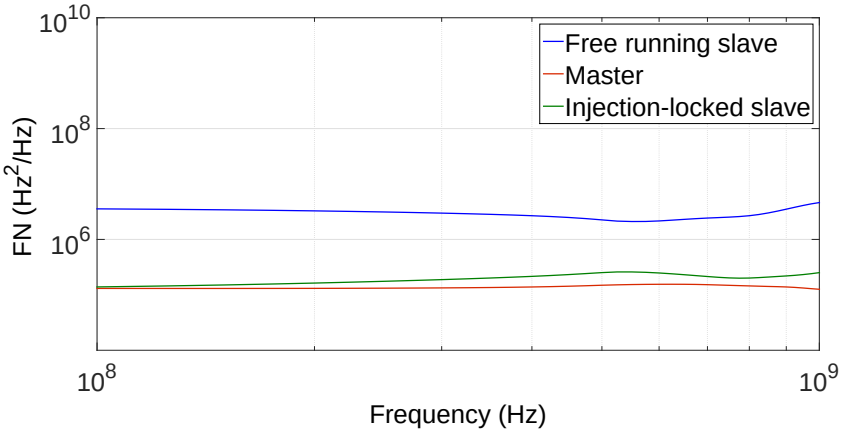

Figure 3.8: FN spectrum for slave laser, $\beta = 10^{-4}$, master laser, $\beta = 10^{-6}$, and the injection-locked slave laser. The low frequency noise of the slave laser decreases towards that of the master when injection-locked.

The model predicts that the injection-locked slave laser will take on the phase noise properties of the master laser. This is a useful property and will be further examined for the case of a gain-switched slave laser in the following section.

3.2.3 Including Gain-Switching with the Injection-Locked Rate Equations

Gain-switching was included in the injection-locked rate equations using the method outlined in section 3.1.3. The FN spectra were calculated and compared for 3 cases; the free running master laser, the gain-switched slave, and the gain-switched injection-locked slave laser. A $4\,\mathrm{GHz}$ signal was used for the gain-switched cases. The spectra are plotted in Figure 3.9.

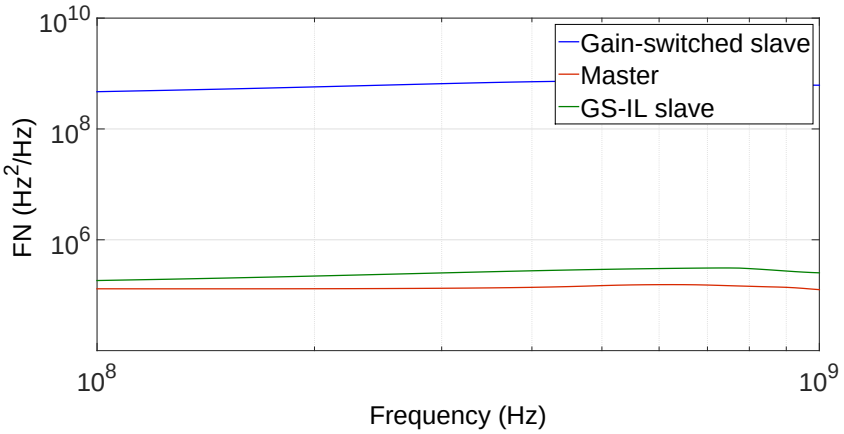

Figure 3.9: FN spectrum for the master laser, gain-switched slave laser, and gain-switched injection-locked (GS-IL) slave laser. The low frequency noise of the GS slave laser decreases towards that of the master when injection-locked. The RF frequency for gain-switching was set at $5\,\mathrm{GHz}$.

While gain-switched, the frequency noise of the slave laser increases above its free running level, as seen in Figure 3.9. When injection-locked, the noise of the slave laser is demonstrated to decrease to the level of the master laser.

The low frequency noise of the injection-locked gain-switched slave laser is a useful property. In Chapter 5, this property shall be investigated with an on-chip master laser, without the use of an isolator [34, 100].

3.3 Conclusion

In this chapter, a theoretical study of single mode lasers has been performed using the semiconductor laser rate equations. Phase noise due to carrier oscillations was the focus, due to its contribution to the laser linewidth. Laser linewidth is a critical characteristic in fibre optic communications, with a low-linewidth desirable for high-bandwidth communications.

From this investigation, it has been shown in Figure 3.5 that a gain-switched single mode laser will experience an increase in phase noise, and thus an increase in linewidth, when the modulation frequency is below the laser's resonance frequency. For the purpose of generating optical combs, a laser with a high resonance frequency, but a low linewidth is required. In order to achieve a low linewidth optical comb source with a tunable comb line spacing, injection-locking was explored.

An analysis of phase noise was performed for the injection-locked rate equations following the same method as for the standard rate equations. It

was shown that by injection-locking the gain-switched slave laser to a low linewidth master laser, the phase noise of the slave laser reduced to that of the master (see Figure 3.9). Thus, injection-locked gain-switched lasers show great promise as optical comb generators for superchannel communications.

The following chapter, Chapter 4, will look at the design and fabrication of real devices to investigate the theoretical findings from this chapter. The photonic integration of two lasers shall be investigated in Chapter 5 for the purpose of comb generation.

Chapter 4

Design, Fabrication, and Initial Characterization of Research Devices

In the previous chapter, injection-locking was theoretically shown to decrease the noise in gain-switched lasers, provided the master laser is itself low-linewidth. The application of the injection-locking technique in real devices is discussed in this chapter, and Chapter 5. This chapter also discusses the design and fabrication of devices.

There are four main steps in the design of a new photonic device; material design/growth, mask design, fabrication, and characterization. This chapter shall focus on basic characterization of devices fabricated for this thesis, as well as lithography mask design and fabrication. Material design was not investigated as part of this thesis, and further device characterization is dealt with in Chapter 5.

All devices fabricated for this thesis were fabricated on commercially available lasing material designed for emission at $1.55\,\mu\mathrm{m}$ with indium phosphide substrates, purchased from the company IQE. The material consists of 5 compressively strained AlGaInAs quantum wells on an n-doped (100) InP substrate, with a total active region thickness of $0.41\,\mu\mathrm{m}$. The upper p-doped cladding consists of a $0.2\,\mu\mathrm{m}$ InGaAs cap layer, followed by $0.05\,\mu\mathrm{m}$ of InGaAsP, lattice matched to $1.62\,\mu\mathrm{m}$ of InP. A detailed layer structure of the material can be found in Appendix A. All devices were designed to operate with a single lateral mode based on single mode waveguide designs. Processes were run on quartered 2-inch wafers to reduce costs.

Several devices were fabricated, both to test if the fabrication process was

successful and that the device characterization setup was fully operational. Device features were also investigated for use in integrated optical comb sources; etched facets, metal coated etched facets [101], and laser slots [102].

4.1 Etched Facets

The use of etched facets was desired for the integration of photonic devices. The performance of these facets was investigated prior to their use, in order to appraise their reflectivity.

4.1.1 Design

A set of Fabry-Pérot lasers were fabricated for investigating the reflectivity of etched facets. The schematic of these devices obtained from the lithography mask file is shown in Figure 4.1a. Each device has a shallow etched ridge of width $2.5\,\mu\mathrm{m}$, and length of approximately $1800\,\mu\mathrm{m}$, $1700\,\mu\mathrm{m}$, and $1700\,\mu\mathrm{m}$ for the devices labelled FP (Fabry-Pérot), EF (etched facet), and MEF1 (metal etched facet) respectively. FP is a cleaved facet Fabry-Pérot laser. EF has one cleaved facet and one etched facet. MEF1 has one cleaved facet and one metal covered etched facet. Figure 4.1b shows a microscope image of the devices.

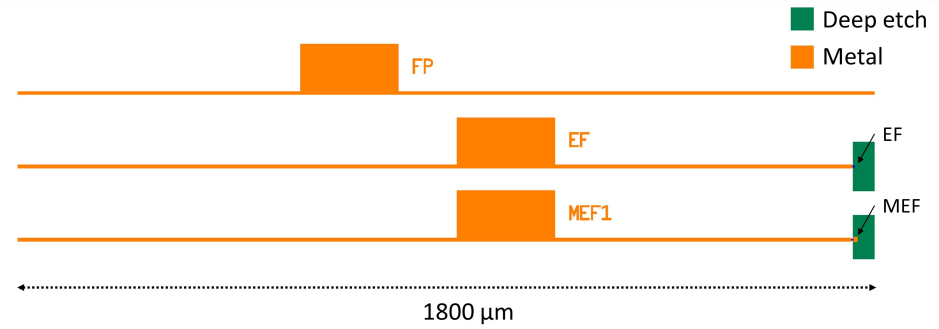

(a)

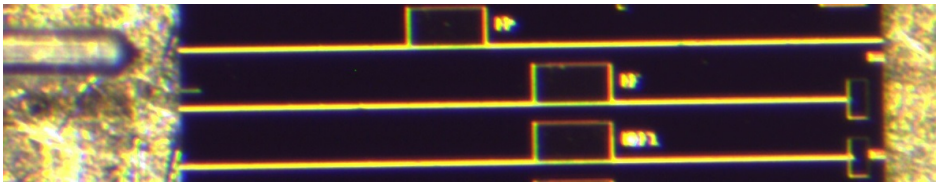

(b)

Figure 4.1: (a) Schematic of Fabry-Pérot lasers. Device FP has two cleaved facets. Devices EF and MEF1 have an etched facet and a metal etched facet respectively, with one cleaved facet each. (b) Microscope image of devices. Lensed optical fibre is visible to the left.

4.1.2 Characterization

The devices were tested on a custom setup built for characterizing PICs. The setup consists of a thermally controlled brass chuck, probe needles for applying bias, and lensed optical fibre for collecting light. A photograph of the test setup with a device under test is shown in Figure 4.2. This was setup was built as part of the work for this thesis.

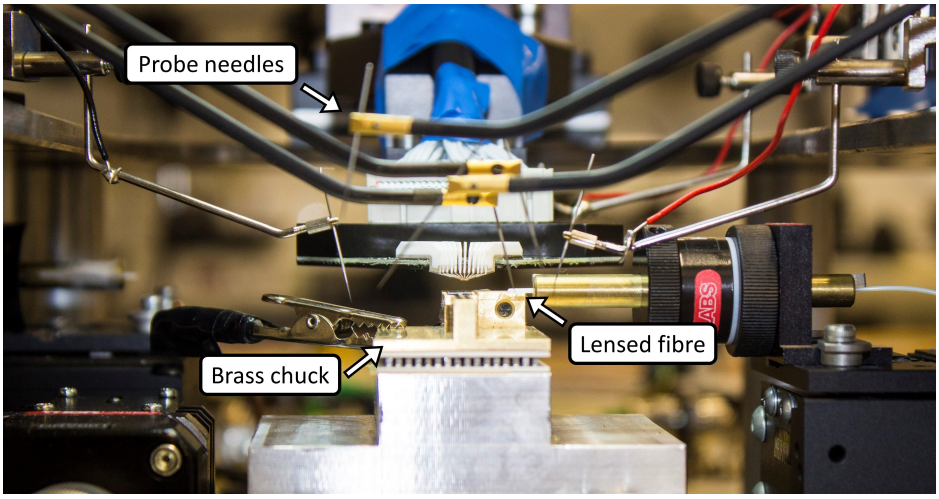

Figure 4.2: Custom test setup built for characterizing PICs. The setup features a thermally controlled brass chuck, probe needles, and lensed optical fibre.

The FP laser chip was mounted on the thermally controlled brass chuck, maintained at $23\,^{\circ}\mathrm{C}$. Voltage and optical power were recorded for an incremental current across the three devices. Current was swept from $0\,\mathrm{mA}$ to $70\,\mathrm{mA}$. Voltage vs. current is shown in Figure 4.3a for the three devices. Device 1 shows a slightly higher resistance than devices 2 and 3, with the devices behaving similar otherwise. This difference could be due to contact issues while probing the device. Optical power vs. current is shown in Figure 4.3b. The threshold current can be determined for the three devices from this plot.

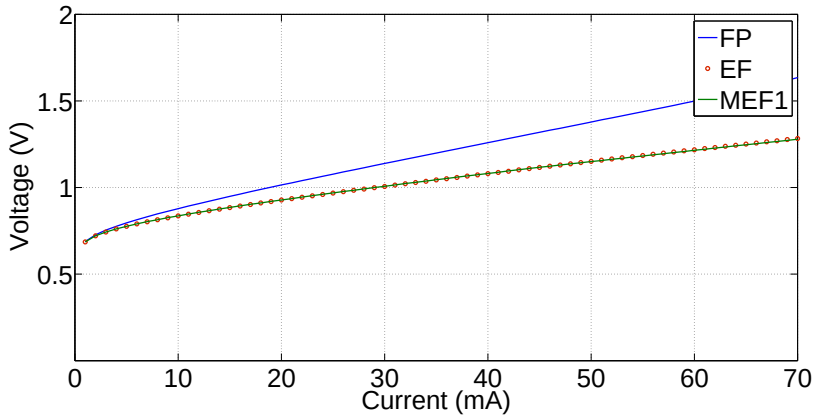

(a)

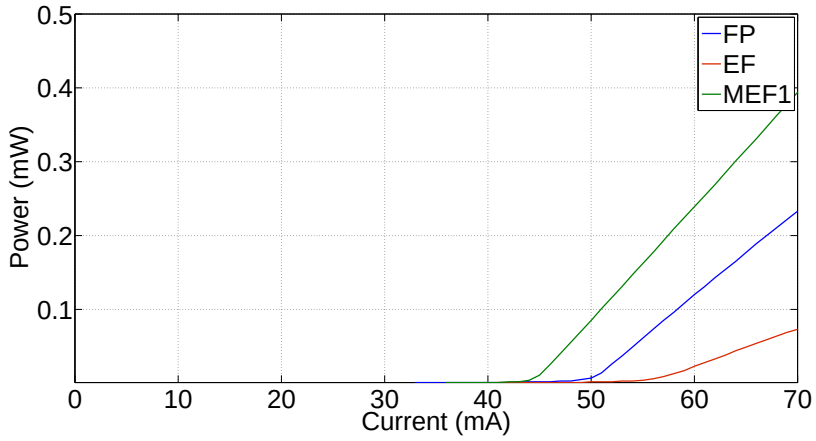

(b)

Figure 4.3: (a) Voltage vs. current (b) Optical power vs. current, for three Fabry-Pérot devices. Device FP has two cleaved facets, device EF has a cleaved facet and an etched facet, and device MEF1 has a cleaved facet and a metal covered etched facet.

A spectrum was recorded just below threshold for the three devices. An example of a typical below threshold spectrum is shown in Figure 4.4 recorded from the FP device at $49\,\mathrm{mA}$. The evenly spaced FP modes determined by the device length are shown, with the gain centred at approximately $1575\,\mathrm{nm}$. Note that for the set of wafers purchased from IQE, the PL wavelength was longer than designed (approximately $1570\,\mathrm{nm}$, as opposed to the desired $1550\,\mathrm{nm}$), resulting in the longer wavelength operation of the devices.

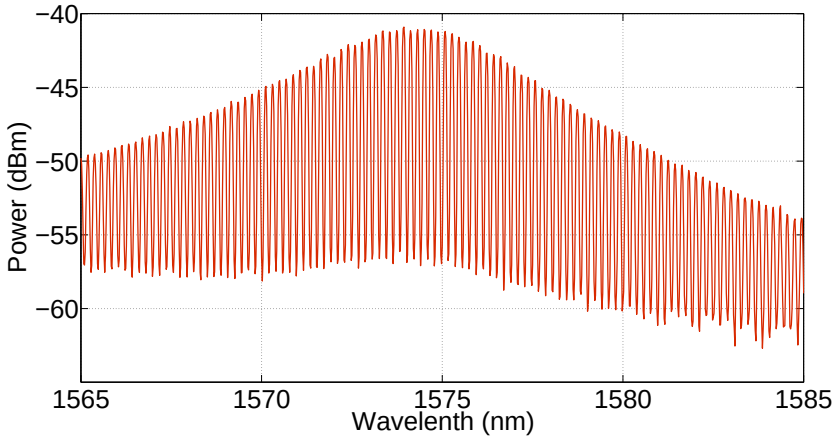

Figure 4.4: Typical optical spectrum for a FP laser just below threshold, $50\,\mathrm{mA}$. Evenly spaced modes are shown with the gain curve centred at approximately $1575\,\mathrm{nm}$.

By applying a Fourier transform to these spectra, the length of the device can be determined. The Fourier transform plot is shown in Figure 4.5.

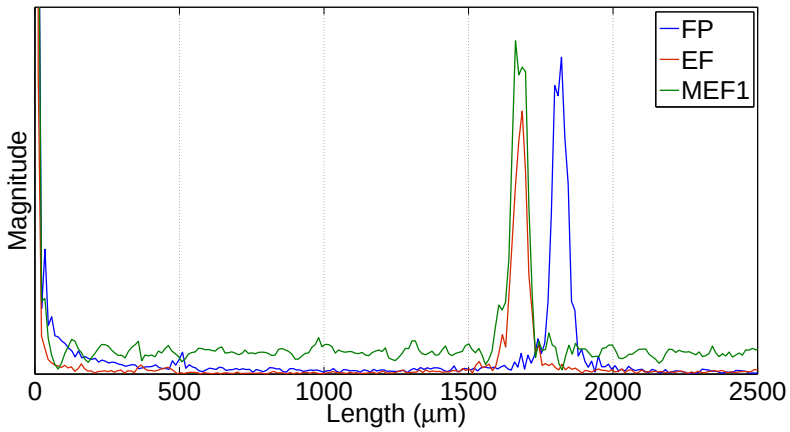

Figure 4.5: Fabricated devices for the purpose of facet reflectivity measurements. From top to bottom, device FP has two cleaved facets, device EF has a cleaved facet and an etched facet, device MEF1 has a cleaved facet and a metal coated etched facet.

The approximate length of the FP cavity was $1820\,\mu\mathrm{m}$, with the EF and MEF1 cavity's measuring $1685\,\mu\mathrm{m}$. While the FP laser is greater in length, the cavities were taken as equal for the purpose of estimating the reflectivity of the etched facets.

The reflectivity of the EF and MEF can be obtained via the following method. The round trip gain for a FP laser is given by [93],

$$g = \frac{1}{2L} \ln\left(\frac{1}{R_1 R_2}\right) \tag{4.1}$$

where g is the gain, L is the cavity length, and R_1 and R_2 are the facet

reflectivities. As gain is proportional to input current (I), the gain of two devices with the same dimensions can be compared at threshold, with the difference in gain accounted for by the difference in mirror reflectivity of the facets.

$$\frac{g_1}{g_2} \propto \frac{I_1}{I_2} = x \tag{4.2}$$

$$g_1 = x g_2 \tag{4.3}$$

Substituting for g,

$$\ln\left(\frac{1}{R_1 R_2}\right) = x \ln\left(\frac{1}{R_1 R_3}\right) \tag{4.4}$$

R_1 is common as both devices have a cleaved facet. Rearranging Equation 4.4 and solving for R_3 gives,

$$R_3 = \sqrt[x]{\frac{R_1 R_2}{R_1^x}} \tag{4.5}$$

Using Equation 4.5, the reflectivity of an EF and an MEF can be estimated from the devices shown in Figure 4.1b. The cleaved facet reflectivity is a known quantity in the equation, and has a typical value of 30%. Applying Equation 4.5, and taking the threshold current for the FP, EF, and MEF lasers as $50\,\mathrm{mA}$, $56\,\mathrm{mA}$, and $45\,\mathrm{mA}$ respectively, the reflectivity of the EF was approximated as ∼22%, and the MEF as ∼38%.

Typically there is a loss associated with a laser cavity, such that the gain is actually proportional to $(I - I_t)$, where I_t the current required for the laser to reach transparency. While it was not possible to measure I_t for this set of devices, R_3 was plotted for a variable I_t to investigate the effect of the transparency current on the reflectivity estimation. The value of x in Equation 4.5 is now given by,

$$x = \frac{I_1 - I_t}{I_2 - I_t} \tag{4.6}$$

The variation of R_3 with I_t is shown in Figure 4.6.

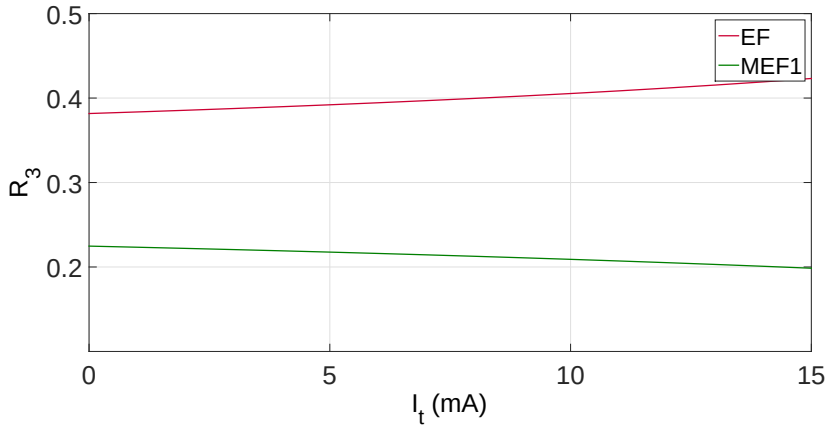

Figure 4.6: R_3 vs. I_t for EF and MEF1. R_3 does not vary significantly with I_t.

From this analysis, the reflectivity of the etched facet and the metal etched facet were overestimated and underestimated respectively. The correlation between R_3 and I_t is weak, indicating that the result provided by Equation 4.5 is sufficient for estimating the reflectivity.

4.2 Slotted Fabry-Pérot Lasers

4.2.1 Design

Specific devices designed for this thesis were based on the Slotted Fabry-Pérot (SFP) laser design reported in references [102–104]. Slotted lasers use periodic slots etched into the ridge to provide reflection. Thus, periodic slots can be used in place of a cleaved facet to provide enough reflection for lasing. The perturbations in the cavity introduced by these slots introduces a wavelength dependence to the optical output and can be used to design a single mode laser, as shown in [104]. The periodic sub-cavities formed by the slots selectively enhance wavelengths which are resonant with the sub-cavities. By varying the periodic spacing between the slots, the accessible modes by the slotted laser can be adjusted. A side view of the slotted design is shown in Figure 4.7.

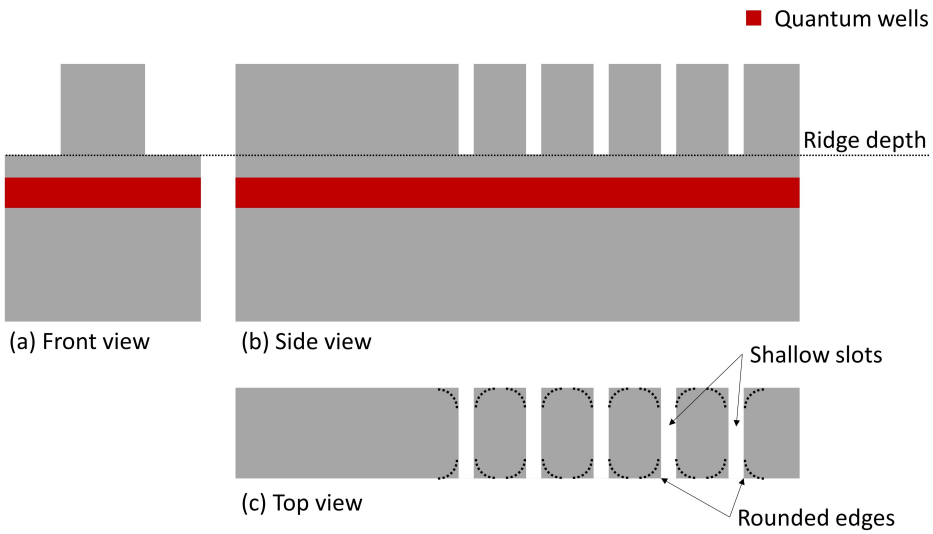

Figure 4.7: Slotted laser structure. (a) A facet view of the device shows the ridge waveguide structure. (b) A side view of slotted laser structure is shown. Slots are periodically etched into the ridge to the same depth as the ridge. Each slot provides a small reflection which compounds with multiple slots to facilitate lasing at the resonant wavelength. (c) A top view of the ridge waveguide. Shallow slots are indicated, with potential rounding of slot edges shown with dashed black lines.

Square features, such as the top corners of the slotted laser design in Figure 4.7, are at risk of becoming rounded during the fabrication process. Rounding of edges can degrade the wave guiding performance of the ridge, and potentially reduce the reflectivity of the slot. As these slots are critical features of an SFP laser, steps were taken to mitigate this issue.

A T-bar structure, as seen in Figure 4.8a, was used to move rounded edges away from the center of the waveguide. As the waveguide only widens for a distance of $1\,\mu\mathrm{m}$, there is little impact on the confined mode. These T-bars were used any time a slot or etched facet was required.

Angled slots were also used in device designs to electrically isolate sections of a waveguide. By angling the T-bar at $7°$ (the Brewster angle) to the vertical, reflections from the slot that would couple back into the waveguide could be reduced [105]. An angled T-bar slot is shown in Figure 4.8b. A combination of angled and straight T-bars could be used if the device required reflection in one direction.

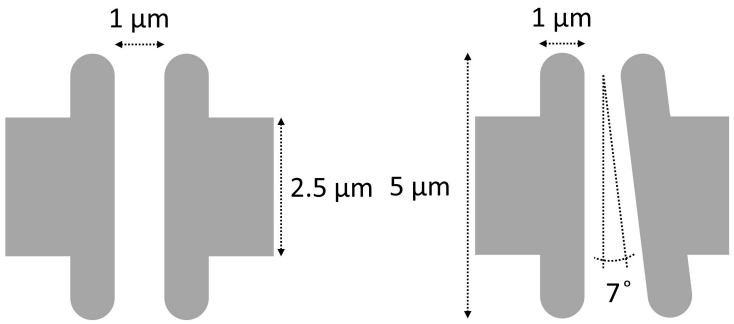

(a) (b)

Figure 4.8: (a) Standard slot used in device designs. T-bar structure removes potential waveguide corner rounding at the slot (b) Angled slot. T-bars are angled at 7° to reduce reflections at the slot. Angled slots can be used to provide electrical isolation between waveguides.

A Scanning Electron Microscope (SEM) image of a slotted feature on a device is shown in Figure 4.9a. An etched facet coated in metal is shown to the left of the slot, with both the etched facet and the slot using T-bars. A top down microscope view of angled T-bar slots used to electrically isolate sections of a waveguide is shown in Figure 4.9b.

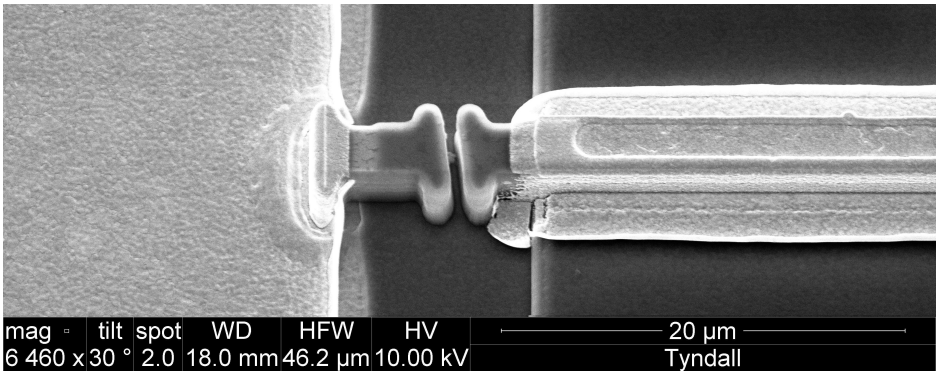

(a)

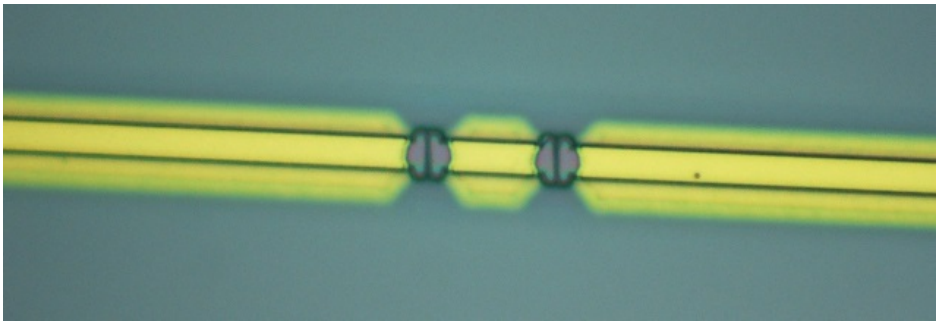

(b)

Figure 4.9: (a) SEM of slot features. A metal coated etched facet is visible on the left, with a deep etched angled slot electrically isolating the facet from the waveguide. (b) Top down microscope view of shallow etched angled slots providing electrical isolation along a waveguide.

An SFP laser schematic is shown in Figure 4.10a. This device has a shallow etched ridge of width $2.5\,\mu\mathrm{m}$, and total length $1350\,\mu\mathrm{m}$. The slotted section features 7 equally spaced slots with a slot spacing of $114\,\mu\mathrm{m}$, connected to a straight $550\,\mu\mathrm{m}$ gain section. The slot width is $1\,\mu\mathrm{m}$. The slot spacing corresponds to a supermode spacing of approximately $380\,\mathrm{GHz}$, similar to the design outlined in [102]. A deep etch was used to define both the metal covered etched facet (MEF) and a top level N-contact. A microscope image of the device is shown in Figure 4.10b. This device was used to investigate the operation of SFP lasers, and also to study gain-switching of a single mode laser.

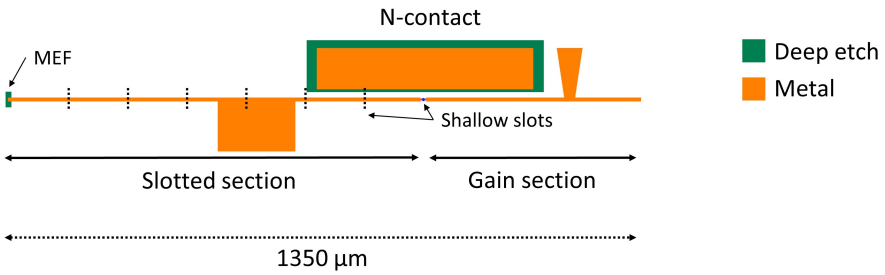

(a)

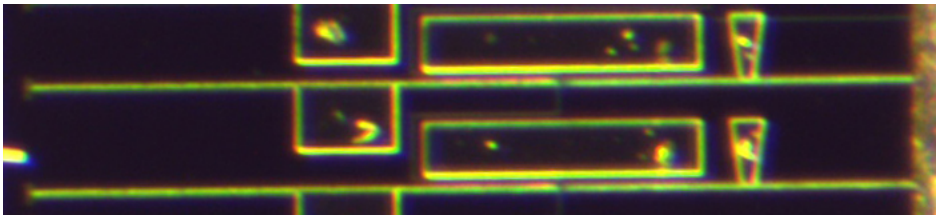

(b)

Figure 4.10: (a) SFP laser schematic with sections labelled. Black dotted lines indicate the positions of the shallow etched slots. A metal covered etched facet (MEF) was placed after the slotted section to improve reflectivity. (b) Microscope image of SFP device with duplicate visible.

4.2.2 Characterization

A basic characterization experiment was performed on the 2-section SFP laser shown in Figure 4.10b. The device was mounted on a thermally controlled brass chuck, maintained at $23\,^{\circ}\mathrm{C}$. The chuck was grounded to act as a negative contact for the backside n-metal of the device. Electrical bias was applied to both sections of the device via probe needles, and swept from $0 - 80\,\mathrm{mA}$. A lensed fibre was coupled to the cleaved facet of the device to measure optical power. Figure 4.11 shows a microscope image of the device under test.

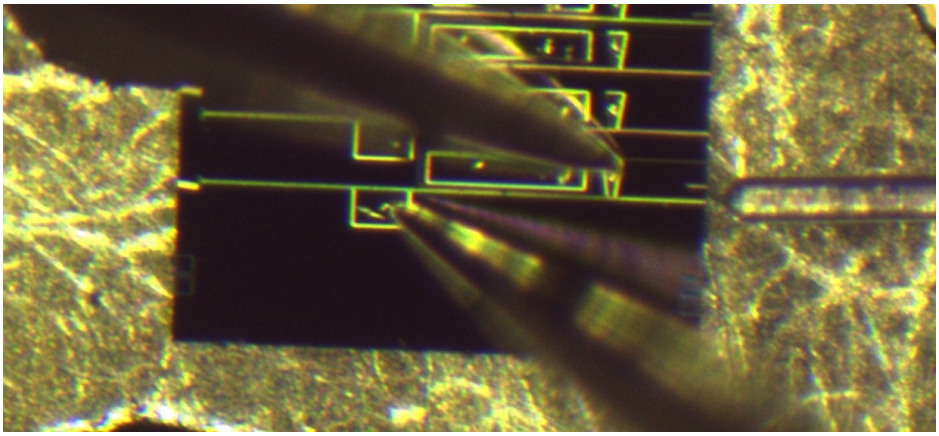

Figure 4.11: SFP test setup. Device was mounted on a brass chuck. Probe needles are shown making contact with each section of the device. To the right of the device, lensed fibre is shown coupling to the facet of the laser.

Voltage and optical power were recorded. The data is represented on a Light-Current-Voltage (LIV) plot in Figure 4.12.

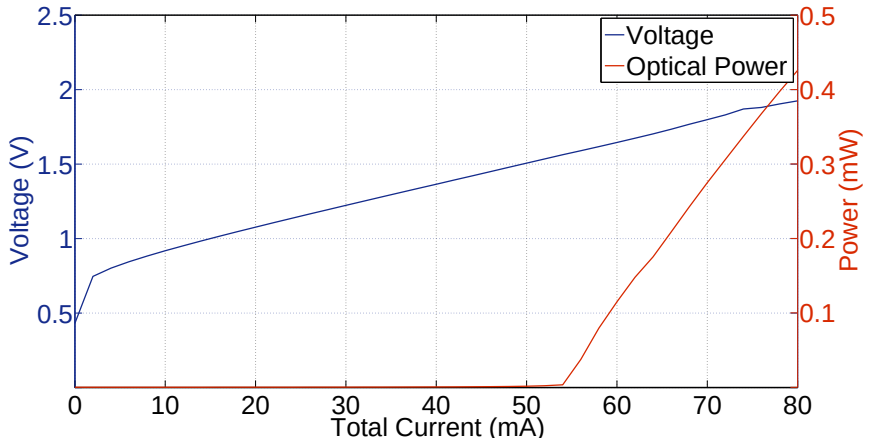

Figure 4.12: LIV plot for 2-section SFP laser shown in Figure 5.9b. Linear increase in optical power at $\sim 55\,\mathrm{mA}$ indicate lasing from the device.

The characteristic kick in optical power at $\sim 55\,\mathrm{mA}$ confirms lasing of the device.

Next, performance as a single mode laser was investigated. By varying the bias in each section of the SFP, multiple wavelengths are obtainable, as demonstrated previously [102, 103]. An automated characterization experiment was performed on the device to determine the tunability. Using programmable current sources, a bias was applied to each section and swept over a certain range. In this case, the range was 20-$70\,\mathrm{mA}$ on each section in steps of $2.5\,\mathrm{mA}$. An optical spectrum was recorded for each bias configuration. The peak wavelength (wavelength with the highest optical power) and the

SMSR was extracted from each spectrum. By plotting this data in the form of a color map, single mode configurations for certain wavelengths can be determined. A diagram of the experimental setup is shown in Figure 4.13.

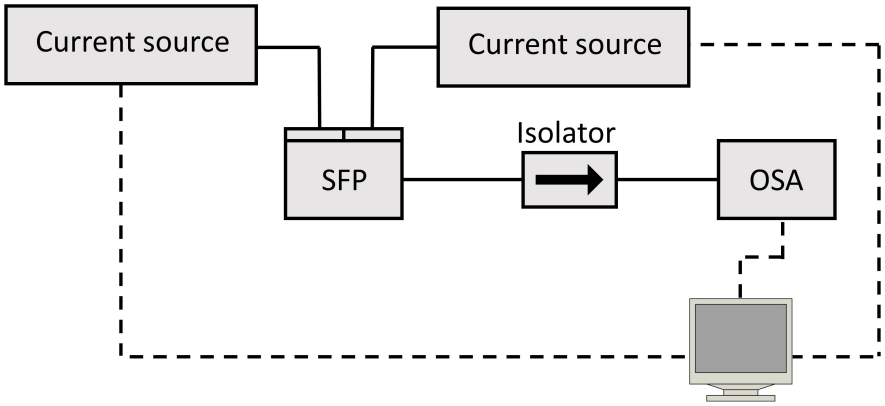

Figure 4.13: Separate current controllers were used to sweep the bias on each section of the SFP laser. An optical spectrum was recorded with an OSA. LabVIEW was used to control the equipment to automate the data collection.

A color map of the peak wavelength for each current configuration is shown in Figure 4.14a, while the color map showing the side mode suppression ratio (SMSR) is shown in Figure 4.14b. The resolution of these plots could be increased by reducing the bias step size, although this leads to a significant increase in the amount of time needed to record the data.

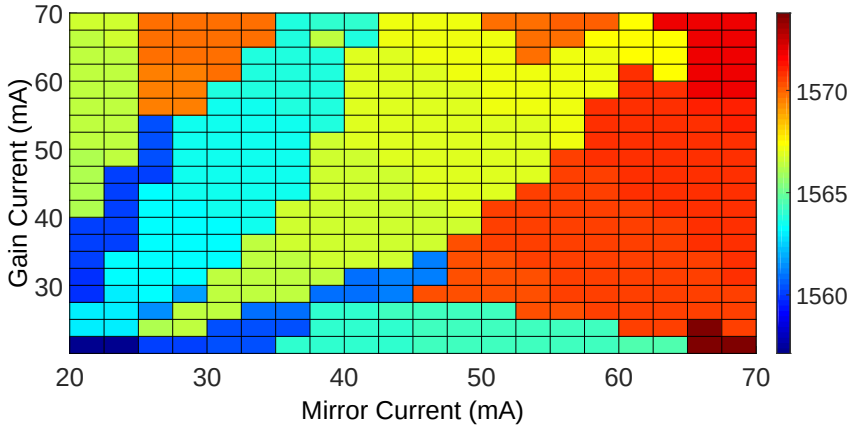

(a)

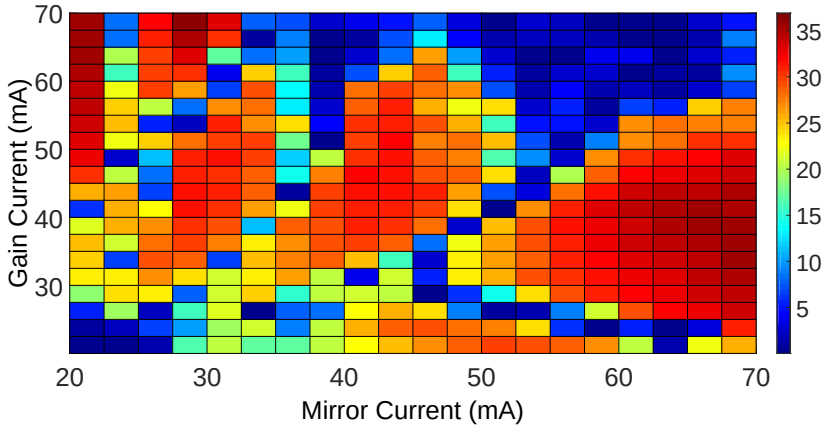

(b)

Figure 4.14: (a) Color plot showing peak wavelength emitted by the SFP for different current configurations. (b) Side mode suppression ratio for the same current configurations. Using these two plots, regions can be identified with a high SMSR at a particular wavelength. Mirror current refers to the current provided to the slotted section.

From the above figures, peak wavelengths with high SMSR can be selected by choosing the correct bias for each section of the SFP. Five wavelengths were identified and plotted in Figure 4.15.

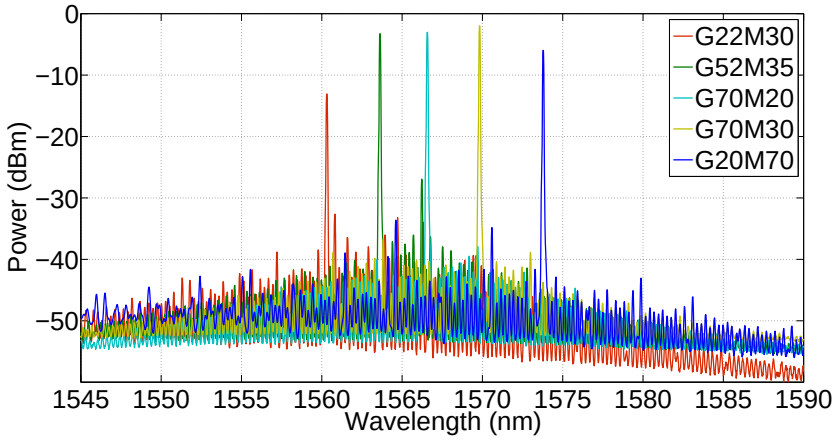

Figure 4.15: Five regions of single mode behaviour achievable from the SFP laser with a minimum SMSR of $20\,\mathrm{dB}$. The legend shows the bias in mA required in each section of the device to obtain each wavelength, where "G" is the gain section and "M" is the mirror section. Mirror current refers to the current provided to the slotted section

The power differential between modes could be reduced with the addition of a semiconductor optical amplifier (SOA) section. The spectral separation between each mode is approximately $3.2\,\mathrm{nm}$, which closely corresponds to the $400\,\mathrm{GHz}$ supermode spacing imposed by the slot period. From the experimental analysis of this device, the SFP lasers show good potential for use as the single mode lasers required for gain-switched optical comb sources. In Chapter 5 the performance of this device as a gain-switched optical comb source will be analysed.

4.3 External Injection-Locking

Injection-locking was first investigated using discrete components, by locking a fabricated Fabry-Pérot diode laser to a commercial tunable laser source (TLS): an Ando AQ4321D, with a stated linewidth of $< 100\,\mathrm{kHz}$. The TLS was used as the master laser, with the diode laser the slave. The master laser wavelength was selected to correspond with a mode supported by the slave laser. This is called external injection-locking. The diode had a shallow etched ridge of width $2.5\,\mu\mathrm{m}$, and length $3.2\,\mathrm{mm}$. Three duplicates of the diode laser are shown in Figure 4.16. These devices were fabricated using the standard ridge laser fabrication process which will be outlined in Section 4.6.1.

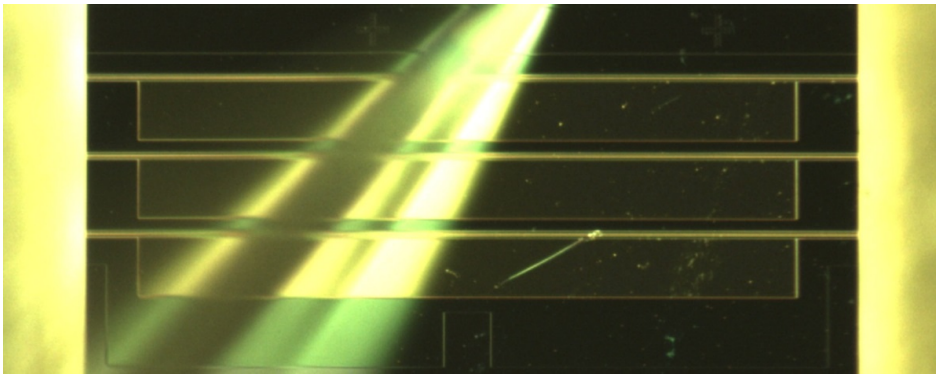

Figure 4.16: Fabricated chip showing three $3.2\,\mathrm{mm}$ Fabry-Pérot ridge lasers with ridge width $2.5\,\mu\mathrm{m}$.

The experimental setup is shown in Figure 4.17, where the DUT is the device under test, and OSA is the optical spectrum analyser. The circulator isolates the TLS from the DUT, and allows the DUT output to be analysed from the same facet as light is injected, simplifying the experimental setup. The circulator provides $30\,\mathrm{dB}$ of isolation. Light was coupled to and from the DUT using a lensed optical fibre. A polarization controller was used to adjust the polarization of the TLS to match that of the DUT. The DUT was mounted on a thermally controlled brass chuck, and maintained at $23\,^{\circ}\mathrm{C}$.

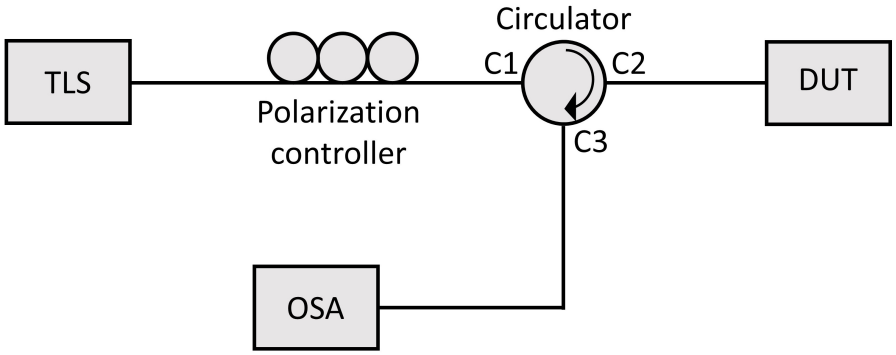

Figure 4.17: Experimental setup. TLS: tunable laser source, DUT: device under test, OSA: optical spectrum analyser. Lensed optical fibre was used to couple to the DUT. The circulator isolates components by only allowing light from C1 to C2, and C2 to C3.

An optical spectrum was first recorded from the DUT with the TLS off. The DUT was biased at $106\,\mathrm{mA}$. The free running spectrum recorded by the OSA is shown in Figure 4.18.

The TLS was switched on to demonstrate external injection-locking. The gross optical power of the TLS, not accounting for losses through components or coupling, was $6\,\mathrm{dBm}$, and the wavelength was set to $\sim 1565.69\,\mathrm{nm}$. Fine

adjustments to wavelength and polarization were required to achieve stable locking. The DUT bias was maintained at $106\,\mathrm{mA}$, and the locked DUT spectrum is shown in Figure 4.18.

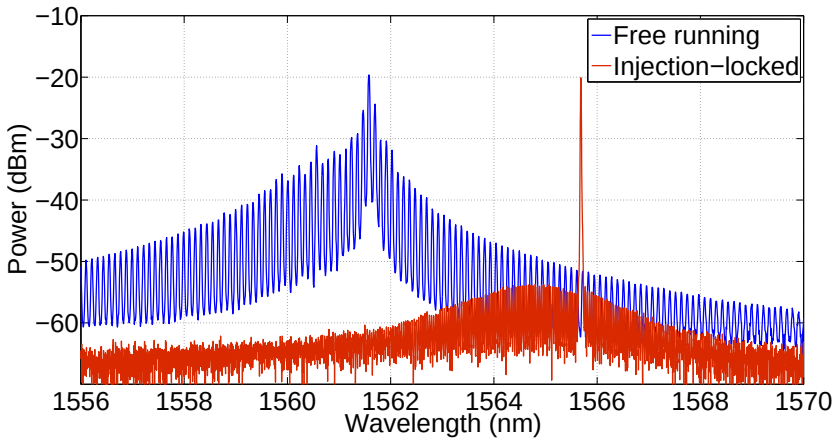

Figure 4.18: Free running and injection-locked spectra for Fabry-Pérot laser biased at $106\,\mathrm{mA}$.

Under injection-locking, all modes in the DUT aside from the locked mode show a dramatic decrease in power, with the spectrum now operating in a single longitudinal mode as the master laser seeds a supported mode in the cavity. The noise floor of the DUT spectrum also decreases under injection-locking; another property of injection-locking due to the low noise master laser [54].

The multimodes of the DUT can be tuned by adjusting the bias. By sweeping the bias, while keeping the TLS constant, it is possible to observe the DUT move in and out of locking to the master. This occurs due to the locking-region that exists, which is dependent on the power of the master laser, and the detuning between the master and slave laser wavelengths [53]. Figure 4.19 demonstrates the locking region effect for a changing DUT bias.

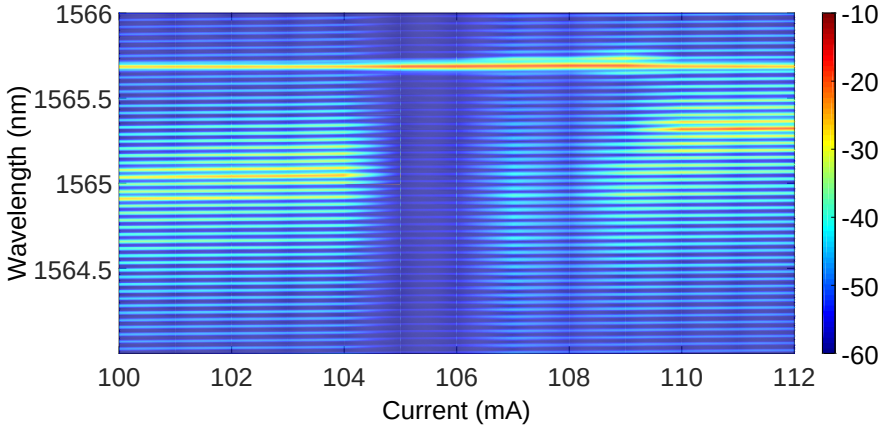

Figure 4.19: Color plot showing the DUT moving in and out of locking as modes are tuned via bias. Increasing optical power is represented by the color changing from blue to red. The DUT is injection-locked for bias of $104\,\mathrm{mA}$ to $108\,\mathrm{mA}$. The bias had a step size of $0.1\,\mathrm{mA}$.

The DUT was locked with an applied bias ranging from $104\,\mathrm{mA}$ to $108\,\mathrm{mA}$, as shown by the decrease in optical power in all other modes of the device. The TLS signal is shown as a constant running through the color plot just below $1566\,\mathrm{nm}$.

With this experiment, external injection using discrete components has been demonstrated. In the following section, on-chip injection-locking is investigated for a monolithically integrated photonic circuit.

4.4 On-Chip Injection-Locking

With injection-locking demonstrated using an external master laser, the case of on-chip injection-locking was next investigated. On-chip injection-locking is a critical requirement for an integrated low linewidth optical comb source based on gain-switched lasers, as demonstrated in Chapter 3. In this section, on-chip injection-locking is demonstrated experimentally for a single device. The technique will be revisited as required in later device characterization sections.

4.4.1 Integrated SFP-FP Device

An FP laser was integrated with an SFP laser to investigate injection-locking and gain-switching [100], see Figure 4.20a. The SFP laser had a total length of $1490\,\mu\mathrm{m}$. The slotted section featured 7 equally spaced slots with a slot spacing of $114\,\mu\mathrm{m}$, with a $690\,\mu\mathrm{m}$ gain section. The FP laser was $400\,\mu\mathrm{m}$ long and was coupled to the SFP via a deeply etched facet. The ridge was formed by a shallow

etch, with a width of $2.5\,\mu\mathrm{m}$. A deep etch was used to define both the metal covered etched facet (MEF) and a top level N-contact. A microscope image is shown in Figure 4.20b

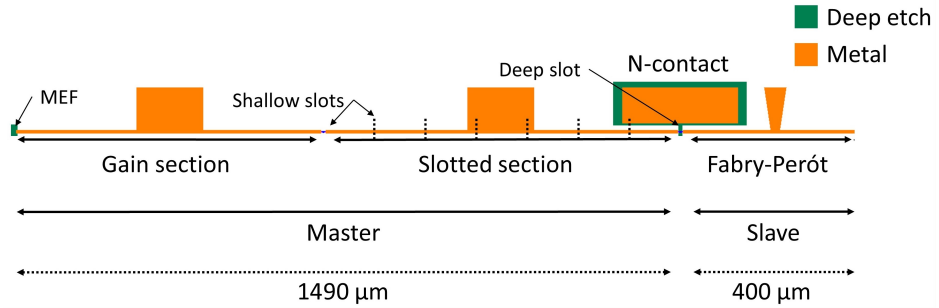

(a)

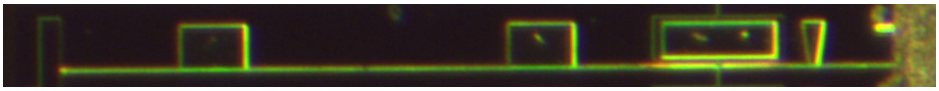

(b)

Figure 4.20: (a) SFP laser integrated with FP laser via an etched facet in a master/slave configuration. Shallow etched slots are labelled and indicated by the dotted black lines. The deep etched slot which forms the etched facet is also labelled. (b) Microscope image of fabricated SFP-FP device.

4.4.2 Injection-Locking

The device was mounted on a thermally controlled chuck maintained at $23\,^{\circ}\mathrm{C}$. A lensed optical fibre was used to couple light out of the cleaved facet of the device for spectral analysis. A probe needle was used to apply bias to each individual section.

An LI curve was obtained from the integrated Fabry-Pérot laser to determine the threshold current of the device. Current was swept from 0 - $40\,\mathrm{mA}$ and optical power was recorded. The resulting plot of optical power vs. current is shown in Figure 4.21a. The threshold current was measured as $\sim 24\,\mathrm{mA}$. The slotted laser was switched off throughout this measurement.

To demonstrate on-chip injection-locking, the Fabry-Pérot laser was biased at $35\,\mathrm{mA}$ with the slotted laser switched off. The optical spectrum was recorded on an OSA. The slotted laser was then switched on by applying $70\,\mathrm{mA}$ to the gain section and $90\,\mathrm{mA}$ to the slotted section. An optical spectrum was recorded. Both spectra are shown overlapped in Figure 4.21b. Suppression of the Fabry-Pérot modes is shown, with the lasing mode showing an SMSR of $\sim 34\,\mathrm{dB}$. Thus on-chip injection-locking has been successfully

demonstrated between the SFP and FP laser.

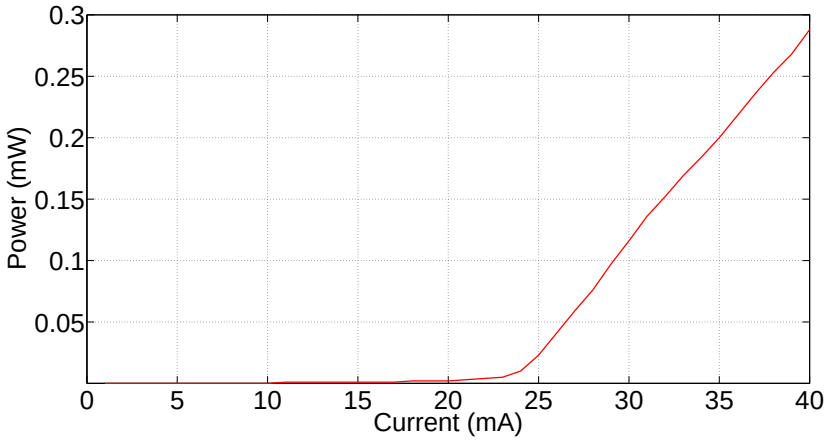

(a)

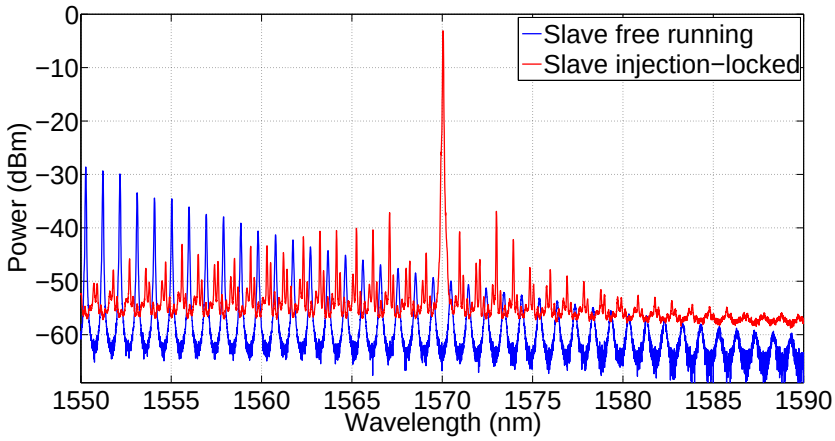

(b)

Figure 4.21: (a) LI plot for a $400\,\mu\mathrm{m}$ Fabry-Pérot laser featuring one etched facet and one cleaved facet. (b) Optical spectrum of free running Fabry-Pérot laser with overlapped injection-locked spectrum. The FP laser is referred to as the slave laser, the slotted laser is the master.

Basic Characterization Summary

With basic characterization experiments outlined above, further device characterization will be dealt with in Chapter 5, where on-chip injection-locking is used extensively. The following sections will deal with the lithography mask design and fabrication of devices.

4.5 Mask Design

Photo-lithography is the process whereby a pattern from a photo-mask is imprinted on to a resist coating a substrate using light. This resist is light sensitive, meaning the exposed/unexposed part of the resist can be removed using a chemical treatment. In this way, lithography can be used to define device features during the device fabrication process. More information on photo-lithography can be found by following references [106, 107].

Each lithography stage of the process requires a lithographic mask. A typical laser process can have three to four lithography steps, thus requiring four lithographic masks. In the process used to fabricate the majority of devices in this thesis, there are four lithography steps: (a) a ridge mask, which defines waveguides/features whose depth is above the quantum wells, (b) a deep mask, which defines waveguides/features whose depth penetrates the quantum wells, (c) an oxide opening mask, which defines openings in the silicon dioxide passivation layer for making contact, and (d) a metal mask, which defines the shape of the metal contacts on the devices. In comparison, a high-speed laser process can have six or more lithography steps, substantially increasing the complexity of the fabrication process. As quarter wafer processes were run, four lithography levels can be defined on a single mask plate, further reducing processing costs. A four level quarter wafer mask design is shown in Figure 4.22a, with a full mask layout showing all layers aligned in Figure 4.22b.

Lithography mask design can be complex, sometimes requiring frequent changes to device parameters. An in-house mask design software was used to design the lithography masks required for this thesis. This software was built within the Integrate Photonics Group and is titled PICDraw [108].

4.5.1 PICDraw

PICDraw is a code based mask layout design software where optical components are drawn by coding commands. An advantage of this software is that device parameters such as length, width, and distances between waveguides, can be defined mathematically such that, if a change is made to one parameter, other parameters can adjust accordingly. Thus, if devices are drawn with care, device scaling and last minute changes to critical device parameters are straightforward. This software was used to design the devices as part of the work for this thesis.

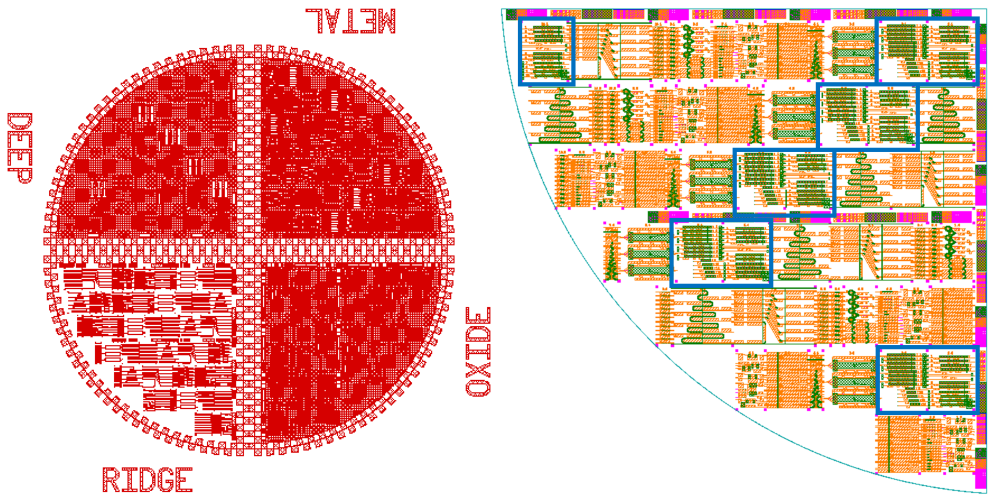

(a) (b)

Figure 4.22: (a) Quad mask output from PICDraw software. Four mask levels printed on a single mask plate for use with a quarter wafer process. Each quarter has a height and width of 1 inches [FHP Comment: the quarter is not 2 inches in size!]. (b) Full mask layout with four layers, ridge, deep, oxide, and metal, overlapped showing the full device layout. Devices designed as part of the work for this thesis have a blue border.

4.6 Fabrication

In this section, the basic steps for the fabrication of ridge waveguide lasers is outlined in Section 4.6.1. A self-aligned deep and shallow etch process is outlined in 4.6.2, where a deep etch involves etching through the quantum wells of the material, with a shallow etch stopping above. This process was designed to accommodate etched facet integration.

Standard UV lithographic techniques were used to define the ridge waveguides and other features such as slots, with a typical ridge width of $2.5\,\mu\mathrm{m}$, ridge height $1.79\,\mu\mathrm{m}$ (shallow etch), deep etch depth $3\,\mu\mathrm{m}$, and a slot width of $1\,\mu\mathrm{m}$, with the ridge etch stopping above the quantum wells. All features were etched with an Inductively Coupled Plasma (ICP) etcher with etch chemistry $Cl_2/CH_4/H_2$ (Ratio 10:8:4).

An overview of the basic process steps involved in the fabrication of a ridge laser using a standard process is outlined below. Devices were fabricated as part of a multi-project fabrication run. Device fabrication was not part of the work for this thesis.

4.6.1 Ridge Laser Fabrication

The main process steps in the fabrication of a ridge laser shall be outlined in this section with diagrams to illustrate each step (see Figures 4.23a, 4.23b). The ridge can be formed with either a deep etch, which etches through the quantum wells, or a shallow etch, which stops above the quantum wells. A shallow etch ridge laser is outlined here:

1. Ridge etch: The ridge was formed by etching the material. Photo-lithography was used to define the ridge on a hard mask of silicon dioxide. The hard mask protected the ridge during the etching process. See Figure 4.23a.

2. Oxide passivation: Silicon dioxide was deposited over and around the ridge, acting as electrical insulation. See Figure 4.23a.

3. Oxide window opening: A window in the oxide layer was opened along the ridge. This allows electric current to pass directly through the ridge. See Figure 4.23b.

4. Metal deposition: Metal, typically a thin layer of titanium followed by gold, was deposited over the ridge. The titanium improves adhesion. A metal contact pad was deposited simultaneously. See Figure 4.23b.

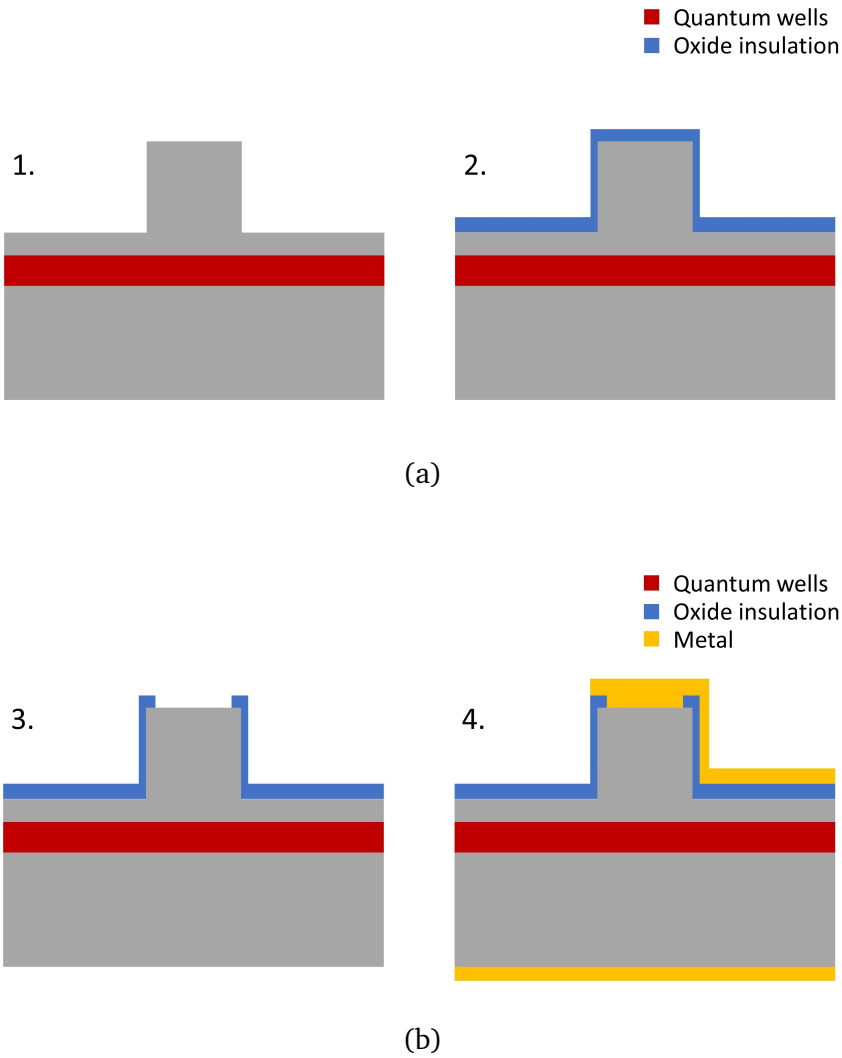

Figure 4.23: (a) Steps 1 and 2 of ridge laser fabrication illustrating the ridge etch in step 1, and silicon dioxide passivation in step 2. (b) Steps 3 and 4 illustrating the oxide window opening in step 3, and metal deposition in step 4.

A SEM image of a ridge laser post fabrication is shown in Figure 4.24. Metal is shown running up and over the ridge. Silicon dioxide is shown as the thin dark gray layer underneath the metal, with a window open on top of the ridge. The quantum wells can be faintly seen as a light gray layer slightly below where the ridge depth stops.

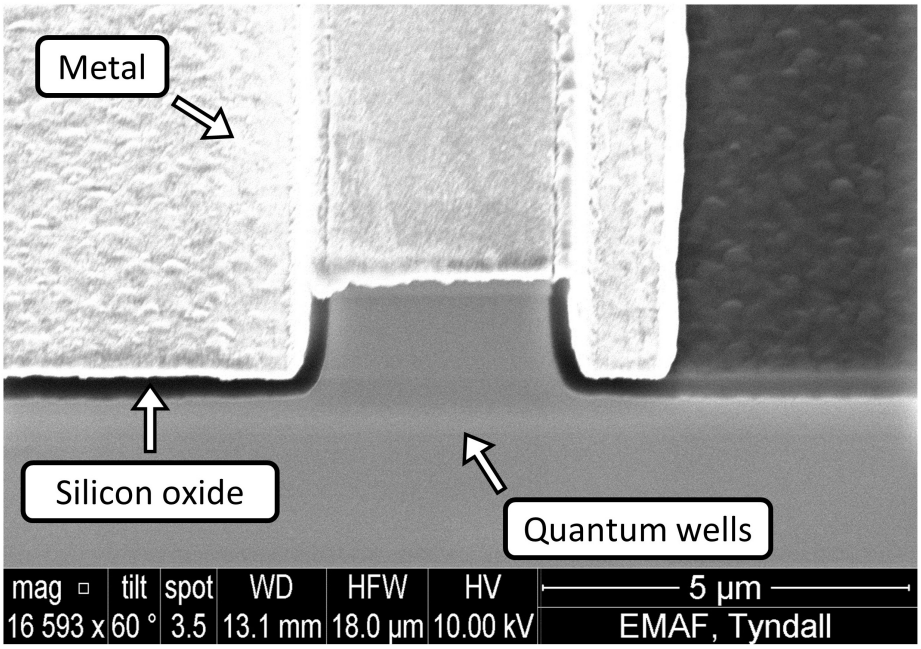

Figure 4.24: Ridge waveguide SEM. Bright gray represents metal running up and over the ridge, making contact with the ridge through a window in thin oxide layer in dark gray. Quantum wells are shown below the ridge depth in light gray.

4.6.2 Self-Aligned Deep and Shallow Etch Process

A self-aligned process was designed to simultaneously etch deep and shallow waveguides [100, 109–111]. The process used two hardmasks during the ridge etch, a silicon dioxide hardmask and a silicon nitride hardmask. Only the oxide hardmask lithography step in this process is critical in both alignment axis, making this a robust process for forming deep and shallow waveguides. The silicon dioxide hardmask defines the ridges, with a broad area silicon nitride protecting areas which are to remain shallow etched. In this way deep and shallow etch ridges can be perfectly aligned with each other. The pertinent steps are outlined below, with illustrations found in Figures 4.25a and 4.25b.

1. The oxide was deposited on the chip and lithographically shaped to protect the areas from the deep and shallow etches. The nitride was deposited on top of the oxide, and lithographically shaped to protect shallow etch areas from the deep etch. The nitride hardmask lithography had a higher error tolerance than the oxide hardmask. A selective nitride etch was used to remove the nitride without harming the oxide. See Figure 4.25a.

2. The first etch was performed, with a target etch depth of $1.3\mu\mathrm{m}$. See

Figure 4.25a.

3. The nitride hardmask was removed using a selective etch, leaving the oxide hardmask for the next etch step. See Figure 4.25b.

4. The second etch step was performed, with a target etch depth of $1.79\,\mu\mathrm{m}$. This gave a total deep etch waveguide depth of $> 3\,\mu\mathrm{m}$, with the shallow etch waveguide stopping at a depth of $1.79\,\mu\mathrm{m}$. See Figure 4.25b.

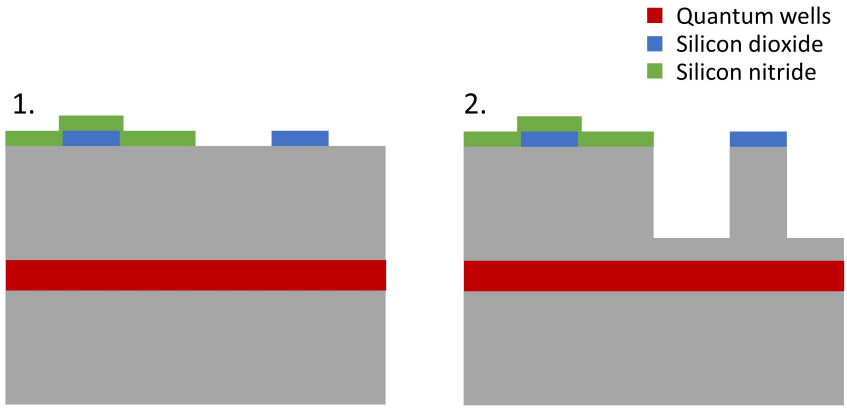

(a)

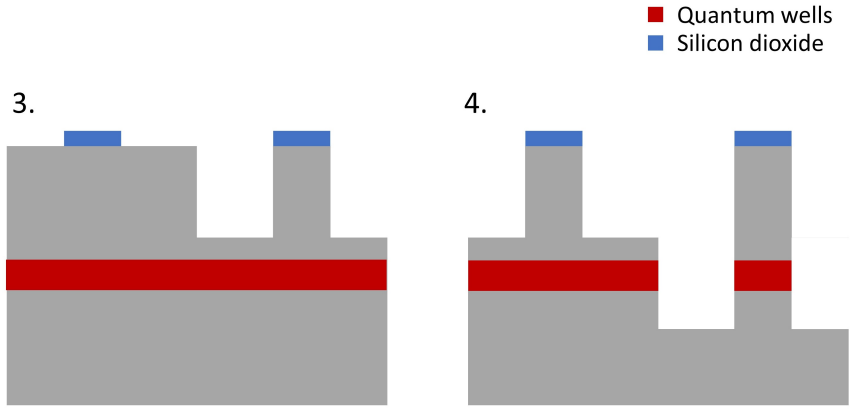

(b)

Figure 4.25: (a) Steps 1 and 2 of the self-aligned deep and shallow etch process illustrating the oxide and nitride hardmask shaping in step 1, and the first etch in step 2. (b) Steps 3 and 4 illustrating the nitride hardmask removal in step 3, and the second etch in step 4.

A SEM image of the self-aligned process after the shallow and deep etches is shown in Figure 4.26. Shallow etch ridge waveguides are shown with slotted

features. The deep etch was used to create etched facets and to define windows or top level n-contacts.

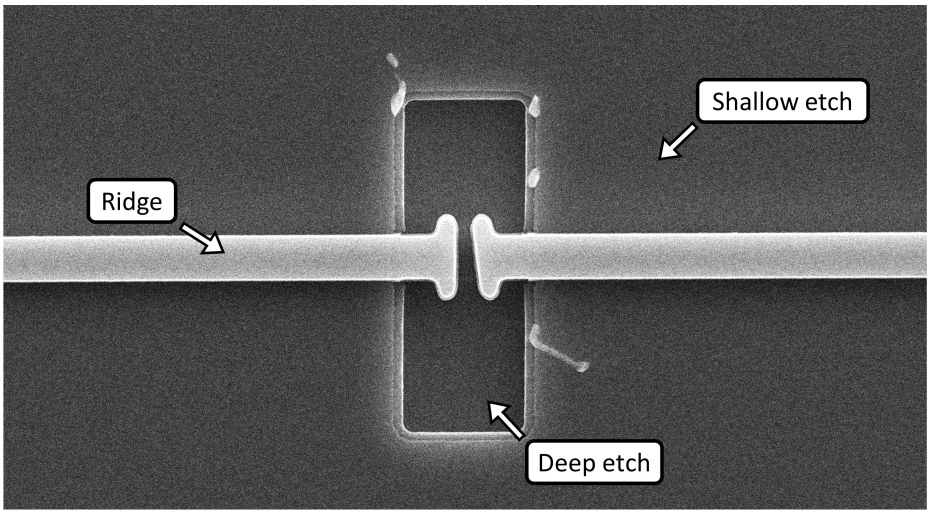

Figure 4.26: SEM image of chip mid self-aligned process. Shallow and deep etches have been performed. A shallow etch ridge waveguide with a slotted feature is shown running horizontally. A deep etch window is shown which was used to form an etched facet. An angled T-bar is shown on right, used to collect light from the etched facet.

4.6.3 High-Speed Process

The high-speed performance of a semiconductor device can be severely limited by the capacitance of the device. The metal pads used as electrical contacts for the device form a parallel plate capacitor with the n-doped substrate. The capacitance in combination with the resistance of the device, impose a limit known as the RC limit. The RC frequency limit is given by Equation 4.7.

$$f_{RC} = \frac{1}{2\pi RC} \tag{4.7}$$

As the dielectric constant of indium phosphide is 12.35 [112], the capacitance is high enough to limit the modulation performance to less than $10\,\mathrm{GHz}$. By etching away the material beneath the contact pads and planarising with a low dielectric constant polymer, the capacitance, and thus the effect of the RC limit, can be greatly reduced.

Benzocyclobutene (BCB) has a dielectric constant 2.65 [113], and can be used to planarise devices to reduce capacitance. Using BCB, the RC limit can be increased in excess of $10\,\mathrm{GHz}$ [114]. The key steps in the planarisation process are outlined below, with illustrations found in Figures 4.27a and 4.27b.

1. A deep etch ridge was formed and passivated with silicon dioxide as per

the method outlined in Section 4.6.2. Oxide passivation improves the adhesion of the BCB. See Figure 4.27a.

2. The chip was coated with BCB and cured at a high temperature ($\sim 250\,^{\circ}\mathrm{C}$) to solidify. Final thickness depends on application factors further elaborated on in reference [113]. See Figure 4.27a.

3. The BCB was etched back until the oxide on the top of the ridge was exposed. See Figure 4.27b.

4. Silicon dioxide was deposited beneath the position where the metal contact pad will be deposited. This was done to promote adhesion as metal typically has poor adhesion to BCB. A window was opened in the oxide and a metal contact was deposited as per the standard process. See Figure 4.27b

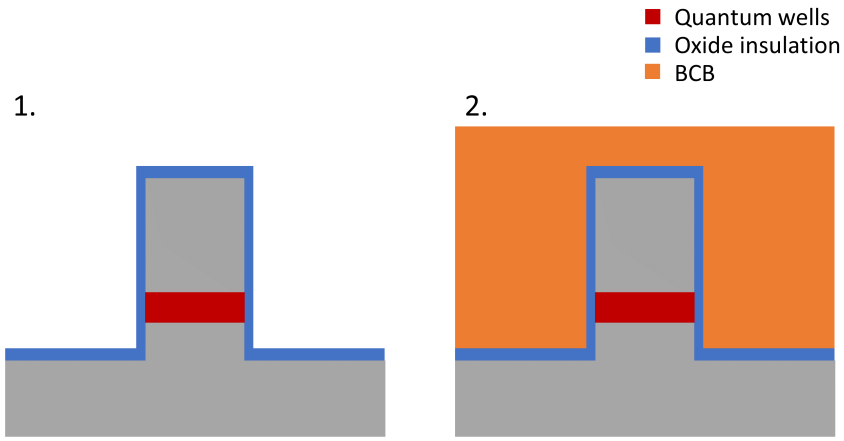

(a)

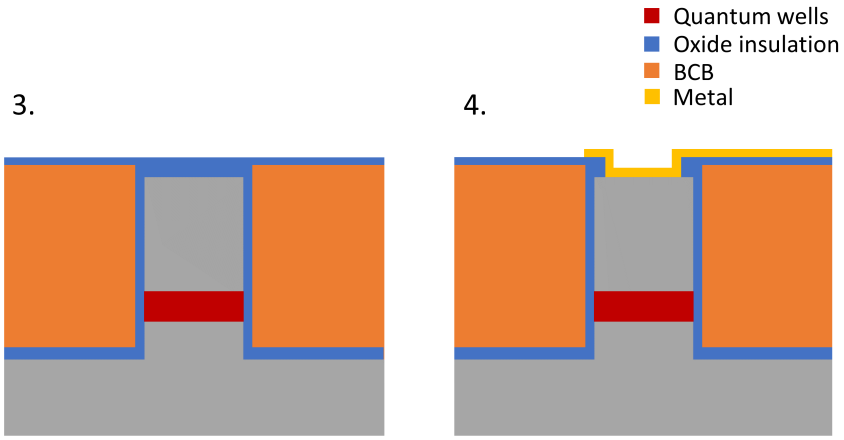

(b)

Figure 4.27: (a) Steps 1 and 2 of the high speed process illustrating the silicon dioxide passivated ridge in step 1, and the BCB application in step 2. (b) Steps 3 and 4 illustrate the BCB etch back to the top of the ridge in step 3, and the oxide opening and metal deposition in step 4. Oxide can be deposited beneath the contact pad before metal deposition to improve metal adhesion.

4.7 Conclusion

In this chapter, several devices were introduced and characterised. A set of Fabry-Pérot lasers featuring a combination of cleaved facets, etched facets, and metal coated etched facets were used to extract the reflectivity of etched facets and metal coated etched facets. These facet variations were used for the integration of Fabry-Pérots and slotted Fabry-Pérot lasers, with the metal coated etched facets providing a modest increase in reflectivity.

Slotted Fabry-Pérot lasers were used extensively in the design of devices for use in this thesis. As such, a brief overview of their structure and operation was given in this chapter. The relative simplicity in the design of these lasers was advantageous for this work, and their performance as gain-switched optical comb sources are detailed in the following chapter, Chapter 5.

Injection-locking was demonstrated off and on-chip. The advantages of injection-locking for gain-switched lasers was demonstrated theoretically in Chapter 3. With an experimental demonstration of the side-mode suppression provided by the technique shown in this chapter, the following chapter shall demonstrate the phase noise reduction during the gain-switching of lasers experimentally.

Lithography mask design, as well as the basic fabrication steps were detailed for the fabrication of the ridge waveguides and slot structures required for research devices.

In Chapter 5, low-linewidth optical combs are demonstrated from gain-switched, injection-locked lasers. Several devices are characterised, building on the work shown in this chapter.

Chapter 5

Low-Linewidth, Gain-Switched Optical Comb Sources

In Chapter 4, devices using etched facets and slots were characterised, and the design and fabrication of devices was discussed. In this chapter, the performance of the research devices fabricated for this thesis as optical comb sources is detailed. Each device made use of previously discussed features. The gain-switching experimental process is described with the aid of diagrams. As explained in previous chapters, the integration of two lasers was determined as the best course of action, with multiple variations of such devices described below. High-speed characterization was performed to determine RF limits on the modulation frequency that could be applied to the devices. The linewidth of each comb source was measured using the delayed self-heterodyne technique [115]. A prototype butterfly package designed for systems level experiments will also be discussed.

5.1 Optical Comb Source Devices

The following section is divided amongst each device fabricated for the purpose of optical comb generation. The structure and characterization of each device is included.

5.1.1 Slotted Fabry-Pérot Laser

5.1.1.1 Structure and Basic Characterization

An SFP laser was tested as an optical comb source. The structure and basic characterization of the device can be found in Chapter 4, Section 4.2, and as such will not be repeated here. The device schematic is reprinted in Figure 5.1a, as well as a microscope image of the device under test, Figure 5.1b, as a point of reference for the following sections.

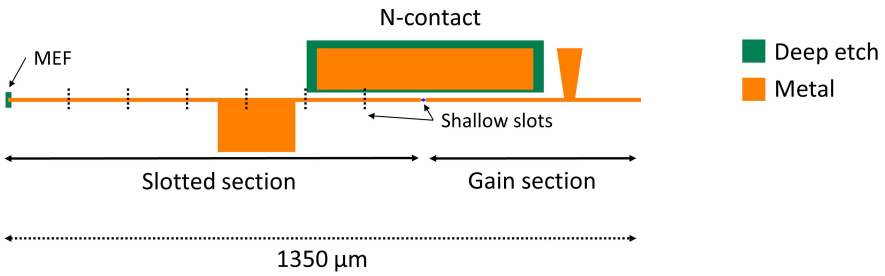

(a)

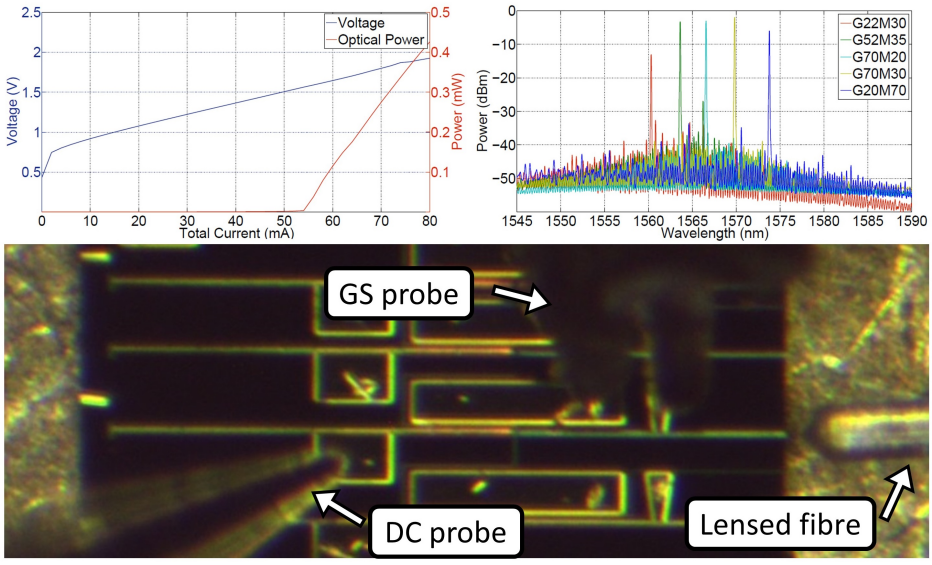

(b)

Figure 5.1: (a) SFP laser schematic with sections labelled. (b) Microscope image of fabricated SFP device under test. Ground-signal (GS) probe is visible for contacting the gain section and N-contact simultaneously, as well as a standard DC probe to the left and lensed fibre to the right. LIV and optical spectra are shown above the device image.

5.1.1.2 Modulation Bandwidth and Comb Generation

The device was mounted on a thermally controlled brass chuck maintained at $23\,^{\circ}\mathrm{C}$. A lensed optical fibre was used to couple light from the device, with probe needles used to apply bias to each device section. The modulation bandwidth of the device was investigated by measuring the S_{11} and S_{21} response of the slave section. These two parameters are called S, or scattering parameters. For a two port electrical system, the S_{11} is a measure of how much RF power is reflected from port one back to port one, while the S_{21} is a measure of how much RF power is transmitted from port one to port two. Thus by measuring the S parameters of a laser for a varying RF frequency, the amount of RF power reflected and transmitted can be determined. These quantities are useful for deducing the maximum RF frequency supported by a device.

The S_{11} response was obtained using an Agilent 8753ES two-port vector network analyser (VNA). The VNA sent a low power RF sinusoidal signal of varying frequency through the device from port one and measured the returning RF signal on port one of the VNA. A GS probe was used to make contact with the gain section and a DC bias was simultaneously applied via a bias tee. The GS probe used for this experiment was rated to a maximum of $40\,\mathrm{GHz}$. A schematic of the VNA test setup is shown in Figure 5.2.

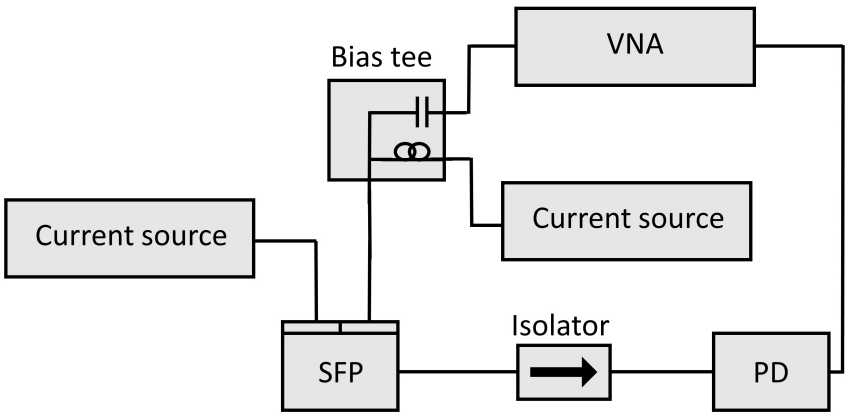

Figure 5.2: Experimental setup for obtaining S_{11} and S_{21} parameters. PD: Photodiode.

The VNA had a range of $30\,\mathrm{kHz}$ to $6\,\mathrm{GHz}$. The log mag S_{11} parameter vs. frequency for a gain section bias of $-2\,\mathrm{V}$ is shown in Figure 5.3. This bias was selected so as to reduce the intrinsic capacitance of the device, revealing the limit imposed by the structure of the contact pads.

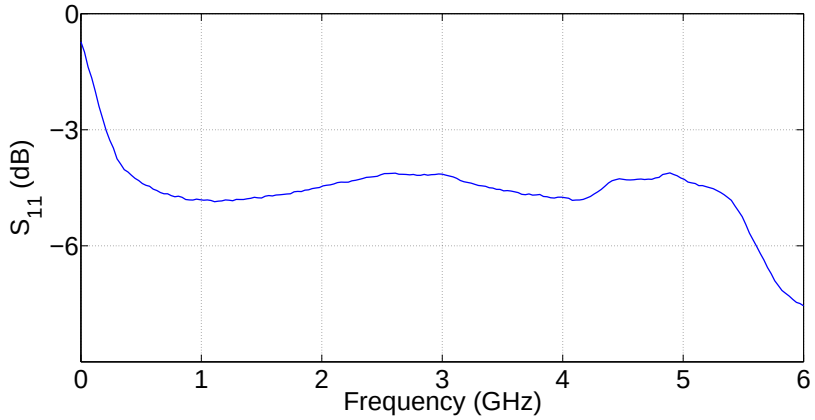

Figure 5.3: S_{11} log mag VNA data for SFP gain section biased at $-2\,\mathrm{V}$.

Figure 5.3 shows that over half the RF power applied to the SFP gain section is reflected for frequencies above $\sim 0.2\,\mathrm{GHz}$, with a sharper drop off after $5.5\,\mathrm{GHz}$.

To obtain the S_{21} measurement, the VNA sent a low power RF sinusoidal signal of varying frequency through the device from port one, which modulates the optical output of the device over the frequency range of the VNA. The optical signal was converted to an electrical signal using a photodiode (PD) and recorded through port two of the VNA. The S_{21} response of the device is shown in Figure 5.4 with the gain section and mirror section biased at $30\,\mathrm{mA}$ each.

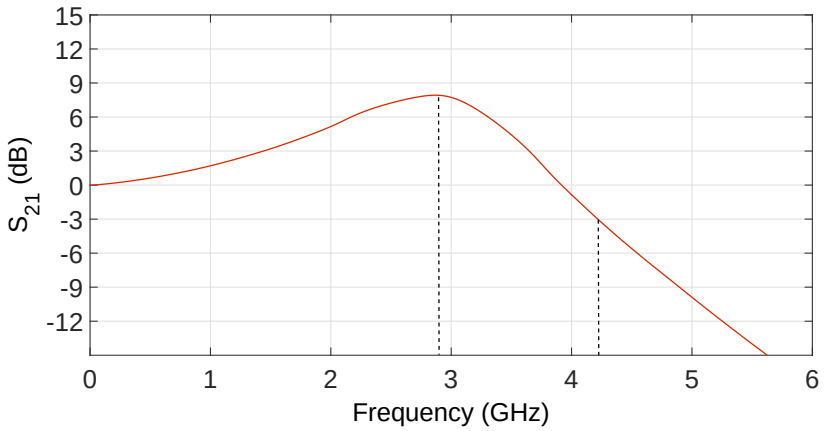

Figure 5.4: S_{21} log mag VNA data for SFP gain section biased at $30\,\mathrm{mA}$. Resonance peak is visible at $2.8\,\mathrm{GHz}$ with a $3\,\mathrm{dB}$ drop off at $4.2\,\mathrm{GHz}$.

The resonance peak of the laser is at $2.9\,\mathrm{GHz}$ with a $3\,\mathrm{dB}$ drop off at $4.2\,\mathrm{GHz}$. Thus this device is mostly limited by the optical resonance frequency. Nevertheless, gain-switching was attempted.

To gain-switch the device, an RF generator was used to produce the high power RF signal. A schematic of the experimental setup is shown in Figure 5.5. Optical spectra were recorded using an OSA with a wavelength resolution of $0.015\,\mathrm{nm}$.

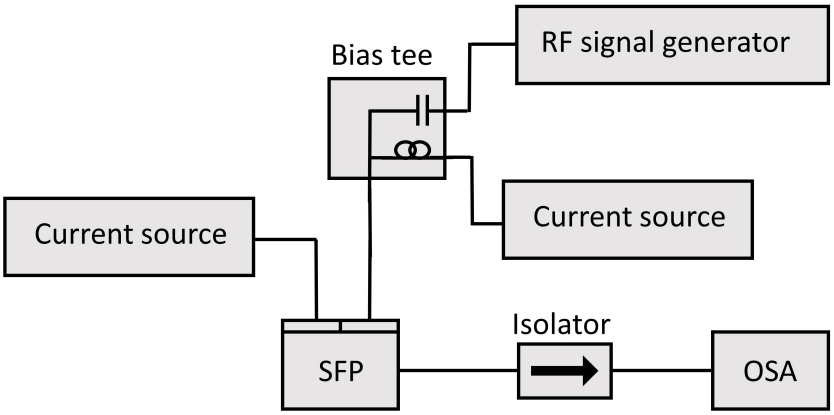

Figure 5.5: Experimental setup for gain-switching a diode laser. Simultaneous RF and DC bias is applied to the gain-switched section.

The gain and slotted sections were biased at $35\,\mathrm{mA}$ each and an optical spectrum was recorded. The spectrum is shown in Figure 5.6a. The gain and slotted sections were then biased at $72\,\mathrm{mA}$ and $34\,\mathrm{mA}$ respectively, and a $6\,\mathrm{GHz}$ $21\,\mathrm{dBm}$ RF signal was applied to the gain section. These bias currents were higher than the values used for the S_{21} measurement as the additionally device heating from the applied RF power caused a shift in the optical spectrum. The bias currents were tuned until a stable optical comb was generated. An RF power of $21\,\mathrm{dBm}$ was required to gain-switch the device due to the high RF losses due to impedance mismatch. The optical comb produced is shown in Figure 5.6b. The comb features 5 lines above $-20\,\mathrm{dBm}$ with unequal power. 2 lines are shown with optical power of approximately $-15\,\mathrm{dBm}$, and 3 lines with optical power of approximately $-18\,\mathrm{dBm}$.

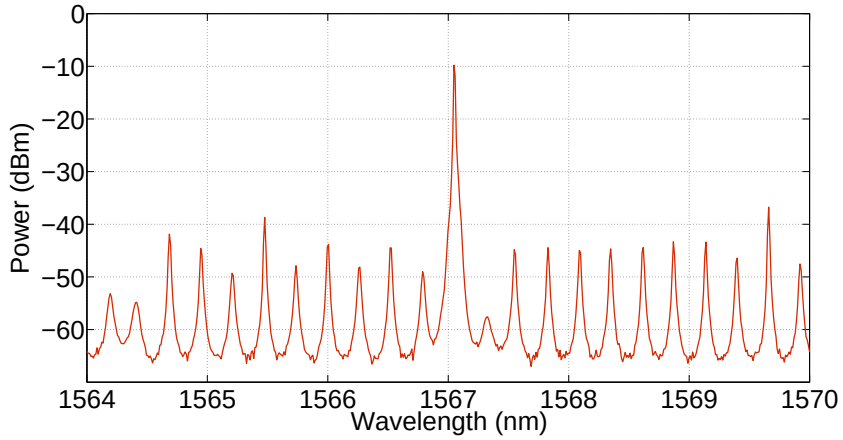

(a)

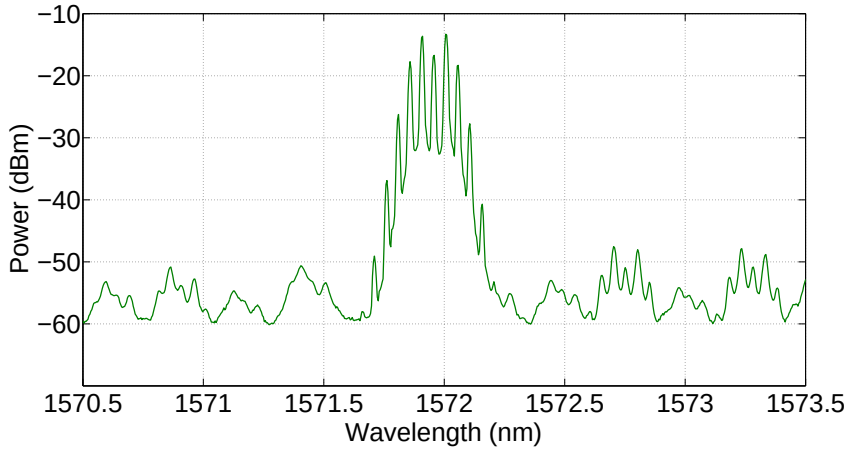

(b)

Figure 5.6: (a) Single mode optical spectrum of SFP device. Different mode spacings are shown in the spectrum due to the effect of multiple sub-cavities in the slotted laser. (b) Optical comb spectrum for SFP device.

5.1.1.3 Linewidth

The linewidth of the device was measured before and after gain-switching using the recirculating delayed self-heterodyne interferometer (RDSHI) method [116]. A schematic of the measurement setup is shown in Figure 5.7. For the gain-switched case, it was not possible to filter a single comb line for measurement due to equipment limitations. Thus the linewidth of the comb line set was measured, giving a weighted average linewidth of the comb lines. Light was coupled from the laser into a 90/10 splitter whereby 90% of the power went through the $50\,\mathrm{km}$ of fibre loop, and 10% was passed to a photodiode (PD). In the loop, the laser was frequency-shifted by $80\,\mathrm{MHz}$ with an acousto-optic modulator (AOM), and passed through a polarization

controller. The frequency shifted beam then recombines with the unshifted beam at the PD and the beat note at $80\,\mathrm{MHz}$ between the beams can be analysed on an electronic spectrum analyser (ESA). Higher order beat notes with decreasing power can be observed due to recirculation in the loop. As a delay length of 50 km gives a resolution of < 2 kHz, which was more than sufficient for this device, only the beat note at 80 MHz was recorded.

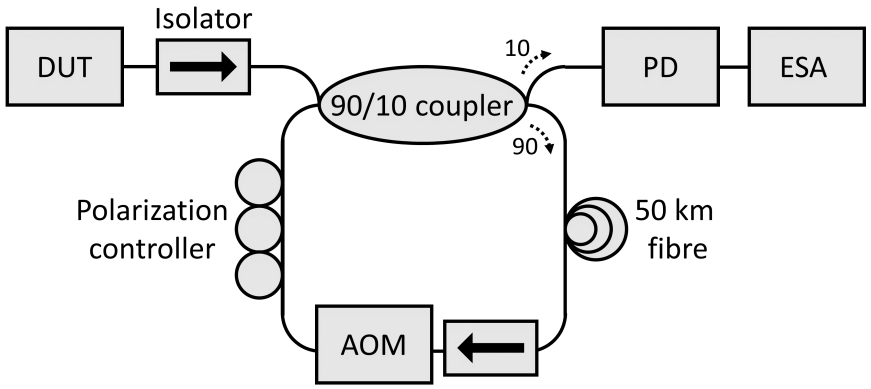

Figure 5.7: Schematic for the RDSHI linewidth measurement, where DUT is device under test, PD is photodiode, AOM is acousto-optic modulator, and ESA is electrical spectrum analyser.

The resolution bandwidth of the ESA was set to 100 kHz, with a sweep time of $60\,\mathrm{ms}$. For an optical comb, the RDSHI gives the linewidth of the comb set, thus providing a weighted average linewidth of all the comb lines.

The full-width half-maximum (FWHM) of the RDSHI measurement before gain-switching was $400\,\mathrm{kHz}$, increasing to $2\,\mathrm{MHz}$ for the gain-switched laser. The measurements are shown in Figure 5.8.

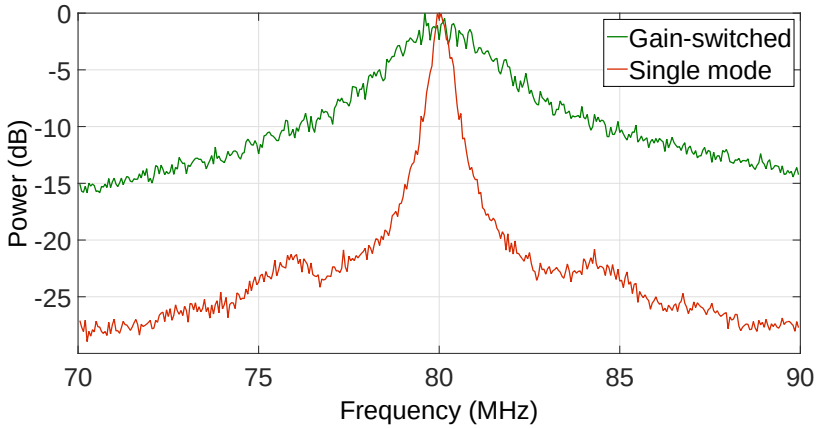

Figure 5.8: Overlapped linewidth measurement for the SFP device before and after gain-switching normalised to zero.

The linewidth of the laser is calculated from half the FWHM of the RDSHI measurement, giving linewidths of $200\,\mathrm{kHz}$ and $1\,\mathrm{MHz}$ for the single mode output and comb line set respectively. A 5 times increase in frequency noise is observed after the laser is gain-switched. Having demonstrated on-chip gain-switching, the next step was to add on-chip injection-locking, which is described in the next section.

5.1.2 Integrated SFP-SFP Device

5.1.2.1 Structure

Two SFP lasers were integrated on the same chip to investigate injection-locking and gain-switching. A high speed process was used to fabricate this device. More details on this fabrication process can be found in Section 4.6.3. The device is a two section SFP laser of total length $1350\,\mu\mathrm{m}$, integrated with a shorter SFP laser of length $680\,\mu\mathrm{m}$. The longer SFP is referred to as the master laser, the shorter SFP the slave. The ridge was shallow etched with a width of $2.5\,\mu\mathrm{m}$.

The master SFP has a $590\,\mu\mathrm{m}$ gain section, with a $760\,\mu\mathrm{m}$ slotted mirror section. The mirror section consists of 8 periodically spaced slots, with slot width $0.88\,\mu\mathrm{m}$, and slot depth of $1.79\,\mu\mathrm{m}$. The slot period is $108\,\mu\mathrm{m}$ giving a supermode spacing of $\sim 400\,\mathrm{GHz}$. The slave SFP has a $250\,\mu\mathrm{m}$ gain section, and a $430\,\mu\mathrm{m}$ mirror section. The mirror consists of 5 periodically spaced slots with the same slot width, period, and depth as before. The SFPs are coupled via a $15\,\mu\mathrm{m}$ long waveguide section. A separate etch through the quantum wells was performed in order to provide access to the n region. BCB was used to

planarise the structure before metal contact deposition. Ground-signal (GS) contacts were deposited in order to allow high-speed modulation of the device. The ground pad makes contact with the n-type substrate through a deep etched opening. A schematic of the device is shown in Figure 5.9a with each section labelled. A microscope image is shown in Figure 5.9b.

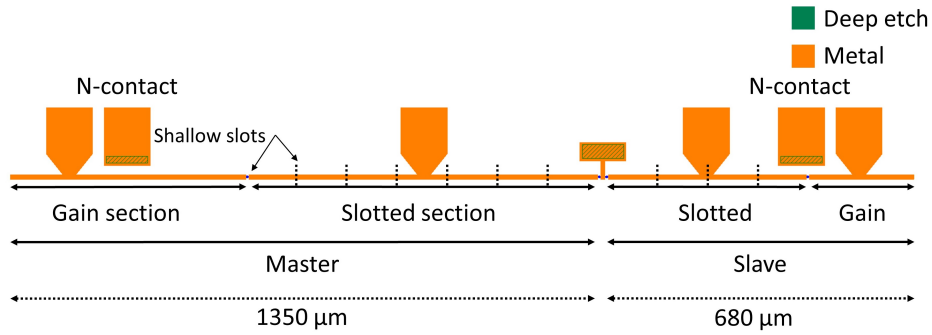

(a)

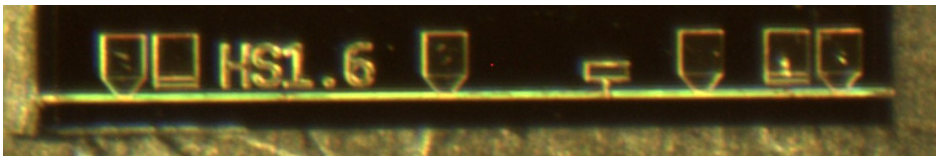

(b)

Figure 5.9: (a) Integrated SFP-SFP device in a master/slave configuration. Shallow etched slots separate each section. Black dotted lines indicate the position of shallow etched slots in the slotted sections. (b) Microscope image of device. Text on the device refer to its position on the mask.

5.1.2.2 Characterization

The longer SFP is referred to as the master laser, with the shorter SFP being the slave laser. The device was mounted on a thermally controlled brass chuck maintained at $23\,^{\circ}\mathrm{C}$. Probe needles contacted the pads of the slave laser. Lensed fibre was used to couple light from the device. The slave laser was found not to lase. Up to $80\,\mathrm{mA}$ was applied to the 5 slot mirror section and the $250\,\mu\mathrm{m}$ gain section respectively with little increase in optical power detected. As such, characterization experiments were not continued. It was thought that the device was too short to provide enough gain to achieve lasing, and this was proven to be the case with an experiment outlined in the following section.

The device was found to lase as a whole with the master laser switched on. The single mode output of the device with a bias of $20\,\mathrm{mA}$, $0\,\mathrm{mA}$, $40\,\mathrm{mA}$, and $40\,\mathrm{mA}$, in the slave gain, slave mirror, master mirror, and master gain sections

respectively, is shown in Figure 5.10. Thesis bias values were determined by manual adjustments while observing OSA traces.

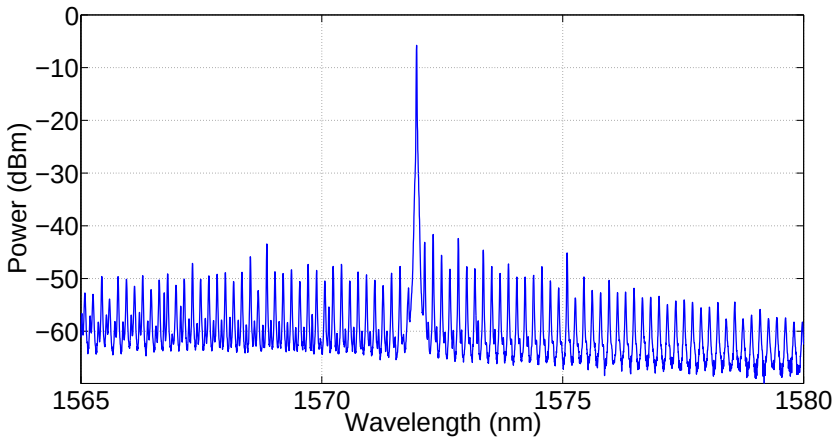

Figure 5.10: Single mode output from SFP-SFP compound laser. Emitted mode is at a wavelength of $\sim 1572\,\mathrm{nm}$.

Due to the non-lasing of the slave independantly with this design, attention was moved to a variation of an integrated SFP-SFP device which shared a mirror section between the two lasers. The SFP-SFP device presented here will be discussed in Chapter 6 for its use in testing a prototype butterfly package [44].

5.1.3 Integrated SFP-SFP Device - Common Mirror

5.1.3.1 Structure

The device described here features two single facet SFP lasers integrated in such a way that they share a slotted mirror section [34, 56]. By sharing a common mirror section, the integration of two SFP lasers was simplified. The ridge was shallow etched to a width of $2.5\,\mu\mathrm{m}$. The mirror section was a length of $756\,\mu\mathrm{m}$, with the master/slave sections $800\,\mu\mathrm{m}$ and $400\,\mu\mathrm{m}$ respectively. The slot period used in the mirror is $108\,\mu\mathrm{m}$. A schematic is shown in Figure 5.11a. This device was fabricated during the same process run as the device in Section 5.1.2. A microscope image is shown in Figure 5.11b.

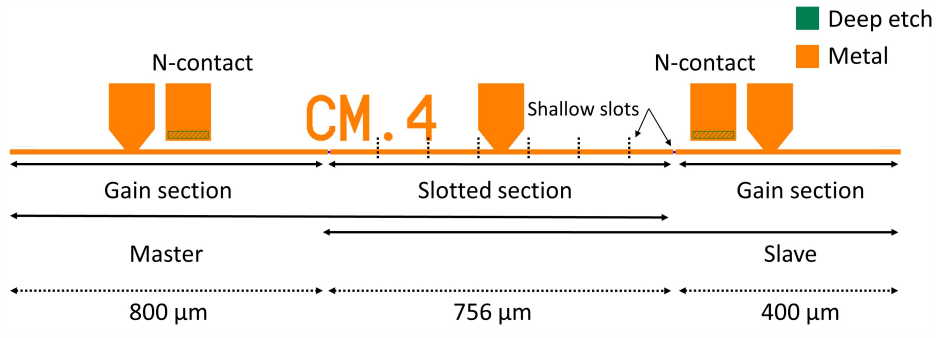

(a)

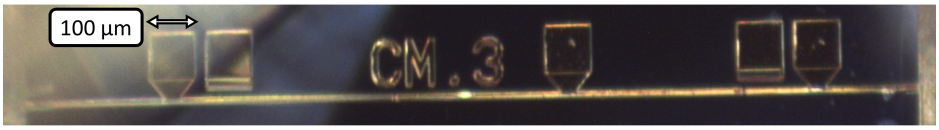

(b)

Figure 5.11: (a) Master/slave configuration SFP lasers with common slotted mirror section. Shallow etched slots separate each section. Black dotted lines indicate the position of shallow etched slots in the slotted sections. (b) Microscope image of common mirror device.

Several variations were fabricated with slave section lengths ranging from $800\,\mu\mathrm{m}$ to $300\,\mu\mathrm{m}$, decreasing by $100\,\mu\mathrm{m}$.

5.1.3.2 Characterization

The device was mounted on the thermally controlled brass chuck maintained at $24\,^{\circ}\mathrm{C}$. Probe needles contacted the pads of the device. LI curves were obtained from the set of common mirror devices by sweeping the bias of the slave section from 0 - $100\,\mathrm{mA}$. The mirror section was maintained at $40\,\mathrm{mA}$, while the master section was reverse biased to $-2\,\mathrm{V}$. Rather than coupling light from the device using a lensed fibre, the photo current measured from the master section was used to generate the LIs. The conversion formula for photo current to optical power is derived as follows;

$$1\,\mathrm{A} = 1\,\mathrm{C\,s^{-1}} \tag{5.1}$$

$$1\,\mathrm{C\,s^{-1}} = 6.25 \times 10^{18}\,\mathrm{electrons/s} \tag{5.2}$$

The energy of n photons is given by,

$$E = n\frac{c}{\lambda}h \tag{5.3}$$

where c is the speed of light, λ is the wavelength, and h is Planck's constant. Assuming that one photon generates one electron, the optical power can be estimated. This assumption was used as the primary concern was the threshold current of each laser, and the general shape of the LI, not the absolute power. The power in Watts is given by,

$$\text{Power (Watts)} = (6.25 \times 10^{18}\,\text{photons/s})\frac{c}{\lambda}h \tag{5.4}$$

Using Equation 5.4 the LI of the devices was plotted in Figure 5.12. Roll-off in the optical power is shown for shorter device lengths as the increased current density leads to increased heating, reducing efficiency.

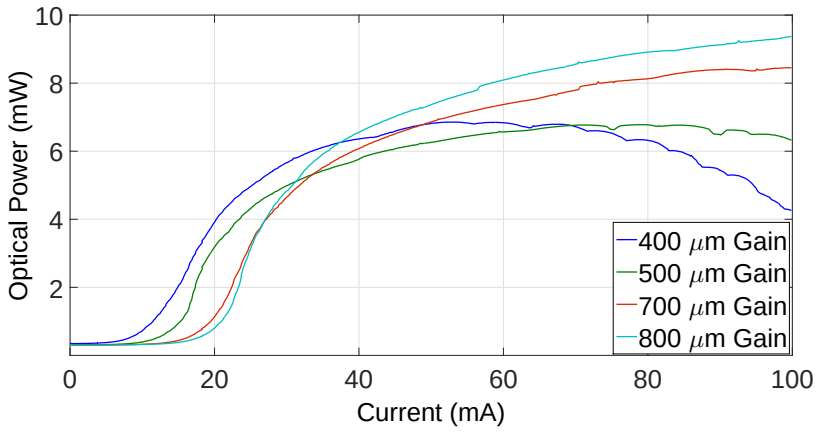

Figure 5.12: LIs for varies gain section lengths. Lasers with gain lengths of $300\,\mu\text{m}$ did not lase, and were not recorded. These results determine the minimum gain section length to be $400\,\mu\text{m}$ for the 7 slot mirror section used.

The slave length of $300\,\mu\text{m}$ was found not to lase, therefore the result was not recorded as there was not enough optical power emitted to accurately align a lensed fibre. The minimum gain section length required for a 7 slot mirror section was determined to be $400\,\mu\text{m}$. Thus the lack of lasing from the slave SFP in Section 5.1.2 was due to insufficient length to provide gain as the amount of current required to reach threshold will contribute to internal heating, reducing the efficiency. Further characterization was focused on the common mirror device with a $400\,\mu\text{m}$ slave section.

5.1.3.3 Injection-Locking and Tunability

Slave and mirror sections were biased at $20\,\text{mA}$ and $30\,\text{mA}$ respectively, with the master section unbiased. An optical spectrum was recorded using an OSA. The master section was then switched on with a bias of $50\,\text{mA}$. The optical

spectrum of the slave output is shown in Figure 5.13a for master on/off. Single mode behavior was observed with a high SMSR ($> 30\,\mathrm{dB}$) with the slave optically phase locked to the master. By varying the bias of the master and mirror sections, 4 main lasing modes were obtained. The tunability of the device is shown in Figure 5.13b, with lasing modes at $1573.1\,\mathrm{nm}$ (slave: $20\,\mathrm{mA}$, mirror: $17\,\mathrm{mA}$, master: $40\,\mathrm{mA}$), $1576.5\,\mathrm{nm}$ (slave: $20\,\mathrm{mA}$, mirror: $30\,\mathrm{mA}$, master: $30\,\mathrm{mA}$), $1579.7\,\mathrm{nm}$ (slave: $20\,\mathrm{mA}$, mirror: $30\,\mathrm{mA}$, master: $50\,\mathrm{mA}$), $1583.9\,\mathrm{nm}$ (slave: $20\,\mathrm{mA}$, mirror: $14\,\mathrm{mA}$, master: $51\,\mathrm{mA}$). The wavelength jumps of roughly $3.2\,\mathrm{nm}$ ($400\,\mathrm{GHz}$ channel spacing) are defined by the interslot distance in the mirror section stated in the previous section. The mode intensities could be leveled with the addition of a semiconductor optical amplifier (SOA) integrated with the laser in future designs [102].

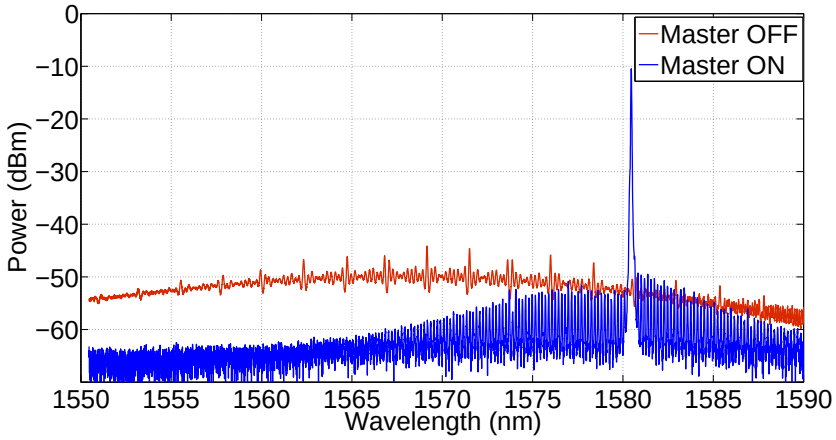

(a)

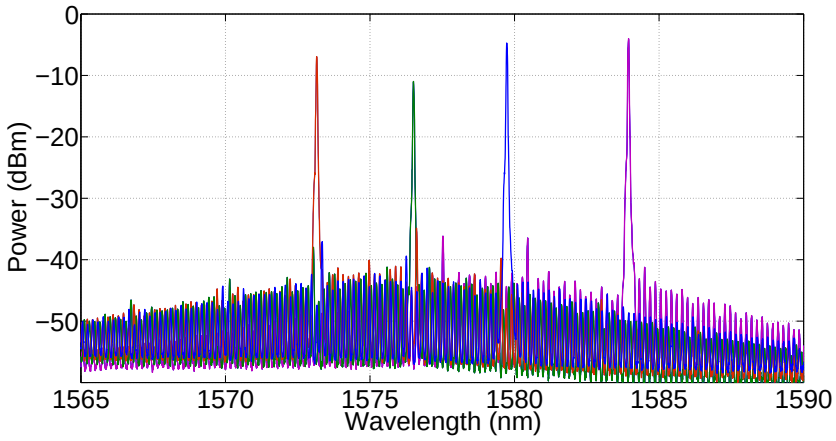

(b)

Figure 5.13: (a) Slave output before/after master section injection. (b) Optical spectrum with varying master and mirror bias showing lasing modes at $1573.1\,\mathrm{nm}$ (slave: $20\,\mathrm{mA}$, mirror: $17\,\mathrm{mA}$, master: $40\,\mathrm{mA}$), $1576.5\,\mathrm{nm}$ (slave: $20\,\mathrm{mA}$, mirror: $30\,\mathrm{mA}$, master: $30\,\mathrm{mA}$), $1579.7\,\mathrm{nm}$ (slave: $20\,\mathrm{mA}$, mirror: $30\,\mathrm{mA}$, master: $50\,\mathrm{mA}$), $1583.9\,\mathrm{nm}$ (slave: $20\,\mathrm{mA}$, mirror: $14\,\mathrm{mA}$, master: $51\,\mathrm{mA}$)

5.1.3.4 Modulation Bandwidth and Comb Generation

Using the method outlined in Section 5.1.1.2, the log mag S_{11} parameter vs. frequency for a slave section bias of $-2\,\mathrm{V}$ is shown in Figure 5.14.

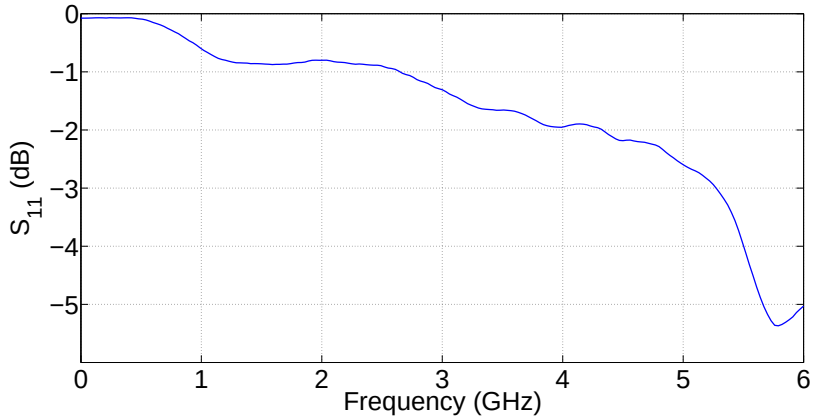

Figure 5.14: S_{11} log mag VNA data for slave section biased at $-2\,\mathrm{V}$.

The reduced reflection at low frequencies due to the high speed fabrication process is apparent when compared to the SFP S_{11} in Figure 5.3. The $3\,\mathrm{dB}$ drop off point is at $\sim 5.3\,\mathrm{GHz}$. The sharp drop after this point was due to the low specification GS probe used for the measurement, which was rated to $7\,\mathrm{GHz}$.

The S_{21} response was next measured, as outlined in Section 5.1.1.2, and was plotted in Figure 5.15a. For a slave and mirror bias of $40\,\mathrm{mA}$ and $50\,\mathrm{mA}$ respectively, the resonance frequency of the slave was measured to be $2.5\,\mathrm{GHz}$, with a 3 dB drop off at 3.5 GHz. For RF signals above $3.5\,\mathrm{GHz}$, the signal experiences an increasing loss in the device. The resonance frequency was increased to $3.5\,\mathrm{GHz}$, with a 3 dB drop off at almost $5\,\mathrm{GHz}$ by biasing the slave section at $20\,\mathrm{mA}$, the mirror section at $30\,\mathrm{mA}$, and by biasing the master section at $50\,\mathrm{mA}$. Thus the device is shown to be limited more by the optical transit time than by the capacitance of the structure.

To generate an optical comb, the slave section was gain-switched by applying a high power RF sinusoidal signal ($> 20\,\mathrm{dBm}$) at $4\,\mathrm{GHz}$ from a signal generator in order to directly modulate the current. A $4\,\mathrm{GHz}$ modulation frequency was chosen as this value is within the bandwidth of the device when all three sections are biased, but exceeds the bandwidth with the master section unbiased. The slave laser DC bias was tuned in order to obtain the best comb (slave: $40\,\mathrm{mA}$, mirror: $54\,\mathrm{mA}$), with the master section unbiased. The output of the slave was recorded using an OSA. The master section was switched on and all three sections tuned in order to obtain the best comb (slave: $20\,\mathrm{mA}$, mirror: $54\,\mathrm{mA}$, master: $30\,\mathrm{mA}$. The optical combs obtained from both of these configurations is shown in Figure 5.15b. With the master on, the number of comb lines obtained was nearly doubled. 8 comb lines were observed within a $3.5\,\mathrm{dB}$ band of each other, as opposed to 3 lines for the slave

and mirror comb. The comb generated with all three sections biased was observable from both device outputs, with no apparent asymmetry due to the stable coupling between master and slave lasers.

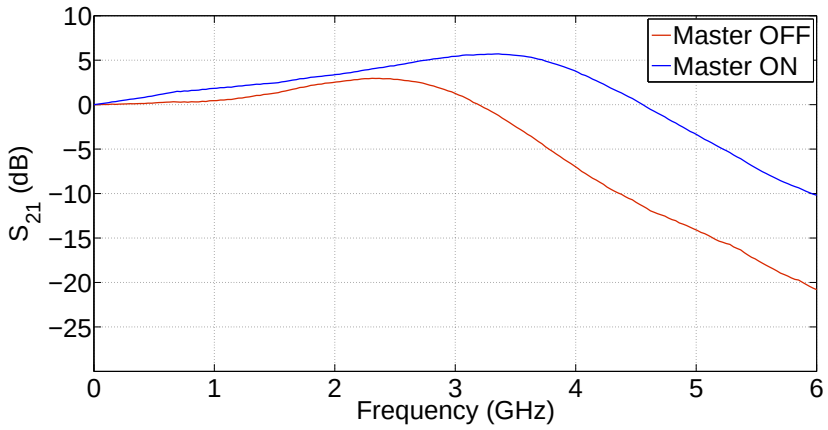

(a)

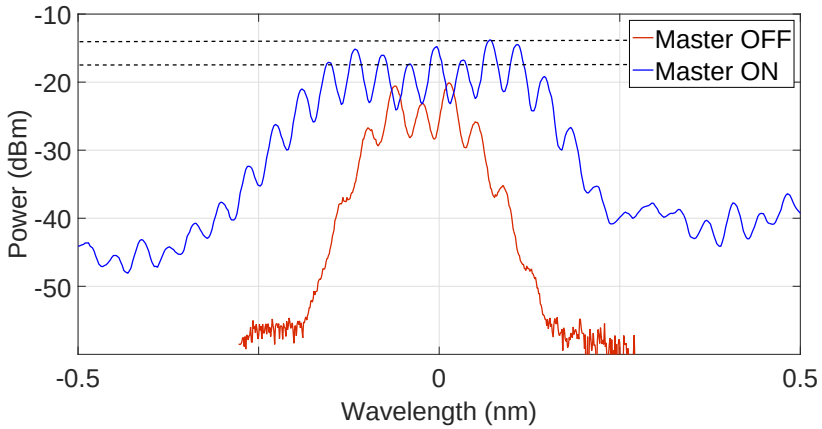

(b)

Figure 5.15: (a) S_{21} for slave laser before/after master section injection. (b) $4\,\mathrm{GHz}$ optical comb with master ON/OFF. The master ON comb is centred at $1580.3\,\mathrm{nm}$, the master OFF comb at $1586.9\,\mathrm{nm}$. This difference arises as the slave section required higher biasing to generate a comb with the master OFF.

5.1.3.5 Linewidth

The linewidth was measured using the setup outlined in Section 5.1.1.3, Figure 5.7. The resolution bandwidth of the ESA was set to 100 kHz, with a sweep time of $60\,\mathrm{ms}$. The beat note for the unmodulated device, the injection locked gain-switched device, and a commercial (distributed feedback) DFB laser (JDSU CQF915) is shown in Figure 5.16. The FWHM at $-3\,\mathrm{dB}$ from the peak was measured as: $\sim 250\,\mathrm{kHz}$ for the unmodulated device (slave: $20\,\mathrm{mA}$,

mirror: 30 mA, master: 50 mA), ~300 kHz for the gain-switched device (slave: 20 mA, mirror: 54 mA, master: 30 mA), and ~1.3 MHz for the DFB. The linewidth of the comb set was found not to broaden significantly as a result of gain-switching, with the measured linewidth considerably lower than that of the DFB laser. The comb set linewidth of 300 kHz is ideal for current state of the art 16-QAM (quadrature amplitude modulation) coherent communication systems which have a linewidth tolerance of 1.4 MHz (at 10 GBaud) [12].

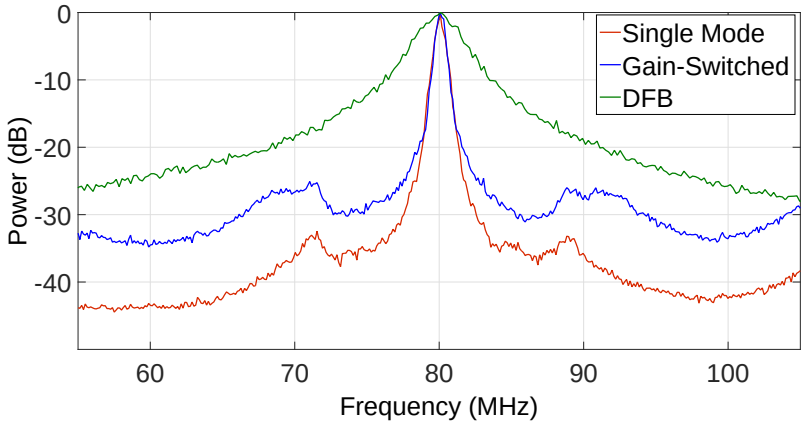

Figure 5.16: Measured linewidths for the device (modulated/unmodulated), and commercial DFB normalised to zero.

5.1.3.6 RF Linewidth

To measure the coherence between the comb lines, the beating of the unfiltered "Master On" 4 GHz optical comb lines shown in Figure 5.15b on a photodiode was examined on an ESA. The comb was converted to an electrical spectrum using a photodiode. The experimental setup is shown in Figure 5.17.

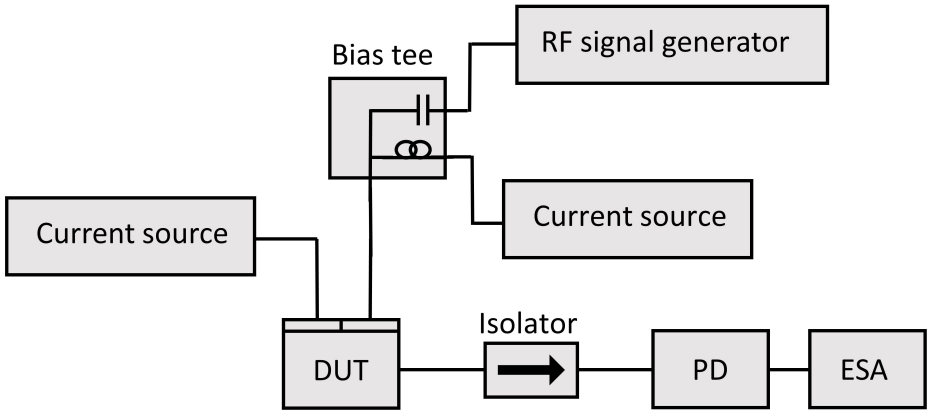

Figure 5.17: Experimental setup for measuring comb coherence. Optical comb source (DUT) has its spectrum converted to an electrical spectrum using a photodiode, and is examined on an ESA.

The ESA resolution bandwidth was set to $300\,\mathrm{kHz}$. The measured electrical spectrum is shown in Figure 5.18.

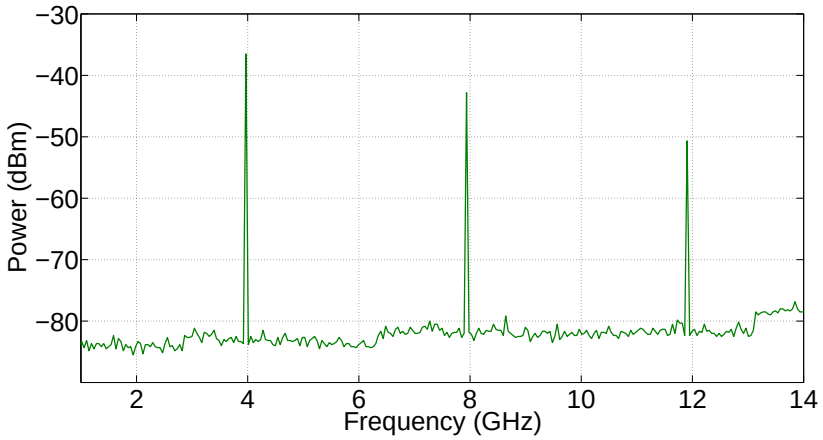

Figure 5.18: RF beat notes between the comb lines visible at $\sim 4\,\mathrm{GHz}$, $\sim 8\,\mathrm{GHz}$, and $\sim 12\,\mathrm{GHz}$.

The narrow peaks at $\sim 4\,\mathrm{GHz}$, $\sim 8\,\mathrm{GHz}$, and $\sim 12\,\mathrm{GHz}$, indicate a high degree of coherence as the beating of coherent signals results in a delta function, and correspond to the beat notes between the comb lines. These beat notes were found to have a linewidth on the order of the resolution of the ESA ($1\,\mathrm{kHz}$) when examined closely.

5.1.4 Integrated SFP-FP Device

The following structures to be examined were fabricated using the standard process outlined in Chapter 4 so as to reduce fabrication complications and increase device yield, at the expense of increased RF reflections from the devices.

5.1.4.1 Structure and Injection-Locking

The device structure was outlined in Chapter 4 and shall not be repeated here. This device did not use a high-speed process to limit capacitance. The device schematic is reprinted in Figure 5.19a, as well as a microscope image of the device under test, see Figure 5.19b, as a point of reference for the following sections.

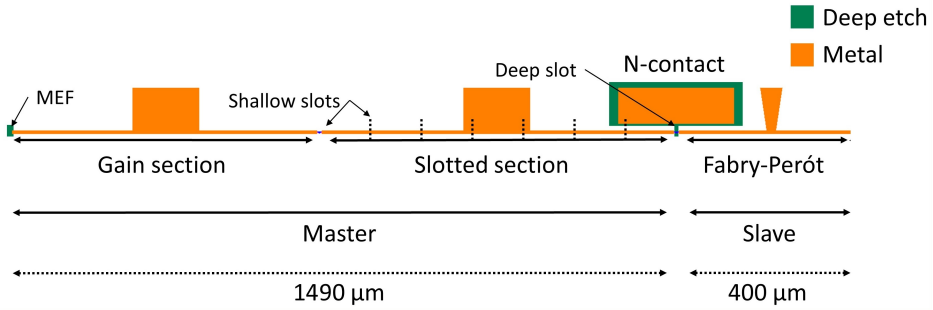

(a)

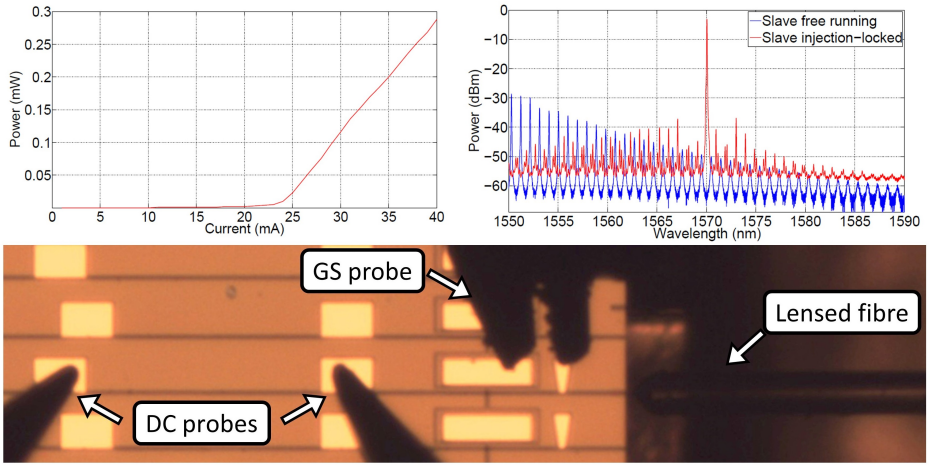

(b)

Figure 5.19: (a) SFP laser integrated with FP laser via an etched facet in a master/slave configuration. (b) Microscope image of fabricated SFP-FP device under test. GS probe is visible making contact with the slave laser, with DC probes to the left, and optical fibre on the right. An LI for the Fabry-Pérot and optical spectra are shown above the device image.

5.1.4.2 Modulation Bandwidth and Comb Generation

The S_{11} and S_{21} response of the slave laser was measured using the method outlined in Section 5.1.1.2, Figure 5.2. For a slave section bias of $-2\,\mathrm{V}$, the log mag S_{11} was recorded and plotted in Figure 5.20. The GS probe used for this experiment was rated to $40\,\mathrm{GHz}$.

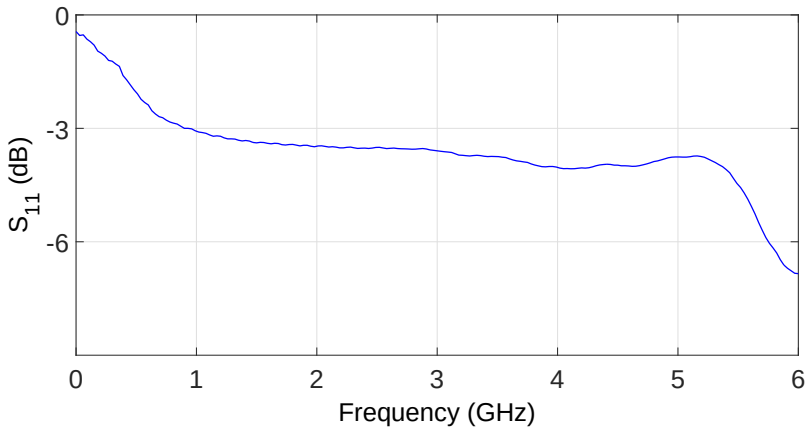

Figure 5.20: S_{11} log mag VNA data for FP slave laser biased at $-2\,\mathrm{V}$.

Over half the RF power is reflected for frequencies above $1\,\mathrm{GHz}$. This is a slight improvement on the S_{11} obtained for the SFP gain section shown in Figure 5.3 fabricated using the same process. An expected result, as the FP laser is $150\,\mu\mathrm{m}$ shorter.

The S_{21} response was recorded for the FP laser with the SFP laser both off and on. The FP laser was biased at $35\,\mathrm{mA}$ with the SFP laser sections off, and the S_{21} response was recorded as described in Section 5.1.1.2. The SFP was then switched on, with $70\,\mathrm{mA}$ applied to the gain section and $90\,\mathrm{mA}$ to the slotted section, and the S_{21} response was recorded. The S_{21} for both cases is plotted in Figure 5.21.

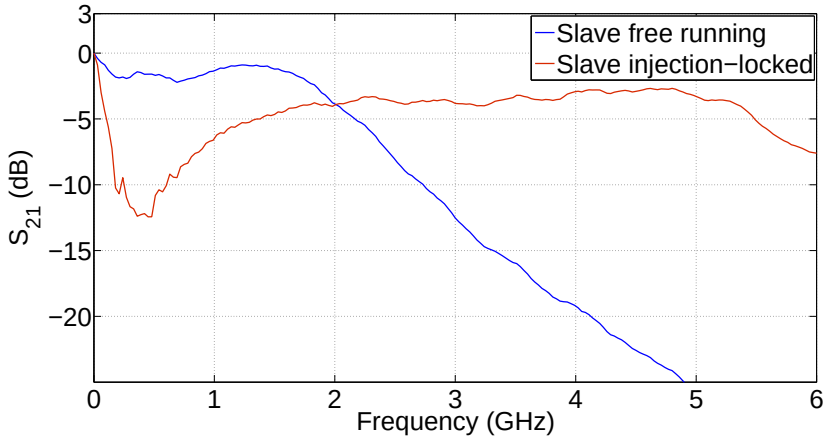

Figure 5.21: S_{21} log mag VNA data for FP slave laser biased at $35\,\mathrm{mA}$ with SFP laser off/on.

The S_{21} response for the injection-locking FP laser is an improvement over the S_{21} for the common mirror device shown in Figure 5.15a. The response is flat, at about $-4\,\mathrm{dB}$ with the drop off at $\sim 5.3\,\mathrm{GHz}$ corresponding to the drop off in the S_{11} response. This indicates that the modulation of the device is limited more by the impedance of the device structure, than by the optical transit time.

The device was next gain-switched to produce an optical comb. The gain and slotted sections of the SFP were biased at $35\,\mathrm{mA}$ and $51\,\mathrm{mA}$ respectively, with the FP biased at $57\,\mathrm{mA}$. A $5\,\mathrm{GHz}$ $22\,\mathrm{dBm}$ RF signal was applied to the FP section, using the setup to that described in Figure 5.5. The optical comb produced is shown in Figure 5.22. The asymmetry in the comb is likely due to the modulation of the laser output from the cavity lengths in the device.

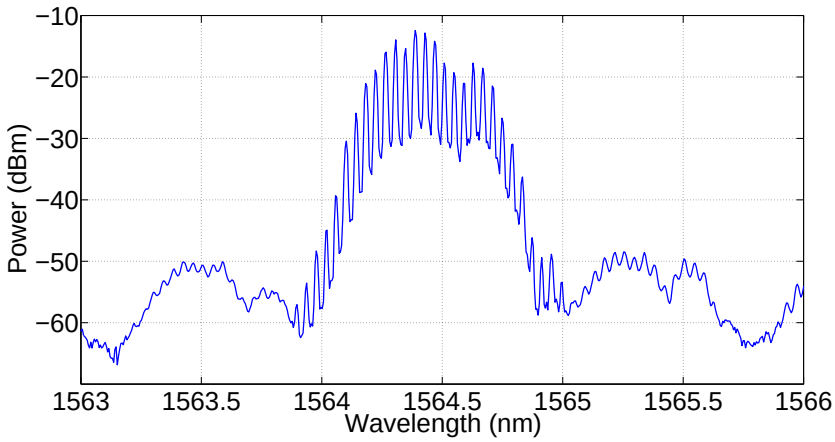

Figure 5.22: $5\,\mathrm{GHz}$ optical comb spectrum generated from integrated SFP-FP device.

It was found that by driving the FP laser with higher biases, optical combs with line spacings of up to $10\,\mathrm{GHz}$ could be obtained, see Figure 5.23. The

optical power for this comb is much lower, as the device is being modulated above it's limit. Such line spacings could not be achieved with the common mirror device described in 5.1.3. Less asymmetry is shown in this comb as the span of the comb is half the span of the comb in Figure 5.22.

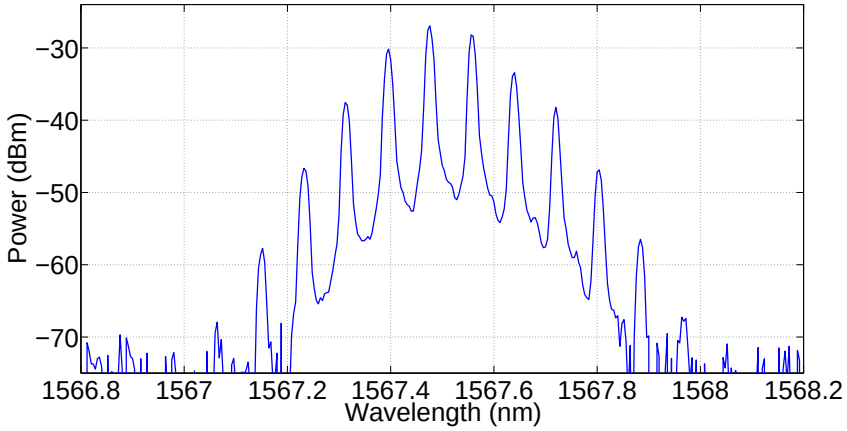

Figure 5.23: $10\,\mathrm{GHz}$ optical comb spectrum generated from integrated SFP-FP device.

5.1.4.3 Linewidth

The linewidth of the laser emission was measured both before and after gain-switching, using the setup described in Section 5.1.1.3, Figure 5.7. The resolution bandwidth of the ESA was set to 100 kHz, with a sweep time of $60\,\mathrm{ms}$. The SFP was biased with $42\,\mathrm{mA}$ and $46\,\mathrm{mA}$ in the gain and slotted sections respectively, with the FP biased at $61\,\mathrm{mA}$, to obtain a single mode output. The optical spectrum is plotted in Figure 5.24. The linewidth of this optical signal was recorded, and compared with a linewidth measurement recorded for the $5\,\mathrm{GHz}$ optical comb shown in Figure 5.22.

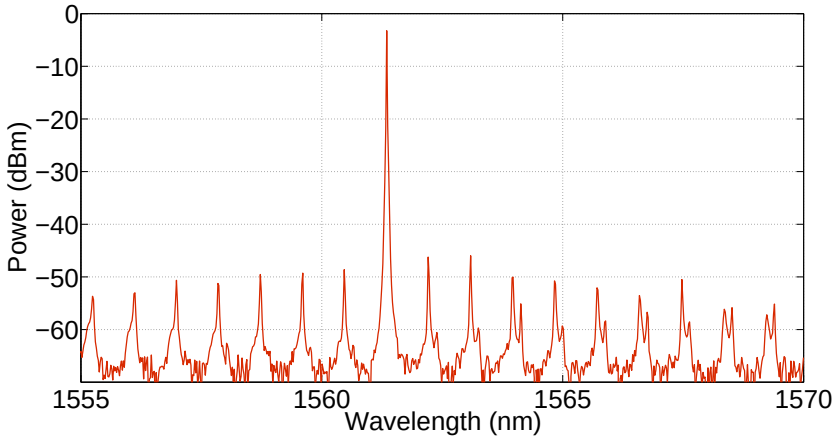

Figure 5.24: Single mode optical spectrum for SFP-FP device. The effect of the couple sub-cavities of the device is shown in the mode spacings of the spectrum.

The FWHM of the RDSHI measurement before gain-switching was $700\,\mathrm{kHz}$. After gain-switching the RDSHI measurement was also approximately $700\,\mathrm{kHz}$. The measurements are shown in 5.25. This gives a linewidth of approximately $350\,\mathrm{kHz}$ (half the value of the FWHM is taken as the laser is beating with itself) with no major increase in frequency noise due to gain-switching. The linewidth of the FP laser with the master laser off could not be measured due to small optical power output [100].

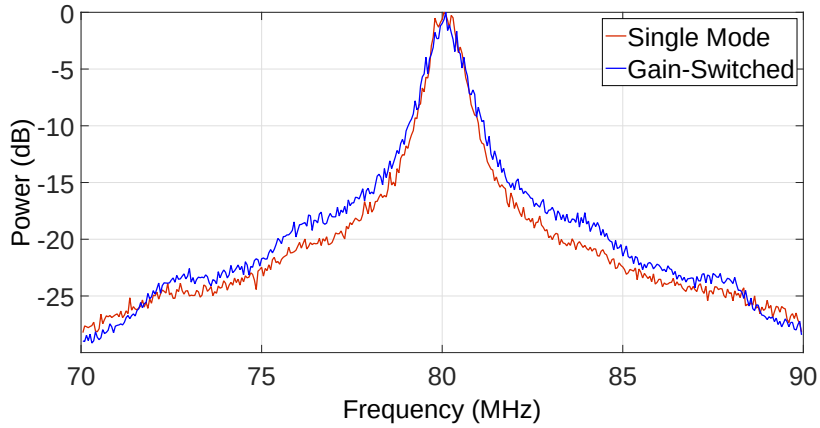

Figure 5.25: Overlapped linewidth measurement for SFP-FP device before and after gain-switching normalised to zero.

5.1.4.4 RF Linewidth

The coherence between the $5\,\mathrm{GHz}$ unfiltered optical comb lines shown in Figure 5.22 was measured using the experimental setup from Figure 5.17. The ESA resolution bandwidth was set to $300\,\mathrm{kHz}$. The measured electrical spectrum is shown in Figure 5.26.

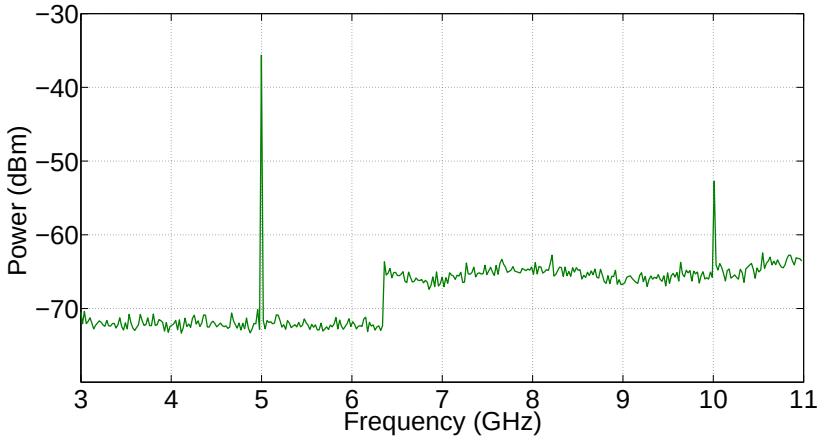

Figure 5.26: RF beat notes between the comb lines visible at $5\,\mathrm{GHz}$, and $10\,\mathrm{GHz}$. The noise floor increase just after $6\,\mathrm{GHz}$ was characteristic of the ESA.

The narrow peaks at $5\,\mathrm{GHz}$, and $10\,\mathrm{GHz}$, indicate a high degree of coherence, and correspond to the beat notes between the comb lines.

The $5\,\mathrm{GHz}$ beat note was examined in more detail by decreasing the resolution bandwidth of the ESA to $1\,\mathrm{kHz}$, over a span of $40\,\mathrm{kHz}$. The RF beat note is shown in Figure 5.27.

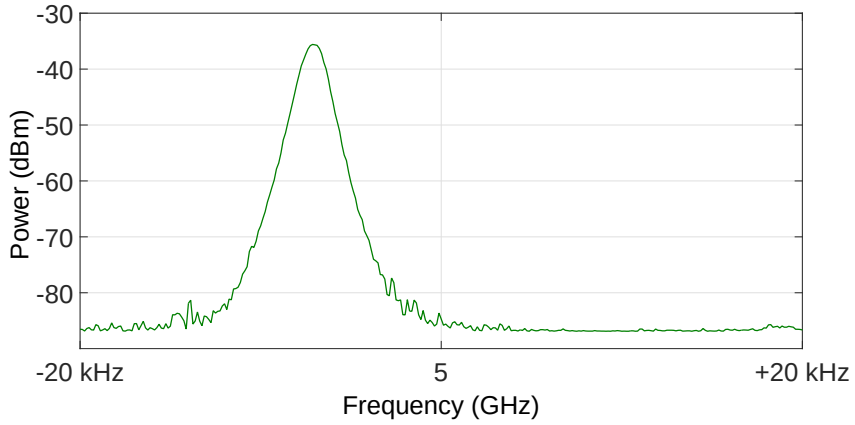

Figure 5.27: $5\,\mathrm{GHz}$ RF beat note with ESA resolution bandwidth set to $1\,\mathrm{kHz}$

The RF linewidth of the beat note is on the order of the resolution bandwidth of the ESA, indicating an extremely high level of coherence between the comb lines. The slight displacement from the expected $5\,\mathrm{GHz}$ is due to error with the RF generator.

5.1.5 Facetless SFP-FP Device

5.1.5.1 Structure

As a first step towards further integration of optical components and the design of a fully integrated AO-OFDM PIC, a facetless version of the device outlined in Section 5.1.4 was fabricated [117]. This device removes reliance on cleaved facets, and consists of a $1300\,\mu\mathrm{m}$ slotted Fabry-Pérot (SFP) laser coupled to a $400\,\mu\mathrm{m}$ Fabry-Pérot (FP) laser, with a $230\,\mu\mathrm{m}$ angled (7°) waveguide to couple light out of the FP laser while reducing unwanted reflections. The SFP laser is a two section device consisting of a $500\,\mu\mathrm{m}$ gain section, and an $800\,\mu\mathrm{m}$ slotted section with 7 periodically spaced slots. The slot widths are $1\,\mu\mathrm{m}$ wide with the slot period approximately $114\,\mu\mathrm{m}$. A deep etch was used to define both the etched facets and a top level N-contact. A microscope image is shown in Figure 5.28b

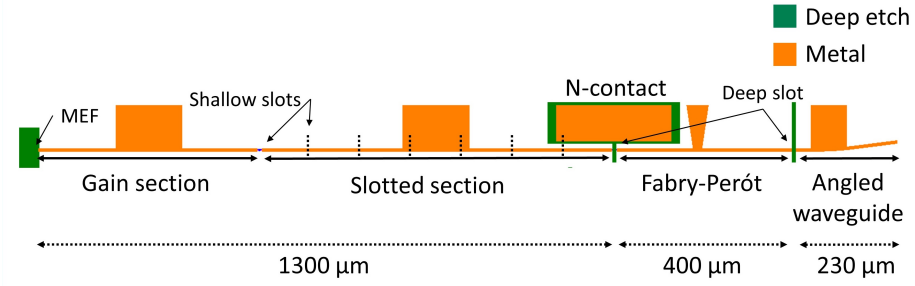

(a)

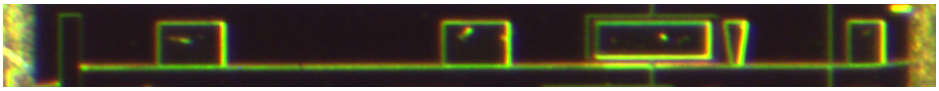

(b)

Figure 5.28: (a) Schematic of device showing metal contact pads, with each section labelled. The Fabry-Pérot cavity is formed by two etched facets. The deep etch areas are etched through the quantum wells of the material. A shallow etched slot separates the gain and slotted sections, with further shallow etched slots indicated by the dotted black lines. (b) Microscope image of the fabricated device.

5.1.5.2 Injection-Locking and Gain-Switching

Injection-locking of the FP laser was first investigated. The FP laser and angled waveguide was biased at $80\,\mathrm{mA}$ and $12\,\mathrm{mA}$ respectively, and the optical spectrum was recorded by the OSA. The SFP was then biased with $42\,\mathrm{mA}$ and $33\,\mathrm{mA}$ to the gain and slotted sections, respectively. The emission spectrum for

the FP laser with and without optical injection from the SFP is shown in Figure 5.29. Strong side mode suppression is shown in the FP with the SFP on. An SMSR of $35\,\mathrm{dB}$ was measured from the OSA trace.

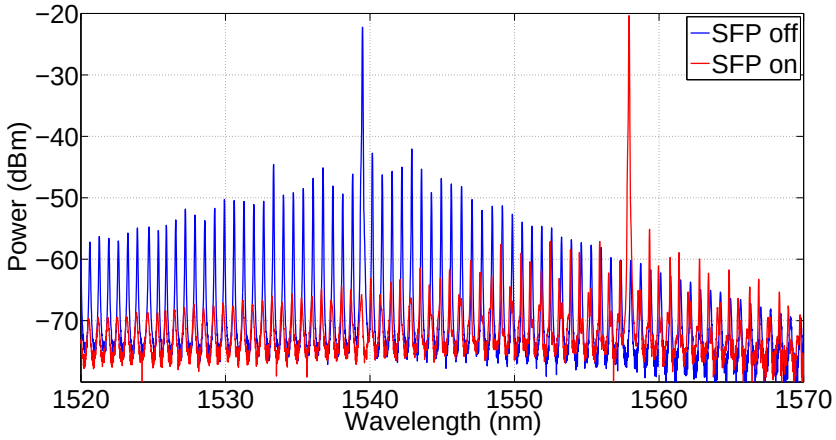

Figure 5.29: Optical spectrum of FP laser with/without injection from the SFP. Spectra were recorded through the angled waveguide section.

The FP laser was gain-switched by applying a $25\,\mathrm{dBm}$, $5\,\mathrm{GHz}$ RF signal via the bias tee, similar to as described in Figure 5.5. The gain section, slotted section, FP laser, and angled waveguide biases were $66\,\mathrm{mA}$, $49\,\mathrm{mA}$, $80\,\mathrm{mA}$, and $21\,\mathrm{mA}$ respectively. The FP laser had higher loss due to using two etched facets to form the cavity, requiring a higher bias level and RF power level. The optical comb spectrum is shown in Figure 5.30.

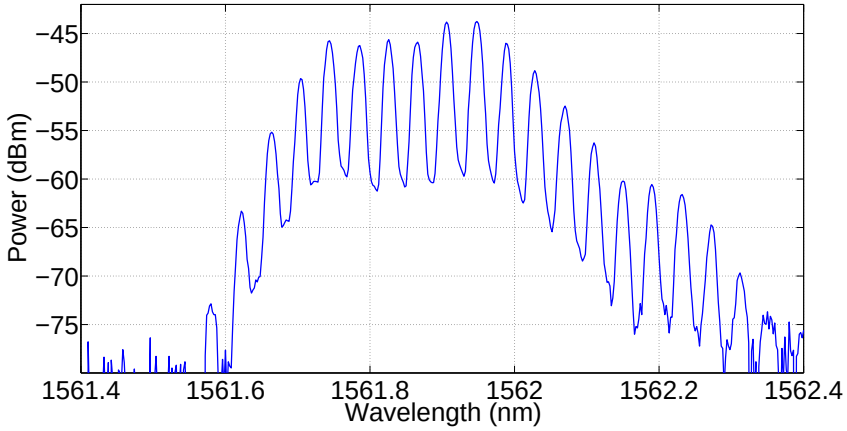

Figure 5.30: Optical comb with 5 GHz line spacing.

Linewidth measurements could not be obtained for this device due to the low optical power. Possible reasons for this low power could be poor coupling of the lensed fibre to the angled waveguide, and/or losses around the bend of the

angled waveguide. The extra etched facet in this device would also contribute to the optical loss.

5.2 Butterfly Packaged Comb Source

A prototype packaged comb source was developed. The package features 7 DC pins, RF SMA connector, and fibre pigtail. Figure 5.31 shows the optical comb source in a prototype package. Such a package has high potential for the future of a superchannel communications system.

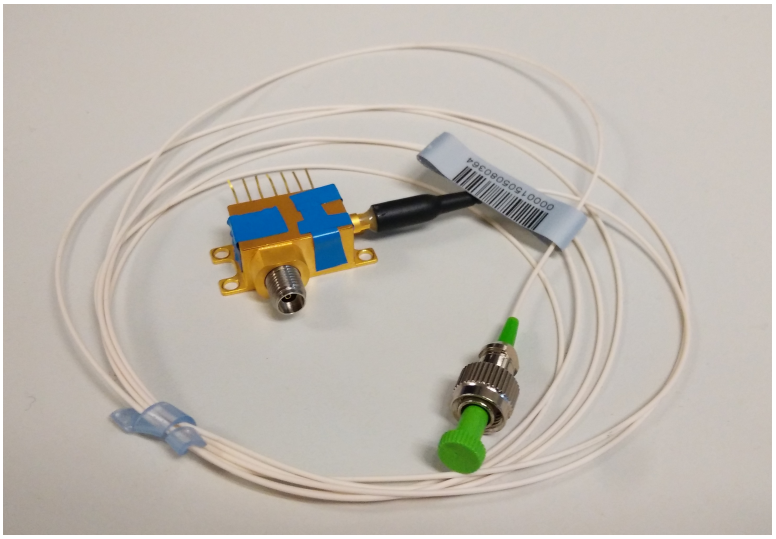

Figure 5.31: Butterfly package for optical comb source, featuring 7 DC pins, RF SMA connector, and fibre pigtail.

5.2.1 Device Design and Fabrication

The device is a two section Slotted Fabry-Pérot (SFP) [104] laser of total length $1350\,\mu\mathrm{m}$ integrated with with a shorter SFP laser of length $680\,\mu\mathrm{m}$. The longer SFP is referred to as the master laser, the shorter SFP the slave. On-chip injection-locking is performed as in [34, 57]. The master SFP has a $600\,\mu\mathrm{m}$ gain section, with a $760\,\mu\mathrm{m}$ slotted mirror section. The mirror section consists of 8 periodically spaced slots, with slot width $0.88\,\mu\mathrm{m}$, period $108\,\mu\mathrm{m}$, and slot depth of $1.7\,\mu\mathrm{m}$. The slave SFP has a $250\,\mu\mathrm{m}$ gain section, and a $430\,\mu\mathrm{m}$ mirror section. The mirror consists of 5 periodically spaced slots with the same slot width, period, and depth as before. The SFPs are coupled via a $15\,\mu\mathrm{m}$ long waveguide section. A schematic of the device is shown in Figure 5.32 with each section labelled. While in Section 5.1.2 it was shown that the shorter SFP

laser in this design did not lase, the device could operate with all sections biased. As such, this device was chosen to trial run the packaging process.

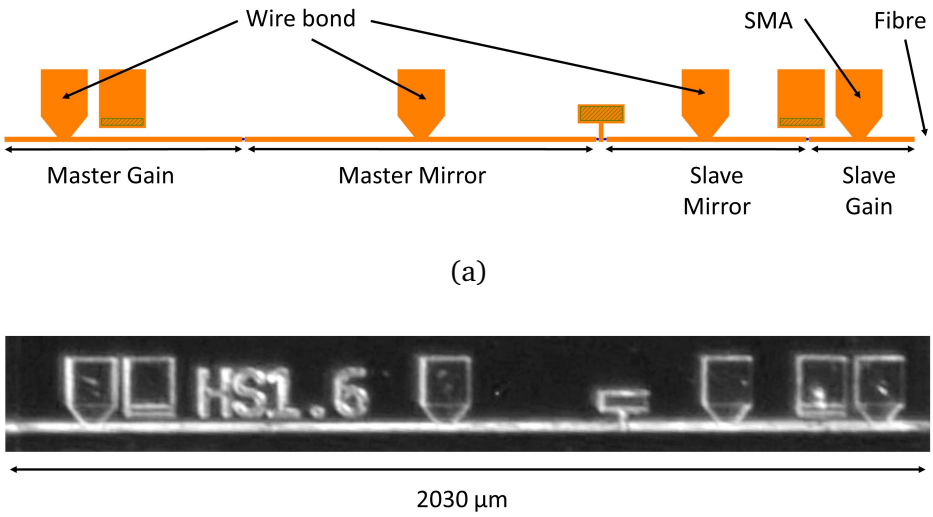

Figure 5.32: (a) Device schematic with sections labelled. Contact pads for the DC pin wire bonds and SMA connector are indicated, as well as the facet used for fibre coupling. (b) Microscope image of device.

The device was packaged in a 7-pin high-speed butterfly package. A thermoelectric cooler (TEC) was included in the package to maintain a stable temperature during operation. Wire-bonds were used to connect the Master Gain, Master Mirror, and Slave Mirror contact pads to DC pins. The Slave Gain contact pad was wire-bonded to a micro-strip line connecting to an RF SMA connector. The SMA connector allows for RF modulation of the Slave Gain section. A fibre pigtail coupled light out of the device from the Slave Gain facet. The lensed optical fibre inside the package is shown in Figure 5.33.

5.2.2 Characterization

The package was mounted on a butterfly mount (Laser 2000, model 203) and was maintained at $20\,^{\circ}\mathrm{C}$ using the TEC. An estimate of the coupling efficiency of the fibre was measured by injecting $0\,\mathrm{dBm}$ of optical power at $1550\,\mathrm{nm}$ into the device. The Slave section was reverse biased at $-2\,\mathrm{V}$ and the total reverse current was recorded. The current generated as a result of absorption (total reverse current minus dark current) was converted to optical power (assuming 1 photon creates 1 electron) giving a coupling efficiency of 43%. Losses can be accounted by mode size mismatch and fibre positioning error.

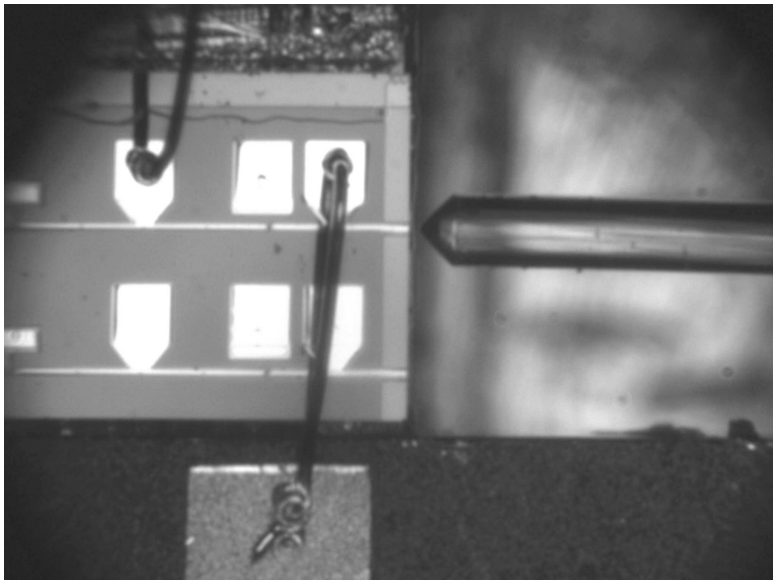

Figure 5.33: Microscope view of inside the butterfly package showing wire-bonds and lensed optical fibre.

DC bias was applied to all four sections of the device, and a bias tee was used to apply simultaneous RF & DC bias to the Slave Gain section. Optical spectra were recorded using an optical spectrum analyser (OSA) with a wavelength resolution of $0.015\,\mathrm{nm}$. DC bias currents of $70\,\mathrm{mA}$, $25\,\mathrm{mA}$, $5\,\mathrm{mA}$, and $40\,\mathrm{mA}$ were applied to the Master Gain, Master Mirror, Slave Mirror, and Slave Gain sections respectively. A $4\,\mathrm{GHz}$ $25\,\mathrm{dBm}$ RF signal was applied to the Slave Gain section. An S_{11} measurement performed with a vector network analyser (VNA) was used to estimate that 36% of the RF power was absorbed by the device. The optical spectrum was recorded and is shown in Figure 5.34. Eight comb lines is shown to be within $3\,\mathrm{dB}$ of each other.

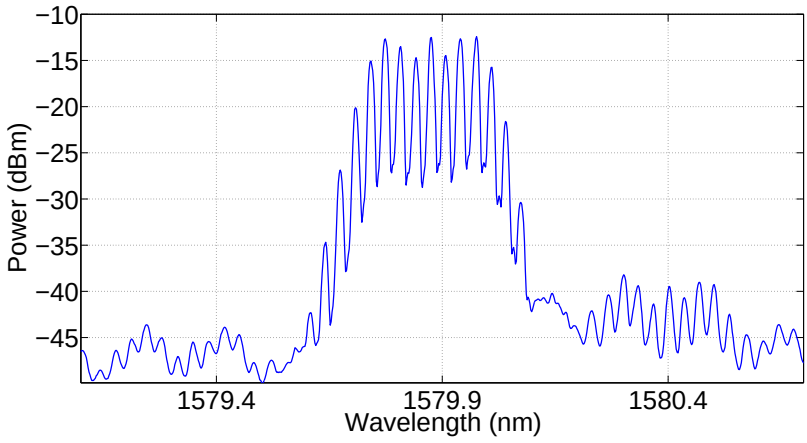

Figure 5.34: $4\,\mathrm{GHz}$ optical comb produced from butterfly packaged device showing 8 comb lines within $3\,\mathrm{dB}$ of each other.

The linewidth of the device was measured using the recirculating delayed self-heterodyne interferometer outlined in Chapter 5, Section 5.1.1.3. The fibre length for the delay was $50\,\mathrm{km}$ giving maximum resolution of $<2\,\mathrm{kHz}$ for the measurement. The resolution bandwidth of the ESA was set to 100 kHz, with a sweep time of $60\,\mathrm{ms}$. The linewidth measurement is shown in Figure 5.35.

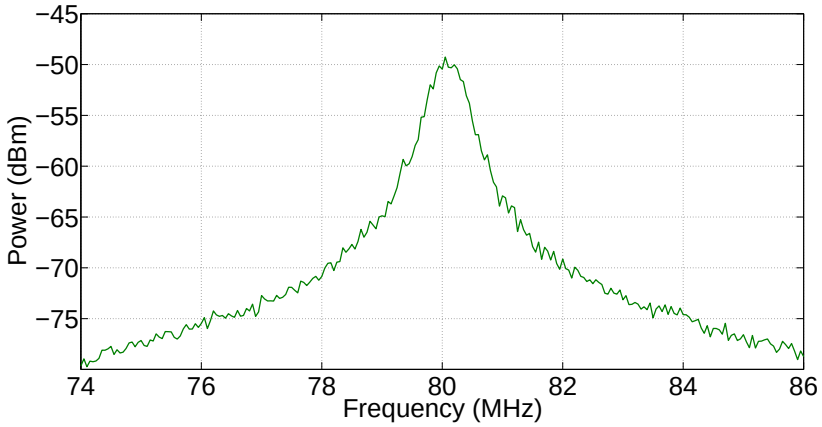

Figure 5.35: Linewidth measurement using the RDSHI method. $50\,\mathrm{km}$ delay fibre was used, along with a $80\,\mathrm{MHz}$ acousto-optic modulator to shift the delayed signal. The full-width half-max is measured as approximately $600\,\mathrm{kHz}$.

The full-width half-max (FWHM) of the measurement in Figure 5.35 is approximately $600\,\mathrm{kHz}$. The linewidth of the device is taken as half the FWHM value as the self-heterodyne beat note is equivalent to twice the laser linewidth, giving a linewidth of $300\,\mathrm{kHz}$.

Thus, a prototype butterfly packaged low-linewidth optical comb source has been demonstrated. The packaged device could be used in systems level experiments involving the modulation of data on to each comb line for the development of AO-OFDM networks.

5.3 Conclusion

In this chapter, several devices were characterised for use as an optical comb source. Modulation bandwidth was analysed using S parameters. A high speed process was employed to reduce RF limits imposed by device impedance for the devices outlined in Sections 5.1.2 and 5.1.3. Further optimizations to the comb source design were performed using the standard fabrication processes as the modulation limit appeared to be mainly from the optical transit time, see Section 5.1.3.

Low linewidth optical combs were successfully generated. An SFP laser was shown to have a higher optical linewidth when gain-switched, see Figure 5.8. Devices which featured on-chip injection-locking showed minimal increase in linewidth, see Figures 5.16 and 5.25. These results agree with the predicted outcome from Chapter 3, where the effect of gain-switching on optical phase noise was modelled.

Achieving spectrally efficient optical communications is imperative to counter the growing demand on the current network infrastructure. Optical comb sources such as the devices presented in this chapter could be used for generation of coherent communications systems. The devices are prime candidates for further photonic integration with splitters and modulators.

As a first step towards the integration of an optical comb source with devices such as splitters and modulators, a facetless optical comb source was designed. This device could produce an optical comb at $5\,\mathrm{GHz}$, see Figure 5.30. Further optimization of this design would be a worthwhile area of research for the development of an integrated AO-OFDM transmitter.

The next logical steps to further this research would be the integration of a comb source with a comb line splitter. Chapter 6 will look into some future work that could be done on this matter, as well as steps which could be taken to reduce the bandwidth limit inherent to laser sources.

Chapter 6

Future Work and Conclusion

In Chapter 5, the experimental results from several optical comb sources were presented. Coherent optical combs were obtained with comb line spacings up to $10\,\mathrm{GHz}$, and linewidths as low as $300\,\mathrm{kHz}$. A prototype packaged optical comb source has been developed to allow for systems level experiments on the comb source for data transmission. In this chapter, information on the next steps of this line of research will be given. The next integration steps are outlined for the development of a monolithically integrated AO-OFDM transmitter. Potential improvements to the comb source are given, primarily in order to boost the laser bandwidth to allow for broader comb line spacing. And finally a summary and conclusion are given for the work presented in this thesis.

6.1 Towards an AO-OFDM Transmitter

In Chapter 5, an optical comb source which did not rely on cleaved facets was demonstrated. This device is readily integrable with further optical components. As the next step towards an AO-OFDM transmitter, this comb source could be integrated with an optical filter, such as the filter used in [70] based on injection-locked lasers. With this filter, a multimode interference coupler (MMI) splits the comb power into separate arms. The comb is then coupled to separate lasers, each of which injection-lock to different comb lines. A schematic is shown in Figure 6.1.

If the comb lines can be successfully demultiplexed, the realization of an optical transmitter based on AO-OFDM becomes a step closer. The integration of a modulator and combiner would follow, such as the electro-absorption modulator (EAM) and star coupler used in [118].

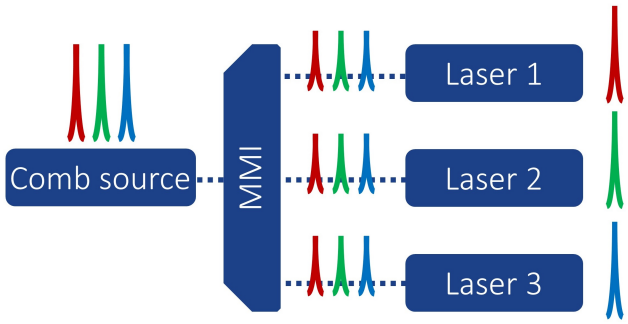

Figure 6.1: Optical comb filter. The optical comb is coupled to three different lasers through a multimode interference coupler (MMI). Each laser then injection-locks to one comb line.

6.2 Future Design Considerations

The simplicity of direct laser modulation to generate optical combs makes gain-switching an attractive technique. The modulation signal is applied directly to the current bias of the laser, without the need for integration of a suitable modulator. Although, by using this method the modulation frequency of the applied signal is limited by the modulation bandwidth of the laser.

The relaxation frequency ω_τ sets an upper limit to the modulation bandwidth of the laser. From Chapter 2, Equation 2.13, the conditions to increase the modulation bandwidth of a laser diode are;

1. Increase the photon density S_0
2. Decrease the photon lifetime τ_p

The photon density can be increased by increasing the current bias of the device, but this can lead to overheating due to the increased optical power. The photon lifetime can be decreased by shortening the cavity length, and by coating the facets in anti-reflection coatings. The threshold current can be reduced by coating the facets with a high reflective coating, although such coatings may not be an option for integrated sources. In general, the best balance between photon density and photon lifetime can be found with short cavities with highly reflective coatings [119].

The fundamental limits on a lasers resonance frequency can be overcome with strong optical injection from an external master laser [50]. Under injection-locking, the resonance frequency of the injected slave laser is

approximately;

$$\omega_{\tau}^2 \approx \omega_{R0}^2 + \Delta\omega_R^2 \tag{6.1}$$

where ω_{R0} is the free running resonance frequency, and $\Delta\omega_R$ is the resonance enhancement [120].

Injected optical power depletes available carriers in the slave cavity, leading to a redshift of the free running laser frequency;

$$\Delta\omega_{shift} = \alpha g_0 \Delta N \tag{6.2}$$

where α is the linewidth enhancement factor (representing carrier induced refractive index change), g_0 is the differential gain, and ΔN is the number of carriers above threshold. The shift in the cavity frequency as a result of optical injection is illustrated in Figure 6.2.

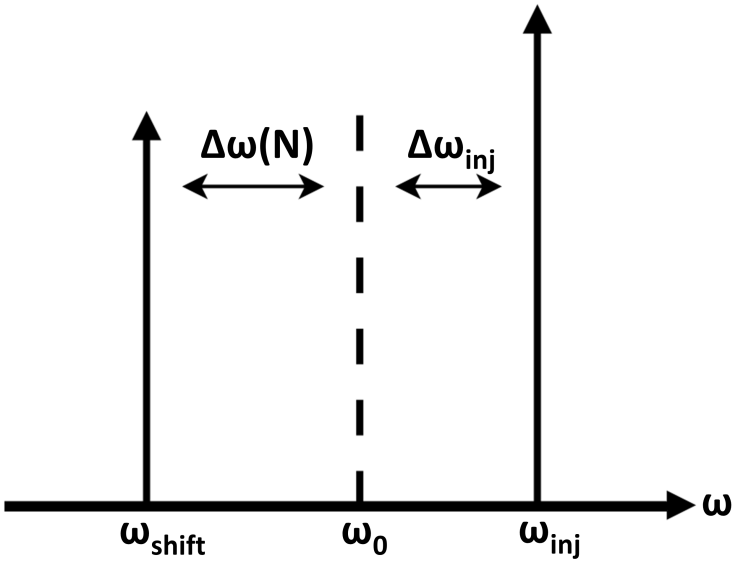

Figure 6.2: Lasing frequency shift as a result of optical injection.

From [99], the resonance enhancement can be attributed to the beat note existing between the injection locked lasing mode, and the shifted cavity mode, $\Delta\omega_R = \omega_{inj} - \omega_{shift}$. From Figure 6.2 and combining with Equation 6.2;

$$\Delta\omega_R = \Delta\omega_{inj} - \alpha g_0 \Delta N \tag{6.3}$$

From Figure 6.2 and Equation 6.3, the maximum resonance enhancement can be achieved by locking the slave laser at the positively detuned edge of its

locking bandwidth. The resonance enhancement can also be defined as [52];

$$\Delta\omega_R = -\kappa\sqrt{R_{int}}\, sin\phi_0 \tag{6.4}$$

where κ is the coupling coefficient ($\nu_g/2L$), R_{int} is the internal injected power ratio from the master to the slave power output, and ϕ_0 is the steady state phase difference between the master and slave fields. R_{int} can be expressed as a function of the external injected power ratio by;

$$\frac{R_{int}}{R_{ext}} = \frac{(1-r)^2}{r} \tag{6.5}$$

Where r is the reflectivity of the injection facet. With $\phi_0 = -\pi/2$ at the positive edge of the locking bandwidth [52], the maximum achievable enhancement is;

$$\Delta\omega_{R,max} = \frac{\nu_g}{2L}\frac{1-r}{\sqrt{r}}\sqrt{R_{ext}} \tag{6.6}$$

$$Q_C = \frac{\omega_0 L}{\nu_g}\frac{\sqrt{r}}{1-r} \tag{6.7}$$

$$\Delta\omega_{R,max} = \frac{\omega_0}{2Q_C}\sqrt{R_{ext}} \tag{6.8}$$

where Q_C is the coupling quality factor, and ω_0 is the laser frequency.

To maximise the resonance enhancement achievable through injection-locking, we require;

1. High injection power from the master, low output power from the slave (maximise R_{ext})
2. Low reflectivity from the slaves injection facet (minimise Q_C)
3. Large mode spacing in the slave laser (reduce possibility of locking adjacent modes)

From the above analysis, the next step in this research could be the integration of two single mode lasers in such a way that the detuning between the wavelengths can be controlled [121]. A device based on the slotted Fabry-Pérot lasers used throughout this thesis, could be designed as depicted in Figure 6.3.

The device pictured integrates two slotted Fabry-Pérot lasers. The SFPs are coupled via an etched facet on the gain section, through a coupling section.

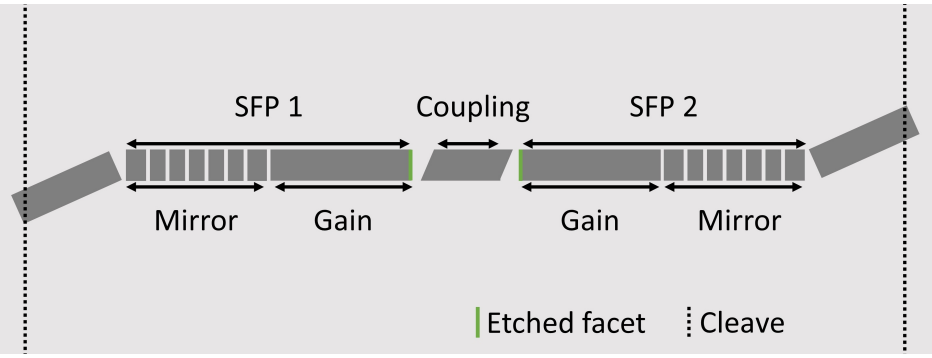

Figure 6.3: Design proposition. Two SFP lasers integrated on a single chip, coupled via etched facets through a coupling section to control coupling strength. Angled waveguides coupling light from the mirror sections of the SFPs to the chip edge.

The coupling section would allow for control of the coupling strength. The device would require a high-speed process fabrication to reduce capacitance so as to measure resonance enhancement beyond $5 - 10\,\mathrm{GHz}$. By eliminating the RC limit with a high speed process, and by increasing the inherent speed of the laser using injection-locking, the resulting device would operate at higher frequencies and therefore produce more comb lines.

6.3 Summary and Conclusion

Optical communications have made a massive impact on the modern world. Day to day interactions through social media and online gaming have changed the social structure in ways never thought possible. The technology upon which the fibre communications network is based is struggling to keep up with the growing user base, and that base's hunger for bandwidth. To satiate this growth, new methods of data transmission devices need to be developed. AO-OFDM is a possibility for increasing bandwidth by improving spectral efficiency. Coherent, low-linewidth optical comb sources are required for this method.

In this thesis, a few methods of comb generation were outlined in Chapter 2. Gain-switching was selected as the method of choice for this work, due to its tunable comb line spacing, and relatively simplistic design and implementation. A theoretical investigation was performed into the noise properties of a gain-switched laser in Chapter 3. The semiconductor rate equations were used to perform this analysis, solving the equations in Matlab. While the phase noise of a laser was found to significantly increase while gain-switched, optical injection from a low-linewidth master laser was shown to solve this issue.

Chapters 4 and 5 dealt with device design and characterization. The building blocks required to integrate devices, such as etched facets and shallow slots, were characterised in Chapter 4. The optical comb sources designed, and incrementally improved, were characterised in Chapter 5. Emission spectra of low-linewidth optical combs were measured. Comb linewidths on the order of $300\,\mathrm{kHz}$ were achieved, with comb line spacings up to $10\,\mathrm{GHz}$. A prototype butterfly packaged optical comb source was demonstrated, for use in systems level experiments.

In Chapter 6, the future of this work was outlined. The next photonic integration steps were discussed for the purpose of developing an AO-OFDM photonic integrated circuit transmitter. Some future comb source design suggestions were made, in order to improve the laser bandwidth to obtain broader comb line spacings.

This thesis has developed coherent, low-linewidth optical comb sources which are a key component for an AO-OFDM transmission system. The comb source design is an integrated pair of lasers, monolithically integrated in a regrowth-free process, making this a low cost method for the generation of optical combs.

Appendix A

Material

Table A.1: Specifications for the material purchased from the company IQE.

Layer	Material	#	x Start	x Finish	y	Dopant	Thickness (μm)
16	GaIn(x)As		0.530			Zinc	0.2000
15	GaIn(x)As(y)P		0.710		0.620	Zinc	0.0500
14	InP					Zinc	0.1000
13	InP					Zinc	1.5000
12	GaIn(x)As(y)P		0.850		0.330	Zinc	0.0200
11	InP					Zinc	0.0500
10	[Al(x)Ga]In(y)As		0.900		0.530	Zinc	0.0600
9	[Al(x)Ga]In(y)As		0.720	0.900	0.530	Undoped	0.0600
8	[Al(x)Ga]In(y)As		0.440		0.490	Undoped	0.0100
7	[Al(x)Ga]In(y)As	5	0.240		0.710	Undoped	0.0060
6	[Al(x)Ga]In(y)As	5	0.440		0.490	Undoped	0.0100
5	[Al(x)Ga]In(y)As		0.900	0.720	0.530	Undoped	0.0600
4	[Al(x)Ga]In(y)As		0.900		0.530	Silicon	0.0600
3	[Al(x)Ga]In(y)As		0.860	0.900	0.530	Silicon	0.0100
2	InP					Silicon	0.5000
1	InP					Silicon	0.300

Appendix B

Matlab Code

B.1 Rate Equation ODE Function

The following code is the function called to solve the rate equations.

```
function dydt = J_rate_eqns(t,y, I2, t1, t2, mod, mod_on,...
    nsteps, Length, N0, a, beta, V, tau_p, Bsim)
dydt = zeros(size(y));

N = y(1);
S = y(2);
Phi = y(3);

A = 1e9; %non radiative recombination
B = 1e-16; %bimoleculare recombination coef
C = 1e-41; %auger recombination coef
alpha = 4; %linewidth enhancement factor
T = 0.3; %confinement factor

R = A*N + B*N*N + C*N*N*N; % carrier recombination rate
G = a*(N-N0); % Gain
tp = 1/tau_p;
e = 1.6e-19; % charge of electron

%%% Gausian random variable
xis=randn;
xin=randn;
xi=randn;
%%%
%Noise terms
Dnn = sqrt((2*R*Bsim))*(xin);
```

```
Dss = sqrt((beta*2*S*B*N*N*Bsim))*(xis);
Dpp = sqrt((beta*S*B*N*N*Bsim*0.5))*xi;

I = (I2)+(50e-3)*cos(2*pi*(mod*1e9)*t)*mod_on;
if I ≤ 0
    I = 0;
end

dydt(1) = I/(e*V) - R - G*S + Dnn - Dss;
dydt(2) = (T*G-tp)*S + beta*B*N*N+ Dss;
dydt(3) = 0.5*T*alpha*a*(N-N0)+ (1/S)*Dpp;
```

B.2 Rate Equation ODE Main File

This code calls the ODE function to solve the rate equations for the given parameters, plotting the carrier density, photon density, and frequency noise spectrum.

```
clear all

%%%%%%%%%% Set parameters %%%%%%%%%%%%%%%%%%%%%%%%
RW = 2.5e-6; % Ridge width
QW_thick = 0.03e-6; % quantum well region thickness
Length = 500e-6; % length of cavity
vg = 8.5e7; %group velocity // group index 3.5
T = 0.3; %confinement factor
R1 = 0.3; R2 = 0.3; %Mirror reflectivity

Aeff = RW*QW_thick*T; %effective model area
V = RW*QW_thick*Length; %volume of active region
tau_p = Length/(vg*log(1/sqrt(R1*R2))); % photon lifetime

v = 200e12; %laser emission frequency 200THz
K =0.3; % ratio of photons that exit the laser
h = 6.62e-34; %planks constant
N0 = 1e24; %carrier density at transparancy
a = 8e-13; %differential gain
alpha = 4; %linewidth enhancement factor
beta = 1e-6; %fraction of spont emission into lasing mode
B = 1e-16; %bimoleculare recombination coef

mod = 5; %modulation rate in GHz
```

```
mod_on = 0; % 1: gain switching on, 0: gain-switching off

t1 = 100e-9;          %%%%% Start time
t2 = 150e-9;         %%%%% Stop time

dt = 5e-12; %time increment
nsteps = (t2-t1)/(dt) +1;  %number of steps
tspan = linspace(t1,t2,nsteps); %span of time values
Bsim =  1/dt; %simulation bandwidth

%%%%%%%%%%% Initial Conditions %%%%%%%%%%%
Ni = N0; %intial carrier density
Si = 1e20; %intial photon density
Pi = 1; % intial phase
%%%%%%%%%%%%%%%%%%%%%%%%%%%%%%%%%%%%%%%%%%%
 for j=1:1:5 %  loop averages results 5 times
    I2 = 50e-3; %current in A
    %solve ODEs giving extra parameters
    [t,y] = ode45(@(t,y) J_rate_eqns(t,y, I2, t1, t2, mod, mod_on,...
    nsteps, Length, N0, a, beta, V, tau_p, Bsim), [tspan], [Ni Si Pi]);
    D = length(y); %getting length of N, S, P, solution matrix
    d_phi = zeros(D,1);
    del_v = zeros(D,1);
    for i=1:1:D
    xi=randn;
    P(i) = vg*Aeff*h*v*K*(y(i,2)); %convert photon number to Power W
    d_phi(i) = 0.5*T*alpha*a*(y(i,1)-N0)...
        + (1/y(i,2))*sqrt((beta*y(i,2)*B*y(i,1)*y(i,1)*Bsim*0.5))*xi;
    del_v(i) = d_phi(i)/(2*pi); %instantaneous frequency change
    end

disp(j)
%%%%%% Fourier transform to calculate FN spectrum %%%%%%%%
start_fluff = 2000;% Remove first 2000 data points, relaxation oscilations
N = length(t)- start_fluff;
bin_vals = [0:N]; df=1/(dt);% sampling freqeuncy
fax_Hz = bin_vals*df/N; N_2 = ceil(N/2);

FFT1 = 2.*abs(fft((del_v(start_fluff+1:end))))*dt;% mulitply by 2 as
                                                 % looking at one sided spectrum.
FFT1(1)=FFT1(1)/2;% half first value as occurs once in two sided spectrum
FFT1(N_2)=FFT1(N_2)/2;
FN = (1/(t2-t(start_fluff+1)))*(FFT1.^2);
ff = fax_Hz(1:N_2); pp = FN(1:N_2);
%%%% Average FN spectrum %%%%
```

```
        if j==1
            New = pp;
            temp = New;
        else
            New = (pp + temp)./2;
            temp = New;
        end
 end
%%%%%%%%%%%%%%%% Plot carrier density %%%%%%%%%%%%%%%%%%%%%%%%
figure(1)
plot(t, y(:,1) ,'LineWidth',2)
grid on
set(gcf,'color','w');
xlabel('Time (s)','Fontsize',40,'color','black');
ylabel('Carrier density (m^{-3}) ','Fontsize',40,'color','black');
set(gca,'Fontsize',40)
Q=get(gca,'ytick');
set(gca,'ytick',Q(2:end))

%%%%%%%%%%%%%%%% Plot photon density %%%%%%%%%%%%%%%%%%%%%%%%
figure(2)
plot(t, y(:,2) ,'LineWidth',2)
grid on
set(gcf,'color','w');
xlabel('Time (s)','Fontsize',40,'color','black');
ylabel('Photon density (m^{-3}) ','Fontsize',40,'color','black');
set(gca,'Fontsize',40)
Q=get(gca,'ytick');
set(gca,'ytick',Q(2:end))

%%%%%%%%%%%%%%%% Plot FN spectrum %%%%%%%%%%%%%%%%%%%%%%%%
figure(3)
%smoo2 = smooth(ff, New,0.004,'rloess'); % smoothing function for New
loglog(ff, New ,'LineWidth',2)
grid on
set(gcf,'color','w');
xlabel('Freqeuncy (Hz)','Fontsize',40,'color','black');
ylabel('FN (Hz) ','Fontsize',40,'color','black');
set(gca,'Fontsize',40)
Q=get(gca,'ytick');
set(gca,'ytick',Q(2:end))

%%%%%% save photon density, carrier density, and phase of laser for use
%%%%%% as master laser in injection-locked equations %%%%%
Sm = y(:,2);
```

```
Phim = y(:,3);
tm = t;
%%%%%%%%%%%%%%%%%%%%%%%%%%%%%%%%%%%%%%%%%%%%%%%%%%%%%%%%%%%%%%%%%%%%%%%%%%%%
```

B.3 Injection-Locked Rate Equation ODE Function

The function below is called to solve the injection-locked rate equations.

```
function dydt = INJ_rate_eqns(t,y,I2, t1, t2, mod, mod_on, nsteps,...
   Length, N0, a, beta, Kinj, del_w, Sm, Phim, tm, Scaling, V, tau_p, Bsim)
dydt = zeros(size(y));

N = y(1);
S = y(2);
Phi = y(3);

A = 1e9; %non radiative recombination
B = 1e-16; %bimoleculare recombination coef
C = 1e-41; %auger recombination coef
alpha = 4; %linewidth enhancement factor - 2.5 for InGaAlAs QWs
T = 0.3; %confinement factor

R = A*N + B*N*N + C*N*N*N; % carrier recombination rate
G = a*(N-N0); % Gain
tp = 1/tau_p;
e = 1.6e-19; % charge of electron

%%% Gausian random variable
xis=randn;
xin=randn;
xi=randn;
%%%
%Noise terms
Dnn = sqrt((2*R*Bsim))*(xin);
Dss = sqrt((beta*2*S*B*N*N*Bsim))*(xis);
Dpp = sqrt((beta*S*B*N*N*Bsim*0.5))*xi;
Smm = interp1(tm, Sm, t); % Interpolate the data set
Phimm = interp1(tm, Phim, t); % Interpolate the data set
I = (I2)+(50e-3)*cos(2*pi*(mod*1e9)*t)*mod_on;
if I <= 0
    I = 0;
end

```

```
dydt(1) = I/(e*V) - R - G*S + Dnn - Dss;
dydt(2) = (T*G-tp)*S + beta*B*N*N...
    + 2*Kinj*sqrt(Scaling*Smm.*S).*cos(Phi-Phimm)+ Dss;
dydt(3) = 0.5*T*alpha*a*(N-N0)...
    - Kinj*sqrt(Scaling*Smm./S).*sin(Phi-Phimm) - del_w + (1/S)*Dpp;
```

B.4 Injection-Locked Rate Equation ODE Main File

This code calls the ODE function to solve the injection-locked rate equations for the given parameters, plotting the carrier density, photon density, and frequency noise spectrum. The standard rate equation solver must be run first to generate the injected master laser signal,

```
clearvars -except Phim Sm tm

%%%%%%%%%% Set parameters %%%%%%%%%%%%%%%%%%%%%%%%
RW = 2.5e-6; % Ridge width
QW_thick = 0.03e-6; % quantum well region thickness
Length = 500e-6; % length of cavity
vg = 8.5e7; %group velocity // group index 3.5
T = 0.3; %confinement factor
R1 = 0.3; R2 = 0.3; %Mirror reflectivity

Aeff = RW*QW_thick*T; %effective model area
V = RW*QW_thick*Length; %volume of active region
tau_p = Length/(vg*log(1/sqrt(R1*R2))); % photon lifetime

v = 200e12; % laser emission frequency 200THz
K =0.3; % ratio of photons that exit the laser
h = 6.62e-34; %planks constant
N0 = 1e24;% carrier density at transparancy
a = 8e-13; % differential gain
alpha = 4; % linewidth enhancement factor
beta = 1e-4; % fraction of spont emission into lasing mode
B = 1e-16; % bimoleculare recombination coef

mod = 2; % modulation rate in GHz
mod_on = 0; % 1: gain switching on, 0: gain-switching off
Inj = 0; % 1: injection-locking on, 0: injection-locking off

t1 = 100e-9;          %%%%% Start time
t2 = 150e-9;         %%%%% Stop time
```

```
30
31 dt = 5e-12; %time increment
32 nsteps = (t2-t1)/(dt) +1;  %number of steps
33 tspan = linspace(t1,t2,nsteps); %span of time values
34 Bsim =  1/dt; %simulation bandwidth
35
36 Kinj = Inj*vg/(2*Length);% coupling rate
37
38 %%%%%%%%%%%% Initial Conditions %%%%%%%%%%%%
39 Ni = N0; %intial carrier density
40 Si = 1e20; %intial photon density
41 Pi = 1; % intial phase
42 %%%%%%%%%%%%%%%%%%%%%%%%%%%%%%%%%%%%%%%%%%%
43 del_w = +Inj*2*pi*0e9; % detuning of injected laser frequency
44 Scaling = 10; % scale injected optical power
45 %%%%%%%%%%%%%%%%%%%%%%%%%%%%%%%%%%%%%%%%%%%
46  for j=1:1:5 %  loop averages results 5 times
47     I2 = 50e-3; %current in A
48     [t,y] = ode45(@(t,y) INJ_rate_eqns(t,y,I2, t1, t2, mod, mod_on,...
49         nsteps, Length, N0, a, beta,...
50         Kinj, del_w, Sm, Phim, tm, Scaling, V, tau_p, Bsim),...
51         tspan, [Ni Si Pi]); %solve ODEs giving I as a parameter
52     D = length(y); %getting size of N, S, P, solution matrix
53     d_phi = zeros(D,1);
54     del_v = zeros(D,1);
55     for i=1:1:D
56         xi=randn;
57     d_phi(i) = 0.5*T*alpha*a*(y(i,1)-N0)...
58       - Kinj*sqrt(Scaling*Sm(i)./y(i,2)).*sin(y(i,3)-Phim(i))...
59       - del_w + (1/y(i,2))*sqrt((beta*y(i,2)*B*y(i,1)*y(i,1)*Bsim*0.5))*xi;
60     del_v(i) = d_phi(i)/(2*pi);
61     end
62 disp(j)
63
64 %%%%%% Fourier transform to calculate FN spectrum %%%%%%%%%
65 start_fluff = 2000;% Remove first 2000 data points, relaxation oscilations
66 N = length(t)- start_fluff;
67 bin_vals = [0:N]; df=1/(dt);% sampling freqeuncy
68 fax_Hz = bin_vals*df/N; N_2 = ceil(N/2);
69
70 FFT1 = 2.*abs(fft((del_v(start_fluff+1:end))))*dt;  %mulitply by 2
71                                          % as looking at one sided spectrum
72 FFT1(1)=FFT1(1)/2; % half first value as occurs once in two sided spectrum
73 FFT1(N_2)=FFT1(N_2)/2;  FN = (1/(t2-t(start_fluff+1)))*(FFT1.^2);
74 ff = fax_Hz(1:N_2); pp = FN(1:N_2);
```

```
%%%% Average FN spectrum %%%%
        if j==1
            New = pp;
            temp = New;
        else
            New = (pp + temp)./2;
            temp = New;
        end
 end
%%%%%%%%%%%%%%%% Plot carrier density %%%%%%%%%%%%%%%%%%%%%%%%
figure(1)
plot(t, y(:,1) ,'LineWidth',2)
grid on
set(gcf,'color','w');
xlabel('Time (s)','Fontsize',40,'color','black');
ylabel('Carrier density (m^{-3}) ','Fontsize',40,'color','black');
set(gca,'Fontsize',40)
Q=get(gca,'ytick');
set(gca,'ytick',Q(2:end))

%%%%%%%%%%%%%%%% Plot photon density %%%%%%%%%%%%%%%%%%%%%%%%
figure(2)
plot(t, y(:,2) ,'LineWidth',2)
grid on
set(gcf,'color','w');
xlabel('Time (s)','Fontsize',40,'color','black');
ylabel('Photon density (m^{-3}) ','Fontsize',40,'color','black');
set(gca,'Fontsize',40)
Q=get(gca,'ytick');
set(gca,'ytick',Q(2:end))

%%%%%%%%%%%%%%%% Plot FN spectrum %%%%%%%%%%%%%%%%%%%%%%%%
figure(3)
%smoo2 = smooth(ff, New,0.004,'rloess'); % smoothing function for New
loglog(ff, New ,'LineWidth',2)
grid on
set(gcf,'color','w');
xlabel('Freqeuncy (Hz)','Fontsize',40,'color','black');
ylabel('FN (Hz) ','Fontsize',40,'color','black');
set(gca,'Fontsize',40)
Q=get(gca,'ytick');
set(gca,'ytick',Q(2:end))
```

References

[1] T. H. Maiman, "Stimulated Optical Radiation in Ruby," *Nature*, vol. 187, no. 4736, pp. 493–494, 1960.

[2] S. Buzzelli, B. Catania, D. Gagliardi, and F. Tosco, "Optical Fibre Field Experiments in Italy: COS1, COS2, and COS3/FOSTER," *Invited paper, International Conference on Communication – ICC '80, Seattle, WA*, vol. 3, pp. 38.9.1–5, 1980.

[3] D. B. Keck, "Optical fiber spans 30 years," *Lightwave*, vol. 17, no. 8, pp. 78–82, 2000.

[4] "http://www.internetlivestats.com/internet-users/," *accessed 14 July 2017*.

[5] J. Murphy and M. Roser, "Internet," *Published online at OurWorldInData.org, https://ourworldindata.org/internet/*, 2017.

[6] Cisco, "Cisco Visual Networking Index: Forecast and Methodology, 2014-2019," *White paper*, 2016.

[7] G. E. Keiser, "A Review of WDM Technology and Applications," *Optical Fiber Technology*, vol. 5, no. 1, pp. 3–39, 1999.

[8] J. Binder and U. Kohn, "10 Gbit/s-Dispersion Optimized Transmission at 1.55 μm Wavelength on Standard Single Mode Fiber," *IEEE Photonics Technology Letters*, vol. 6, no. 4, pp. 558–560, 1994.

[9] Fujitsu, "The path to 100G," *White paper*, 2011.

[10] P. Winzer, G. Raybon, and M. Duelk, "107-Gb/s optical ETDM transmitter for 100G Ethernet transport," in *31st European Conference on Optical Communications (ECOC 2005)*, 2005.

[11] P. Winzer, "Beyond 100G ethernet," *IEEE Communications Magazine*, vol. 48, no. 7, pp. 26–30, 2010.

[12] T. Pfau, S. Hoffmann, and R. Noé, "Hardware-Efficient Coherent Digital Receiver Concept With Feedforward Carrier Recovery for M-QAM Constellations," *Journal of Lightwave Technology*, vol. 27, no. 8, pp. 989–999, 2009.

[13] Infinera, "Super-Channels : DWDM Transmission at 100Gb / s and Beyond," *White Paper*, vol. WP-SC-10-2, no. 1, pp. 1–13, 2012.

[14] H. Ishio, J. Minowa, and K. Nosu, "Review and status of wavelength-division-multiplexing technology and its application," *Journal of Lightwave Technology*, vol. 2, no. 4, pp. 448–463, 1984.

[15] N. S. Bergano, S. M. Ieee, and C. R. Davidson, "Wavelength Division Multiplexing in Long-Haul Transmission Systems," vol. 14, no. 6, pp. 1299–1308, 1996.

[16] ITU-T, "G.694.1 (02/2012), Spectral grids for WDM applications: DWDM frequency grid," *Series G.694.1*, pp. 1–16, 2012.

[17] R. Mears, L. Reekie, I. Jauncey, and D. N. Payne, "Low-noise erbium-doped fibre amplifier operating at 1.54μm," *Electronics Letters*, vol. 23, no. 19, p. 1026, 1987.

[18] R.-J. Essiambre, G. Kramer, P. J. Winzer, G. J. Foschini, and B. Goebel, "Capacity Limits of Optical Fiber Networks," *Journal of Lightwave Technology*, vol. 28, no. 4, pp. 662–701, 2010.

[19] R. Nagarajan, M. Kato, D. Lambert, P. Evans, S. Corzine, V. Lal, J. Rahn, A. Nilsson, M. Fisher, M. Kuntz, J. Pleumeekers, A. Dentai, H.-S. Tsai, D. Krause, H. Sun, K.-T. Wu, M. Ziari, T. Butrie, M. Reffle, M. Mitchell, F. Kish, and D. Welch, "Terabit/s class InP photonic integrated circuits," *Semiconductor Science and Technology*, vol. 27, no. 9, p. 094003, 2012.

[20] A. Ellis and F. Gunning, "Spectral density enhancement using coherent WDM," *IEEE Photonics Technology Letters*, vol. 17, no. 2, pp. 504–506, 2005.

[21] K. Nosu, H. Toba, and K. Iwashita, "Optical OFDM Transmission Technique," *Journal of Lightwave Technology*, vol. L, no. 9, pp. 1301–1308, 1987.

[22] W. Shieh and I. Djordjevic, "OFDM for Optical Communications," vol. 27, no. 3, p. 456, 2009.

[23] G. Boudreau, J. Panicker, N. Guo, R. Chang, N. Wang, and S. Vrzic, "Interference coordination and cancellation for 4G networks," *IEEE Communications Magazine*, vol. 47, no. 4, pp. 74–81, 2009.

[24] P. Delfyett, S. Gee, Myoung-Taek Choi, H. Izadpanah, Wangkuen Lee, S. Ozharar, F. Quinlan, and T. Yilmaz, "Optical frequency combs from semiconductor lasers and applications in ultrawideband signal processing and communications," *Journal of Lightwave Technology*, vol. 24, no. 7, pp. 2701–2719, 2006.

[25] V. Torres-Company and A. M. Weiner, "Optical frequency comb technology for ultra-broadband radio-frequency photonics," *Laser & Photonics Reviews*, vol. 8, no. 3, pp. 368–393, 2014.

[26] I. Coddington, W. Swann, and N. Newbury, "Coherent Multiheterodyne Spectroscopy Using Stabilized Optical Frequency Combs," *Physical Review Letters*, vol. 100, no. 1, p. 013902, 2008.

[27] X. Wang, S. Takahashi, K. Takamasu, and H. Matsumoto, "Space position measurement using long-path heterodyne interferometer with optical frequency comb," *Optics Express*, vol. 20, no. 3, pp. 2725–2732, 2012.

[28] T. Healy, F. C. Garcia Gunning, A. D. Ellis, and J. D. Bull, "Multi-wavelength source using low drive-voltage amplitude modulators for optical communications," *Optics Express*, vol. 15, no. 6, pp. 2981–2986, 2007.

[29] I. Tomkos, S. Azodolmolky, J. Sole-Pareta, D. Careglio, and E. Palkopoulou, "A tutorial on the flexible optical networking paradigm: State of the art, trends, and research challenges," *Proceedings of the IEEE*, vol. 102, no. 9, pp. 1317–1337, 2014.

[30] R. Zhou, S. Latkowski, J. O'Carroll, R. Phelan, L. P. Barry, and P. Anandarajah, "40nm Wavelength Tunable Gain-Switched Optical Comb Source," *2011 37th European Conference and Exhibition on Optical Communication*, vol. 19, no. 26, pp. 1–3, 2011.

[31] C. C. Renaud, M. Pantouvaki, S. Gregoire, I. Lealman, P. Cannard, S. Cole, R. Moore, R. Gwilliam, and A. J. Seeds, "A Monolithic MQW

InP–InGaAsP-Based Optical Comb Generator," *IEEE Journal of Quantum Electronics*, vol. 43, pp. 998–1005, nov 2007.

[32] Z. Liu, Y. Chen, Z. Li, B. Kelly, R. Phelan, J. O. Carroll, T. Bradley, J. P. Wooler, N. V. Wheeler, A. M. Heidt, T. Richter, S. Member, C. Schubert, M. Becker, F. Poletti, M. N. Petrovich, S. Member, S.-u. Alam, S. Member, and D. J. Richardson, "High-Capacity Directly Modulated Optical Transmitter for 2-μm Spectral Region," *Journal of Lightwave Technology*, vol. 33, no. 7, pp. 1373–1379, 2015.

[33] R. Zhou, P. M. Anandarajah, D. G. Pascual, J. O Carroll, R. Phelan, B. Kelly, and L. P. Barry, "Monolithically Integrated 2-Section Lasers for Injection Locked Gain Switched Comb Generation," *Optical Fiber Communication Conference/National Fiber Optic Engineers Conference 2013*, vol. 1, pp. 1–3, 2014.

[34] J. K. Alexander, P. E. Morrissey, H. Yang, M. Yang, P. J. Marraccini, B. Corbett, and F. H. Peters, "Monolithically integrated low linewidth comb source using gain switched slotted Fabry-Perot lasers," *Optics Express*, vol. 24, no. 8, p. 7960, 2016.

[35] P. Stolarz, C. N. Ironside, M. Sorel, and C. Bryce, "High temperature and wide range 40-GHz passive mode-ocking operation of an AlGaInAs 1.55-μm strained quantum well laser," *LEOS 2008 - 21st Annual Meeting of the IEEE Lasers and Electro-Optics Society*, pp. 679–680, 2008.

[36] S. Matsuo, H. Ishii, T. Sato, R. Sato, K. Kasaya, a. Ohki, Y. Shibata, and H. Oohashi, "Monolithically integrated tunable DFB laser array and Mach-Zehnder modulator," *36th European Conference and Exhibition on Optical Communication*, pp. 1–3, 2010.

[37] H. Ito, H. Yokoyama, S. Murata, and H. Inaba, "Picosecond optical pulse generation from an r.f. modulated AlGaAs d.h. diode laser," *Electronics Letters*, vol. 15, no. 23, p. 738, 1979.

[38] S. Tarucha and K. Otsuka, "Response of semiconductor laser to deep sinusoidal injection current modulation," *IEEE Journal of Quantum Electronics*, vol. 17, no. 5, pp. 810–816, 1981.

[39] P. J. Winzer and R.-J. Essiambre, *Advanced optical modulation formats*, vol. 94. 2006.

[40] A. D. Ellis, "The nonlinear Shannon limit and the need for new fibres," in *SPIE* (B. J. Eggleton, A. L. Gaeta, and N. G. Broderick, eds.), vol. 8434, p. 84340H, jun 2012.

[41] L. P. Barry, P. Anandarajah, and A. Kaszubowska, "Optical pulse generation at frequencies up to 20 GHz using external-injection seeding of a gain-switched commercial Fabry-Perot laser," *IEEE Photonics Technology Letters*, vol. 13, no. 9, pp. 1014–1016, 2001.

[42] P. M. Anandarajah, R. Maher, Y. Q. Xu, S. Latkowski, J. O'Carroll, S. G. Murdoch, R. Phelan, J. O'Gorman, and L. P. Barry, "Generation of coherent multicarrier signals by gain switching of discrete mode lasers," *IEEE Photonics Journal*, vol. 3, no. 1, pp. 112–122, 2011.

[43] M. G. Pascual, P. M. Anandarajah, R. Zhou, F. Smyth, S. Latkowski, and L. P. Barry, "Cascaded Fabry-Perot lasers for coherent expansion of wavelength tunable gain switched comb," in *Optical Communication (ECOC), 2014 European Conference on*, no. August 2015, pp. 1–3, 2014.

[44] J. Alexander, P. Morrissey, H. Yang, M. Yang, Y. Zhao, M. Rensing, P. O'Brien, and F. Peters, "Butterfly packaged low-linewidth optical comb source," *Electronics Letters*, vol. 53, no. 9, pp. 615–616, 2017.

[45] P. M. Anandarajah, S. P. O. Duill, Rui Zhou, and L. P. Barry, "Enhanced Optical Comb Generation by Gain-Switching a Single-Mode Semiconductor Laser Close to Its Relaxation Oscillation Frequency," *IEEE Journal of Selected Topics in Quantum Electronics*, vol. 21, pp. 592–600, nov 2015.

[46] S. Mohidiek, H. Burkhard, and H. Walter, "Chirp reduction of directly modulated semiconductor lasers at 10 Gb/ s by strong CW light injection," *Journal of Lightwave Technology*, vol. 12, no. 3, pp. 418–424, 1994.

[47] J. Peña Ramirez, L. A. Olvera, H. Nijmeijer, and J. Alvarez, "The sympathy of two pendulum clocks: beyond Huygens' observations," *Scientific Reports*, vol. 6, no. March, p. 23580, 2016.

[48] R. Pantell, "The laser oscillator with an external signal," *Proceedings of the IEEE*, vol. 53, no. 5, pp. 474–477, 1965.

[49] W. H. Steier and H. L. Stover, "Locking of Laser Oscillators by Light Injection," *IEEE Journal of Quantum Electronics*, vol. 2, no. 4, pp. 111–112, 1966.

[50] J. Wang, M. K. Haldar, S. Member, L. Li, and F. V. C. Mendis, "Enhancement of Modulation Bandwidth of Laser Diodes by Injection Locking," *Technology*, vol. 8, no. 1, pp. 34–36, 1996.

[51] V. Annovazzi-Lodi, A. Sciré, M. Sorel, and S. Donati, "Dynamic behavior and locking of a semiconductor laser subjected to external injection," *IEEE Journal of Quantum Electronics*, vol. 34, no. 12, pp. 2350–2356, 1998.

[52] E. K. Lau, H.-K. Sung, and M. C. Wu, "Scaling of resonance frequency for strong injection-locked lasers," *Optics Letters*, vol. 32, no. 23, p. 3373, 2007.

[53] A. Daly, B. Roycroft, and B. Corbett, "Stable locking phase limits of optically injected semiconductor lasers," *Optics Express*, vol. 21, p. 30126, dec 2013.

[54] F. Mogensen, H. Olesen, and G. Jacobsen, "FM noise suppression and linewidth reduction in an injection-locked semiconductor laser," *Electronics Letters*, vol. 21, no. 16, p. 696, 1985.

[55] G. Yabre, "Effect of relatively strong light injection on the chirp-to-power ratio and the 3 dB bandwidth of directly modulated semiconductor lasers," *Journal of Lightwave Technology*, vol. 14, no. 10, pp. 2367–2373, 1996.

[56] A. Tauke-Pedretti, G. A. Vawter, E. J. Skogen, G. Peake, M. Overberg, C. Alford, W. W. Chow, Z. S. Yang, D. Torres, and F. Cajas, "Mutual injection locking of monolithically integrated coupled-cavity DBR lasers," *IEEE Photonics Technology Letters*, vol. 23, no. 13, pp. 908–910, 2011.

[57] P. E. Morrissey, W. Cotter, D. Goulding, B. Kelleher, S. Osborne, H. Yang, J. O'Callaghan, B. Roycroft, B. Corbett, and F. H. Peters, "On-chip optical phase locking of single growth monolithically integrated slotted fabry perot lasers," *Optics Express*, vol. 21, p. 17315, jul 2013.

[58] J. K. Alexander, P. E. Morrissey, H. Yang, M. Yang, and F. H. Peters, "Resonance Enhancement of a Monolithically Integrated Common Cavity Device," in *European Conference on Integrated Optics (ECIO)*, 2016.

[59] F. Dubois, E. Sooudi, P. E. Morrissey, J. Alexander, H. Yang, and F. H. Peters, "Mutually Coupled Semiconductor Lasers in Photonic Integrated Circuits," in *European Conference on Integrated Optics (ECIO)*, pp. 18–19, 2016.

[60] S. E. Miller, "Integrated Optics: An Introduction," *Bell System Technical Journal*, vol. 48, no. 7, pp. 2059–2069, 1969.

[61] G. E. Moore, "Cramming More Components Onto Integrated Circuits, Electronics, April 19, 1965," *Electronics*, vol. 38, no. 8, pp. 82–85, 1965.

[62] M. Smit, J. van der Tol, and M. Hill, "Moore's law in photonics," *Laser and Photonics Reviews*, vol. 6, no. 1, pp. 1–13, 2012.

[63] M. Smit, X. Leijtens, H. Ambrosius, E. Bente, J. van der Tol, B. Smalbrugge, T. de Vries, E.-J. Geluk, J. Bolk, R. van Veldhoven, L. Augustin, P. Thijs, D. D'Agostino, H. Rabbani, K. Lawniczuk, S. Stopinski, S. Tahvili, A. Corradi, E. Kleijn, D. Dzibrou, M. Felicetti, E. Bitincka, V. Moskalenko, J. Zhao, R. Santos, G. Gilardi, W. Yao, K. Williams, P. Stabile, P. Kuindersma, J. Pello, S. Bhat, Y. Jiao, D. Heiss, G. Roelkens, M. Wale, P. Firth, F. Soares, N. Grote, M. Schell, H. Debregeas, M. Achouche, J.-L. Gentner, A. Bakker, T. Korthorst, D. Gallagher, A. Dabbs, A. Melloni, F. Morichetti, D. Melati, A. Wonfor, R. Penty, R. Broeke, B. Musk, and D. Robbins, "An introduction to InP-based generic integration technology," *Semiconductor Science and Technology*, vol. 29, no. 8, p. 083001, 2014.

[64] M. Suzuki, Y. Noda, H. Tanaka, S. Akiba, Y. Kushiro, and H. Isshiki, "Monolithic integration of InGaAsP/InP distributed feedback laser and electroabsorption modulator by vapor phase epitaxy," *Journal of Lightwave Technology*, vol. 5, no. 9, pp. 1277–1285, 1987.

[65] U. Koren, B. I. Miller, G. Raybon, M. Oron, M. G. Young, T. L. Koch, J. L. DeMiguel, M. Chien, B. Tell, K. Brown?Goebeler, and C. A. Burrus, "Integration of 1.3 μm wavelength lasers and optical amplifiers," *Applied Physics Letters*, vol. 57, no. 14, pp. 1375–1377, 1990.

[66] C. Joyner and M. Zirngibl, "High performance, 12 frequency optical multichannel controller," *Electronics Letters*, vol. 30, pp. 700–701, apr 1994.

[67] S. Chandrasekhar, M. Zirngibl, A. G. Dentai, C. H. Joyner, F. Storz, C. A. Burrus, and L. M. Lunardi, "Monolithic Eight-Wavelength Demultiplexed Receiver for Dense WDM Applications," *IEEE Photonics Technology Letters*, vol. 7, no. 11, pp. 1342–1344, 1995.

[68] S. Menezo, A. Talneau, F. Delorme, S. Grosmaire, F. Gaborit, and S. Slempkes, "10-wavelength 200-GHz channel spacing emitter integrating DBR lasers with a PHASAR on InP for WDM applications," *IEEE Photonics Technology Letters*, vol. 11, no. 7, pp. 785–787, 1999.

[69] R. Nagarajan, C. H. Joyner, R. P. J. Schneider, J. S. Bostak, T. Butrie, A. G. Dentai, V. G. Dominic, P. W. Evans, M. Kato, M. Kauffman, D. J. H. Lambert, S. K. Mathis, A. Mathur, R. H. Miles, M. L. Mitchell, M. J. Missey, S. Murthy, A. C. Nilsson, F. H. Peters, S. C. Pennypacker, J. L. Pleumeekers, R. A. Salvatore, R. K. Schlenker, R. B. Taylor, T. Huan-Shang, M. F. V. Leeuwen, J. Webjorn, M. Ziari, D. Perkins, J. Singh, S. G. Grubb, M. S. Reffle, D. G. Mehuys, F. A. Kish, and D. F. Welch, "Large-scale photonic integrated circuits," *IEEE Journal of Selected Topics in Quantum Electronics*, vol. 11, no. 1, pp. 50–65, 2005.

[70] W. Cotter, *Photonic Integrated Circuit for the Manipulation of Coherent Optical Combs*. PhD thesis, University College Cork, 2013.

[71] J. Cashell, *Thermal Crosstalk in High Density Photonic Integrated Circuits*. Master's, University College Cork, 2014.

[72] R. Soref, "The Past, Present, and Future of Silicon Photonics," *IEEE Journal of Selected Topics in Quantum Electronics*, vol. 12, no. 6, pp. 1678–1687, 2006.

[73] G. Roelkens, L. Liu, D. Liang, R. Jones, A. Fang, B. Koch, and J. Bowers, "III-V/silicon photonics for on-chip and intra-chip optical interconnects," *Laser and Photonics Reviews*, vol. 4, no. 6, pp. 751–779, 2010.

[74] B. Corbett, R. Loi, W. Zhou, D. Liu, and Z. Ma, "Transfer print techniques for heterogeneous integration of photonic components," *Progress in Quantum Electronics*, vol. 52, pp. 1–17, mar 2017.

[75] L. A. Coldren, S. C. Nicholes, L. Johansson, S. Ristic, R. S. Guzzon, E. J. Norberg, and U. Krishnamachari, "High Performance InP-Based Photonic ICs—A Tutorial," *Journal of Lightwave Technology*, vol. 29, pp. 554–570, feb 2011.

[76] P. E. Morrissey, N. Kelly, M. Dernaika, L. Caro, H. Yang, and F. H. Peters, "Coupled Cavity Single-Mode Laser Based on Regrowth-Free Integrated MMI Reflectors," *IEEE Photonics Technology Letters*, vol. 28, no. 12, pp. 1313–1316, 2016.

[77] H. A. Haus, "Mode-locking of lasers," *IEEE Journal on Selected Topics in Quantum Electronics*, vol. 6, no. 6, pp. 1173–1185, 2000.

[78] K. A. Williams, M. G. Thompson, and I. H. White, "Long-wavelength monolithic mode-locked diode lasers," *New Journal of Physics*, vol. 6, pp. 179–179, 2004.

[79] J. Javaloyes and S. Balle, "Mode-locking in semiconductor Fabry-Pérot lasers," *IEEE Journal of Quantum Electronics*, vol. 46, no. 7, pp. 1023–1030, 2010.

[80] F. Lelarge, B. Dagens, J. Renaudier, R. Brenot, A. Accard, F. van Dijk, D. Make, O. L. Gouezigou, J.-G. Provost, F. Poingt, J. Landreau, O. Drisse, E. Derouin, B. Rousseau, F. Pommereau, and G.-H. Duan, "Recent Advances on InAs/InP Quantum Dash Based Semiconductor Lasers and Optical Amplifiers Operating at 1.55 um," *IEEE Journal of Selected Topics in Quantum Electronics*, vol. 13, no. 1, pp. 111–124, 2007.

[81] P. Klopp, U. Griebner, M. Zorn, and M. Weyers, "Pulse repetition rate up to 92 GHz or pulse duration shorter than 110 fs from a mode-locked semiconductor disk laser," *Applied Physics Letters*, vol. 98, no. 7, pp. 16–19, 2011.

[82] U. Keller, "Recent developments in compact ultrafast lasers," *Nature*, vol. 424, no. 6950, pp. 831–838, 2003.

[83] C. M. Gee, G. D. Thurmond, and H. W. Yen, "17-GHz bandwidth electro-optic modulator," *Applied Physics Letters*, vol. 43, no. 11, pp. 998–1000, 1983.

[84] D. G. Girton, S. L. Kwiatkowski, G. F. Lipscomb, and R. S. Lytel, "20 GHz electro-optic polymer Mach-Zehnder modulator," *Applied Physics Letters*, vol. 58, no. 16, pp. 1730–1732, 1991.

[85] E. Yamada, K. Tsuzuki, and N. Kikuchi, "Compact Low-power-consumption Optical Modulator," vol. 3, no. 3, pp. 41–45, 2005.

[86] L. A. Coldren and S. W. Corzine, *Diode lasers and photonic circuits*. 2012.

[87] M. U. Sadiq, M. R. Gleeson, N. Ye, J. O'Callaghan, P. Morrissey, H. Y. Zhang, K. Thomas, A. Gocalinska, E. Pelucchi, F. C. G. Gunning, B. Roycroft, F. H. Peters, and B. Corbett, "10 Gb/s InP-based Mach-Zehnder modulator for operation at 2 μm wavelengths," *Optics Express*, vol. 23, no. 9, p. 10905, 2015.

[88] Q. Wang, L. Huo, Y. Xing, and B. Zhou, "Ultra-flat optical frequency comb generator using a single-driven dual-parallel Mach–Zehnder modulator," *Optics Letters*, vol. 39, p. 3050, may 2014.

[89] I. Morohashi, T. Sakamoto, N. Sekine, A. Kasamatsu, and I. Hosako, "Ultrashort optical pulse source using Mach–Zehnder-modulator-based flat comb generator," *Nano Communication Networks*, vol. 10, pp. 79–84, 2016.

[90] R. M. Spencer, J. Greenberg, L. F. Eastman, C.-Y. Tsai, and S. S. O'Keefe, "High-Speed Direct Modulation of Semiconductor Lasers," 1997.

[91] I. Fatadin, D. Ives, and M. Wicks, "Numerical simulation of intensity and phase noise from extracted parameters for CW DFB lasers," *IEEE Journal of Quantum Electronics*, vol. 42, no. 9, pp. 934–941, 2006.

[92] M. Ahmed, M. Yamada, and M. Saito, "Numerical modeling of intensity and phase noise in semiconductor lasers," *IEEE Journal of Quantum Electronics*, vol. 37, no. 12, pp. 1600–1610, 2001.

[93] K. Petermann, *Laser Diode Modulation and Noise*. Kluwer Academic Publishers, 1st ed., 1991.

[94] C. H. Henry, "Theory of the Linewidth of Semiconductor Lasers," *IEEE Journal of Quantum Electronics*, vol. 18, no. 2, pp. 259–264, 1982.

[95] K. Kikuchi, "Characterization of semiconductor-laser phase noise and estimation of bit-error rate performance with low-speed offline digital coherent receivers," *Optics Express*, vol. 20, no. 5, p. 5291, 2012.

[96] R. S. Tucker, "High-Speed Modulation of Semiconductor Lasers," *Journal of Lightwave Technology*, vol. L, no. 6, pp. 1180–1192, 1985.

[97] A. Yariv, "Ultra-high speed semiconductor lasers," *IEEE Journal of Quantum Electronics*, vol. 21, no. 2, pp. 121–138, 1985.

[98] E. K. Lau, L. J. Wong, and M. C. Wu, "Enhanced modulation characteristics of optical injection-locked lasers: A tutorial," *IEEE Journal on Selected Topics in Quantum Electronics*, vol. 15, no. 3, pp. 618–633, 2009.

[99] T. B. Simpson, J. M. Liu, and A. Gavrielides, "Small-signal analysis of modulation characteristics in a semiconductor laser subject to strong optical injection," *IEEE Journal of Quantum Electronics*, vol. 32, no. 8, pp. 1456–1468, 1996.

[100] J. K. Alexander, P. E. Morrissey, L. Caro, M. Dernaika, N. P. Kelly, and F. H. Peters, "On-Chip Investigation of Phase Noise in Monolithically Integrated Gain-Switched Lasers," *IEEE Photonics Technology Letters*, vol. 29, pp. 731–734, may 2017.

[101] C. Seibert and D. Hall, "High-index-contrast ridge waveguide laser with thermally oxidised etched facet and metal reflector," *Electronics Letters*, vol. 46, no. 15, p. 1077, 2010.

[102] D. Byrne, Q. Lu, W. H. Guo, J. F. Donegan, B. Corbett, B. Roycroft, P. Lambkin, J. P. Engelstaedter, and F. Peters, "A facetless laser suitable for monolithic integration," *2008 Conference on Quantum Electronics and Laser Science Conference on Lasers and Electro-Optics, CLEO/QELS*, pp. 2008–2010, 2008.

[103] R. Phelan, W. Guo, Q. Lu, D. Byrne, B. Roycroft, P. Lambkin, B. Corbett, and J. Donegan, "A Novel Two-Section Tunable Slotted Fabry-Perot Laser Exhibiting ns Wavelength Switching," *2007 9th International Conference on Transparent Optical Networks*, vol. 2, pp. 2–4, 2007.

[104] D. C. Byrne, J. P. Engelstaedter, W. H. Guo, Q. Y. Lu, B. Corbett, B. Roycroft, J. O'Callaghan, F. H. Peters, and J. F. Donegan, "Discretely

tunable semiconductor lasers suitable for photonic integration," *IEEE Journal on Selected Topics in Quantum Electronics*, vol. 15, no. 3, pp. 482–487, 2009.

[105] P. A. Besse, J. S. Gu, and H. Melchior, "Reflectivity Minimization of Semiconductor Laser Amplifiers with Coated And Angled Facets Considering Two-Dimensional Beam Profiles," *IEEE Journal of Quantum Electronics*, vol. 27, no. 6, pp. 1830–1836, 1991.

[106] M. A. McCord and M. J. Rooks, *Handbook of Microlithography, Micromachining, and Microfabrication. Volume 1: Microlithography*. 1997.

[107] "http://britneyspears.ac/physics/fabrication/photolithography.htm," *accessed 22 Nov 2017*.

[108] "https://careers.tyndall.ie/content/photonic-integrated-circuits-pics," *accessed 22 Nov 2017*.

[109] L. Caro, N. P. Kelly, M. Dernaika, M. Shayesteh, P. E. Morrissey, J. K. Alexander, and F. H. Peters, "A facetless regrowth-free single mode laser based on MMI couplers," *Optics & Laser Technology*, vol. 94, pp. 159–164, 2017.

[110] M. Dernaika, L. Caro, N. P. Kelly, J. K. Alexander, F. Dubois, P. E. Morrissey, and F. H. Peters, "Deeply Etched Inner-Cavity Pit Reflector," *IEEE Photonics Journal*, vol. 9, no. 1, pp. 1–8, 2017.

[111] N. P. Kelly, M. Dernaika, L. Caro, P. E. Morrissey, A. H. Perrott, J. K. Alexander, and F. H. Peters, "Regrowth-Free Single Mode Laser Based on Dual Port Multimode Interference Reflector," *IEEE Photonics Technology Letters*, vol. 29, pp. 279–282, feb 2017.

[112] C. Hilsum, S. Fray, and C. Smith, "The optical frequencies and dielectric constants of InP," *Solid State Communications*, vol. 7, no. 15, pp. 1057–1059, 1969.

[113] DOW, "Processing Procedures for CYCLOTENE 4000 Series Photo BCB Resins," *CYCLOTENE Advanced Electronic Resins*, 2005.

[114] T. Tanigawa, T. Onishi, S. Nagai, and T. Ueda, "High-Speed 850nm AlGaAs / GaAs Vertical Cavity Surface Emitting Laser with Low Parasitic

Capacitance Fabricated Using BCB Planarization Technique," *CLEO 2005*, pp. 1381–1383, 2005.

[115] H. Tsuchida, "Laser frequency modulation noise measurement by recirculating delayed self-heterodyne method," *Optics Letters*, vol. 36, no. 5, pp. 681–683, 2011.

[116] H. Tsuchida, "Simple technique for improving the resolution of the delayed self-heterodyne method," *Optics Letters*, vol. 15, p. 640, jun 1990.

[117] J. K. Alexander, P. E. Morrissey, L. Caro, M. Dernaika, N. P. Kelly, and F. H. Peters, "Integratable Optical Comb Source for Coherent Communications Systems," in *Conference on Lasers and Electro-Optics (CLEO) USA*, pp. 7–8, 2017.

[118] N. Kelly, M. Dernaika, L. Caro, P. E. Morrissey, and F. H. Peters, "Monolithic Integration Of Photonic Devices For Use In A Regrowth-Free CoWDM Transmitter," *IEEE Photonics Technology Letters*, vol. 29, no. 12, pp. 1–1, 2017.

[119] A. Mar, "Optimum facet reflectivity for high speed lasers," vol. 26, no. 17, pp. 1382–1384, 1990.

[120] E. K. Lau, H.-K. Sung, and M. C. Wu, "Frequency Response Enhancement of Optical Injection-Locked Lasers," *IEEE Journal of Quantum Electronics*, vol. 44, no. 1, pp. 90–99, 2008.

[121] D. Liu, C. Sun, B. Xiong, and Y. Luo, "Modulation Characteristics Enhancement by Mutual Injection Locking of Monolithically Integrated Laser Diodes," vol. 1, no. 6, pp. 4–5, 2014.